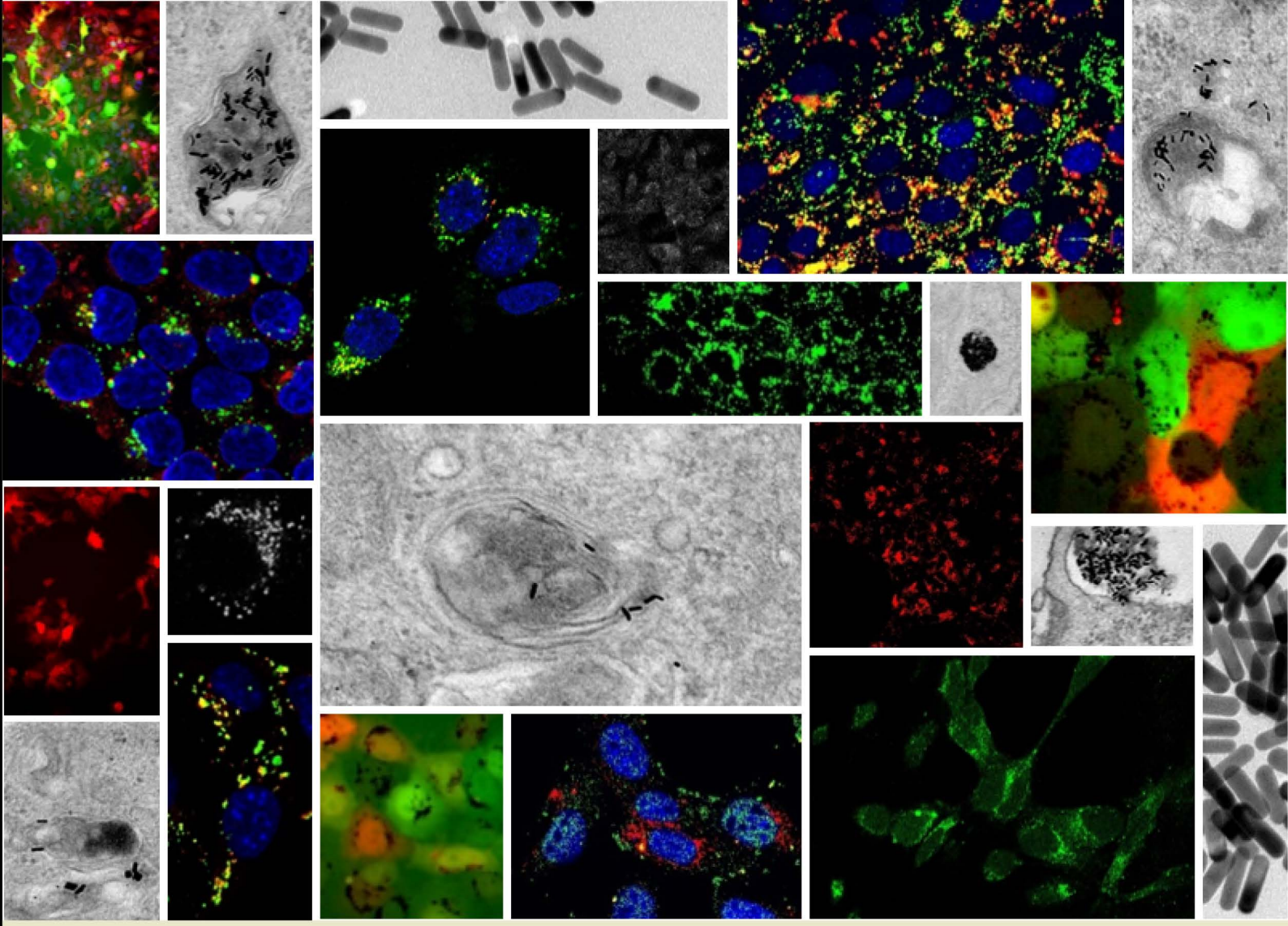

Miguel Maria da Fonseca Miranda Ferreira Lino

# LIGHT-TRIGGERABLE NANOMATERIALS FOR THE DELIVERY OF BIOMOLECULES

Tese de doutoramento em Biociências, Especialização em Biotecnologia,
orientada pelo Doutor Lino da Silva Ferreira e pelo Doutor Rui de Albuquerque Carvalho,
apresentada ao Departamento de Ciências da Vida da Faculdade de Ciências e Tecnologia da Universidade de Coimbra.

Dezembro 2016

· U C ·

Universidade de Coimbra

Miguel Maria da Fonseca Miranda Ferreira Lino

# LIGHT-TRIGGERABLE NANOMATERIALS FOR THE DELIVERY OF BIOMOLECULES

Tese de doutoramento em Biociências, Especialização em Biotecnologia, orientada pelo Doutor Lino da Silva Ferreira e pelo Doutor Rui de Albuquerque Carvalho, apresentada ao Departamento de Ciências da Vida da Faculdade de Ciências e Tecnologia da Universidade de Coimbra

Dezembro de 2016


UNIVERSIDADE DE COIMBRA

***You never fail until you stop trying***

Albert Einstein

# Agradecimentos

***Nenhum dever é mais importante do que a gratidão.***

Cícero

Toda a execução deste projecto só foi possível graças à contribuição de várias pessoas que merecem o devido apreço. Não só as que estiveram directamente ligadas ao projecto, mas também as que, mesmo não estando envolvidas neste trabalho ou que nem têm especial ligação ao mundo científico, foram importantes para que o mesmo se concretizasse.

Agradeço ao meu orientador, Dr. Lino Ferreira, por todo o apoio e incentivo demonstrados ao longo destes anos. Agradeço-lhe a exigência e o rigor que me levaram a querer superar-me a cada dia. A confiança depositada em mim também foi extremamente importante e permitiu-me ganhar independência na execução do trabalho experimental e na resolução de problemas.

Agradeço ao meu co-orientador, Dr. Rui Carvalho pelo apoio e pela ligação ao Departamento de Ciências da Vida da Universidade de Coimbra.

Gostaria de agradecer ao Biocant, UC-Biotech e seus colaboradores, pelas boas condições de trabalho que nos são proporcionadas.

Obrigado à Sónia Pinho pela ajuda e pelo impulso dado no início deste projecto e na optimização da síntese de nanorods.

Um agradecimento muito especial à Susana Simões. A Susana foi uma peça fundamental na elaboração deste trabalho e a sua ajuda foi preciosa. Agradeço-lhe todas as sugestões e o enorme apoio que me deu. Nunca me deixou desanimar! Agradeço-lhe também a atenção aos detalhes e o espírito crítico. Estou-lhe imensamente grato pela paciência que teve comigo. Às vezes a minha teimosia não é fácil.

Agradeço à Andreia Vilaça por toda a ajuda e empenho no planeamento e execução das últimas experiências deste projecto.

Um agradecimento à Alessandra pela ajuda e sentido crítico no desenho das experiências com as células endoteliais e por nos ter fornecido as células para as nossas experiências.

Agradeço à Unidade de Biotecnologia Molecular por ter disponibilizado o HPLC. Um obrigado à Carla Almeida pela ajuda.

Um obrigado ao Akhilesh pela troca de ideias no laboratório ao longo destes anos. Agradeço também por me ter deixado usar o seu gabinete durante a escrita da tese.

Agradeço a todos os meus colegas de grupo pela partilha de ideias e pelas pequenas ajudas dadas pontualmente que são essenciais para que o trabalho experimental se desenvolva da melhor forma. Obrigado pela boa disposição e por animarem os dias de trabalho.

Felizmente os anos de doutoramento foram mais do que trabalho laboratorial e uma tese para escrever. Exemplo disso são as boas amizades que criei ao longo deste percurso. Obrigado a vários elementos do grupo: Cristiana, Akhilesh, Adri, Josi, Carlos, Pedro, Su, Xica, Susana Simões, Helena Antunes, Emanuel, Renato, Nina, Patrícia e Michy e também o grupo dos pinguins, Sandra, Zé e Vitó pela vossa amizade e apoio.

Agradeço aos membros do Grupo Ohmini, a Célia, a Ju, a Sónia, a Tânia e o Rafael, por todos os momentos de diversão, pelos risos e gargalhadas que muitas vezes me permitiram esquecer as preocupações laboratoriais e manter alguma sanidade mental.

**Um agradecimento muito especial à minha família e amigos.**
Agradeço ao meu irmão e à Célia toda a força e incentivo que me dão.
Um obrigado enorme ao meu pequeno sobrinho Henrique que é um exemplo de força, perseverança e superação.
Ao meu Pai e à minha Mãe, simplesmente obrigado por tudo. Quaisquer palavras seriam escassas para expressar a minha gratidão.

# Financial Support

The research leading to this thesis has received funding from the European Research Council under the European Union's Seventh Framework Programme (FP/2007-2013) / ERC Grant Agreement nº 307384 -NanoTrigger

I would like to thank FCT for a PhD fellowship (SFRH/BD/81705/2011)

# Abstract

During the last years, proteins and microRNAs have received increased attention in the context of drug delivery, due to their modulatory effect on cellular behaviour. Moreover, the drug delivery paradigm is shifting towards combinatorial therapies for enhanced efficacy through synergistic effect between drugs. The success of multidrug delivery depends significantly on the control of drug ratios and on temporal and spatial coordination of drug delivery. This has triggered the development of new nanocarriers for immobilization of more than one drug with controllable stoichiometry and with controllable release profiles for spatio-temporal resolution on drug delivery. Nevertheless, the delivery of multiple proteins or microRNAs in an orchestrated manner remains elusive. The main objective of this thesis was to develop a near-infrared light-triggerable nanocarrier for intracellular delivery of multiple proteins and microRNAs with spatio-temporal precision. We developed a nanocarrier constituted by a gold nanorod (AuNR) conjugated with controllable amounts of single stranded DNA (ssDNA) that function as linkers for the immobilization of ssDNA-conjugated proteins or microRNAs through DNA hybridization. ssDNAs with distinct nucleotide sequences and melting temperatures were designed for highly specific hybridization and for non-overlapping release profiles. AuNRs with an aspect ratio of 3.4 and a surface localized plasmon resonance band centred at 780 nm are able to generate a photothermal effect when irradiated with a 780 nm laser. Harnessing this effect, it was possible to cause dehybridization of DNA strands and achieve distinct release profiles for each protein or microRNA. The nanoformulation was used for intracellular release of beta-galactosidase (β-Gal) and two fluorescent proteins sequentially. When irradiated, AuNRs and proteins were able to escape the endosome with low cytotoxic effect. Importantly, β-Gal remained active after being released. In this thesis, the same immobilization strategy and delivery principle were applied to the intracellular delivery of microRNAs with distinct properties for modulation of cell activity in the context of angiogenesis. miR-155 was used to enhance survival of outgrowth endothelial cells (OECs) in hypoxic conditions and miR-302a was used to induce cell proliferation. To potentiate the biological effect of miRNAs we used an antimicrobial peptide to enhance endosomal escape and uptake, increasing 63-fold the amount of gold internalized by cells. The sequential release was validated in HEK-293T reporter cell line expressing two fluorescent proteins. The first laser stimulus (2 min at 1.25 $Wcm^{-2}$) was able to release miR-155 causing knockdown of one of the proteins. A higher energy stimulus (2 min at 2 $Wcm^{-2}$) releases miR-302a that induces knockdown of the other protein. In OECs, release of miR-155 was able to induce more than 6-fold increase in cell survival. With higher energy stimulus, proliferation of OECs was induced by miR-302a.

**Keywords:** Gold nanoparticles; light-triggerable materials; near-infrared; protein delivery, microRNA delivery, modulation of cell activity.

# Resumo

Nos últimos anos, proteínas e pequenos RNAs não codificantes (microRNAs), têm recebido maior atenção no contexto de entrega de fármacos, devido ao seu efeito de modelação do comportamento celular. Além disso, o paradigma de entrega de fármacos sofreu uma mudança no sentido de combinar terapias para uma maior eficácia através de efeitos sinérgicos entre fármacos. O sucesso da entrega de múltiplos fármacos depende bastante do controlo do rácio das moléculas e da coordenação temporal e espacial da sua entrega. Isto tem impulsionado o desenvolvimento de nanopartículas para imobilização de mais do que uma molécula com estequiometria e perfis de libertação controláveis para uma maior resolução espacial e temporal na entrega de fármacos. Contudo, a entrega de múltiplas proteínas ou múltiplos microRNAs de uma forma orquestrada ainda é ilusória. O principal objectivo desta tese foi o desenvolvimento de uma nanopartícula ativada pela luz para entrega intracelular de múltiplas proteínas e microRNAs com precisão temporal e espacial. Nós desenvolvemos uma nanopartícula constituída por um *nanorod* (nanopartícula em forma de bastonete) de ouro (AuNR) conjugado com quantidades controláveis de cadeias simples de DNA (ssDNA) que funcionam como ligantes, para a imobilização através de hibridização de proteínas ou microRNAs conjugados a cadeias de DNA. Foram desenhadas cadeias de DNA com diferentes sequências e temperaturas de desnaturação para se obter hibridizações muito específicas e perfis de libertação não sobrepostos. AuNR, com um rácio entre comprimento e largura equivalente a 3.4 e uma banda de ressonância plasmónica superficial centrada a 780 nm, são capazes de gerar um efeito foto-térmico quando irradiados com um laser de 780 nm. Aproveitando este efeito, foi possível causar desnaturação das cadeias de DNA e atingir perfis de libertação distintos para cada proteína e microRNA. A formulação foi usada para a libertação intracelular de beta-galactosidase e de duas proteínas fluorescentes de forma sequencial. Quando irradiados, os AuNRs escapam aos endossomas sem induzir efeito citotóxico. A enzima beta-galactosidase permanace activa após libertação. Nesta tese, a mesma estratégia de imobilização e princípio de entrega foram aplicados à entrega de microRNAs com diferentes propriedades para modelação da atividade celular no contexto de angiogénese. O MicroRNA-155 (miR-155) foi utilizado para aumentar a sobrevivência de um tipo de células endoteliais progenitoras (outgrowth endothelial cells – OECs) em condições de hipoxia e o miR-302a foi usado para induzir proliferação celular. Para potenciar o efeito biológico dos microRNAs, nós usámos um péptido antimicrobiano para aumentar o escape aos endosomas e a internalização, tendo conseguido aumentar em 63 vezes a quantidade de ouro internalizada pelas células. A libertação sequencial de microRNAs foi validada em células repórter HEK-293T que expressam duas proteínas fluorescentes. O primeiro estímulo com laser (2 min a

1.25 $Wcm^{-2}$) induziu a libertação do miR-155, causando a diminuição da expressão de uma das proteínas. Um estímulo de maior energia causa a libertação de miR-302a e leva à diminuição da expressão da outra proteína. Em células OEC, a libertação de miR-155 aumentou em mais de 6 vezes a sobrevivência das células. Com um estímulo de maior energia, a proliferação de OECs foi induzida pela libertação de miR-302a.

**Palavras-chave**: Nanopartículas de ouro; materiais ativados pela luz; infravermelho-próximo; entrega de proteínas; entrega de microRNAs; modelação da atividade celular

# Aims and outline of the thesis

Recent advances in cell biology have set the importance of macromolecules, such as proteins[1] and microRNAs[2] in the regulation of cell activity. Additionally, orchestrated multidrug delivery is regarded as a better approach for different therapeutic applications[3, 4]. However, there is still a lack of adequate nanotechnology-based systems for independent and sequential release of more than one molecule. The aim of this thesis was to develop a light-triggerable nanoformulation for spatio-temporal controlled release of more than one macromolecule for modulation of cell activity. During the thesis we have performed two sub-projects. One related to the development of a plasmonic nanocarrier for light-controlled release of two proteins. In the other work, we designed a nanocarrier for light-triggered release of two microRNAs that could be applied in the modulation of the angiogenic potential of outgrowth endothelial cells.

**Chapter I** reviews nanocarriers and the importance of multidrug delivery. This chapter also provides an overview about stimuli-responsive nanoformulations, focusing on light-triggerable nanocarriers and plasmonic nanoparticles for delivery of macromolecules. Different strategies for endosomal escape of nanocarriers are also reviewed. The last section of this chapter describes the modulatory effect of microRNAs in outgrowth endothelial cells and their therapeutic potential.

**Chapter II** describes the development of a gold nanorod-based system for sequential delivery of proteins. It provides information about the synthesis, functionalization and characterization of the nanocarrier. It also presents results regarding laser-induced release profiles of fluorescent proteins and an active enzyme, intracellular release and endosomal escape of proteins.

**Chapter III** describes a gold-nanorod system for modulation of angiogenic activity by sequential delivery of two microRNAs. It describes the conjugation process and the functionalization of AuNRs. It also presents results regarding the use of an antimicrobial peptide as uptake enhancer and endosomolytic agent. Finally it describes the validation of the technology in a reporter cell line and in outgrowth endothelial cells.

**Chapter IV** discusses the experimental results described in chapters II and III and presents new prospects for future work.

# Publications and Communications

Miguel. M. Lino, Susana Simões, Sónia Pinho and Lino Ferreira. “Delivery of more than one protein with spatio-temporal control” *Submitted*

Miguel. M. Lino, Susana Simões, Andreia Vilaça and Lino Ferreira. “Modulation of angiogenic activity by light-activatable nanocarriers carrying miRNAs”. *Under preparation*

Miguel M. Lino, Susana Simões, Sónia Pinho, Lino Ferreira. “Modulating cell activity by opto-nanomedicine”. 9th International Meeting of the Portuguese Society for Stem Cells and Cell Therapies. Oeiras, October 2015

Miguel M.Lino; Susana Simões; Sónia Pinho, Lino Ferreira. “Modulating protein delivery by optonanomedicine” World Biomaterials Congress. Montreal, May 2016.

**Patents**

Lino, M.,Ferreira, L. “A composition for controlled release of proteins”. PAT20151000082123.

# Table of Contents

# Abbreviations

AMP – Antimicrobial peptide

AuNR – Gold nanorod

AuNS – Gold nanoshell

B-Gal – Beta-galactosidase

BSA – Bovine serum albumin

CAD – Coronary artery disease

CM – Cecropin-melittin

CPP – Cell penetrating peptide

CTAB – Hexadecyltrimethylammonium bromide

CV – Coefficient of variation

CW – Continuous wave

DL – DyLight

DNQ - 2-diazo-1,2-naphthoquinone

dsDNA – Double stranded DNA

EGFP – Enhanced green fluorescent protein

EPC – Endothelial progenitor cell

FBS – Fetal bovine serum

FDA - US Food and Drug Administration

HEK-293T – Human embryonic kidney cells

HGNP- Hollow gold nanoparticles

HUVEC – Human umbilical vein endothelial cell

HPLC – High-performance liquid chromatography

ICP-MS - Inductively coupled plasma mass spectrometry

LSPR - Localized surface plasmon resonance

MHA – Mercaptohexanoic acid

miR - MicroRNA

miRNA- MicroRNA

MSNP – Mesoporous silica nanoparticle

NIR – Near-infrared

NP – Nanoparticle

OEC – Outgrowth endothelial cell

ONPG - o-nitrophenyl β-d-galactopyranoside

PAGE – Polyacrylamide gel electrophoresis

PBS – Phosphate buffered saline

PEG – Polyethylene glycol

PEI – Polyethylenimine

PLGA - Poly(lactic-co-glycolic) acid

PNIPAM - Poly(N -isopropylacrylamide)

RNAi – RNA interference

RISC - RNA induced silencing complex

ROS – Reactive oxygen species

SDS – Sodium dodecyl sulphate

siRNA – Small interference RNA

ssDNA – Single stranded DNA

Sulfo-GMBS - N-[γ-maleimidobutyryloxy]sulfosuccinimide ester

TBE – Tris/borate/EDTA

TEM – Transmission electron microscopy

TRITC - Tetramethylrhodamine isothiocyanate

UCNP – Upconversion nanoparticle

UV – Ultraviolet

VEGF – Vascular endothelial growth factor

# List of Figures

# List of Tables

# Chapter 1

## Introduction

## 1.1 - The importance of multidrug delivery

The mechanisms of health and disease are extremely complex, involving intricate and highly orchestrated networks. As these mechanisms are being unveiled, medicine and biomedical technologies are adapting and shifting to new paradigms. For example, the drug delivery paradigm is shifting from one drug-one target to a combination of drugs-multiple targets. The multifactorial pattern of certain diseases such as cancer, diabetes and cardiovascular diseases requires new therapeutic approaches based on the combination of multiple drugs to achieve a therapeutic synergy, where the combinatorial effect is greater than the sum of the effects of the individual drugs [5]. Moreover, combined therapies with drugs with different modes of action are also effective approaches to optimise therapeutic efficacy, while minimising side effects [6].

Indeed, multidrug delivery in an orchestrated fashion may be of great interest for several purposes. For example, in cancer treatment, the order of drug delivery may have a significant impact in the final outcome, where simultaneous or reverse administration of drugs can even induce antagonistic effect [7]. Likewise, in regenerative medicine applications, complex cascades of events demand the delivery of multiple drugs or bioactive molecules in an coordinated manner [8]. In a cell reprogramming context, it has been shown that the order in which the transcription factors are expressed in progenitor cells has impact in the lineage outcome [9]. Also, in tissue repair and regeneration, the sequential presentation of signal proteins plays an important role in the remodelling of diseased tissue [10].

Additionally, the evidence of dysregulation of biomolecules such as non-coding RNAs in multiple diseases has added a new layer of complexity in the regulatory molecular circuits of diseases, but has also opened new therapeutic opportunities [11]. The elucidation of these circuits can help in the design of new therapeutic agents and will raise the possibility of interfering with multiple cellular processes either simultaneously or sequentially, by silencing multiple target genes [3]. Combinatorial silencing of genes with multiple small interfering RNAs (siRNAs) has already been reported as a promising strategy to enhance therapeutic effects in the treatment of cancer[12, 13] and infectious diseases[14, 15].

Importantly, this new paradigm of drug delivery is being supported not only by a deeper understanding of biological processes but also by technological innovation in nanomaterials with the design of new and more complex delivery systems [16].

## 1.2 - Nanotechnology and nanomedicine

In 1959, the future Nobel laureate Richard Feynman, shared his revolutionary vision in a lecture entitled “There is Plenty of Room at the Bottom”, setting the principles of a new field of research: “I would like to describe a field, in which little has been done, but in which an enormous amount can be done in principle” [17]. Although Feynman did not introduce the term nanotechnology, he could envision the conceptual idea of a science based on the miniaturization and convergence of physical, chemical and biological processes at the molecular level. By definition, nanotechnology refers to research at the scale of 100 nm or less for the restructure, control of matter and creation of materials with new properties and functions. In fact, nanotechnology has received a great deal of attention during the last decades. It is a unique science in the sense that it represents not only one specific field but a variety of fields of research. The integration of nanotechnology in biomedical research has received the term nanomedicine and it comprises a multitude of applications such as *in vivo* imaging, *in vitro* diagnostics, biomaterials, active implants and drug delivery [18], which are changing the foundations of disease diagnosis, treatment and prevention. In particular, the application of nanotechnology in drug delivery focuses in the development of nanomaterials that can be used as carriers or drug delivery systems (DDS) to improve bioavailability and pharmacokinetics of therapeutics. Nanotechnology may be useful (1) to improve drug solubility; 2) to target the delivery of drugs; 3) to control the dosage of the drug; 4) to reduce the toxicity of the drug; 5) to allow the transcytosis of drugs across epithelial and endothelial barriers; 6) to allow the intracellular delivery of macromolecules; 7) to make possible the co-delivery of multiple drugs, etc...

### 1.2.1 - Nanocarriers

Since the first report on the encapsulation of a drug in liposomes[19], a diversity of nanoparticulate systems for drug delivery has emerged, which is reflected in the increasing number of nanocarriers undergoing clinical trials [20]. Nanocarriers can be differentiated in terms of their chemical composition, physical properties, surface chemistry (**Figure 1.1**), although a categorization may be difficult to achieve given the heterogeneity of the systems reported so far. Nevertheless, an important feature of all types of nanocarriers is the high surface-to-volume ratio that enables their modification with multiple compounds to tailor properties and optimize drug loading. Physical parameters like size, shape and surface charge play critical role in the function of nanocarriers *in vitro* and *in vivo*. Nanoparticle size and shape has been shown to have impact on several cellular responses, including

nanoparticle uptake[21, 22], adhesion, migration and cell viability[23], as well as biodistribution and clearance *in vivo*[24, 25]. Size and shape also determine other properties of the nanocarrier. For example, the size and shape of gold nanoparticles have influence on their optical properties.[26]

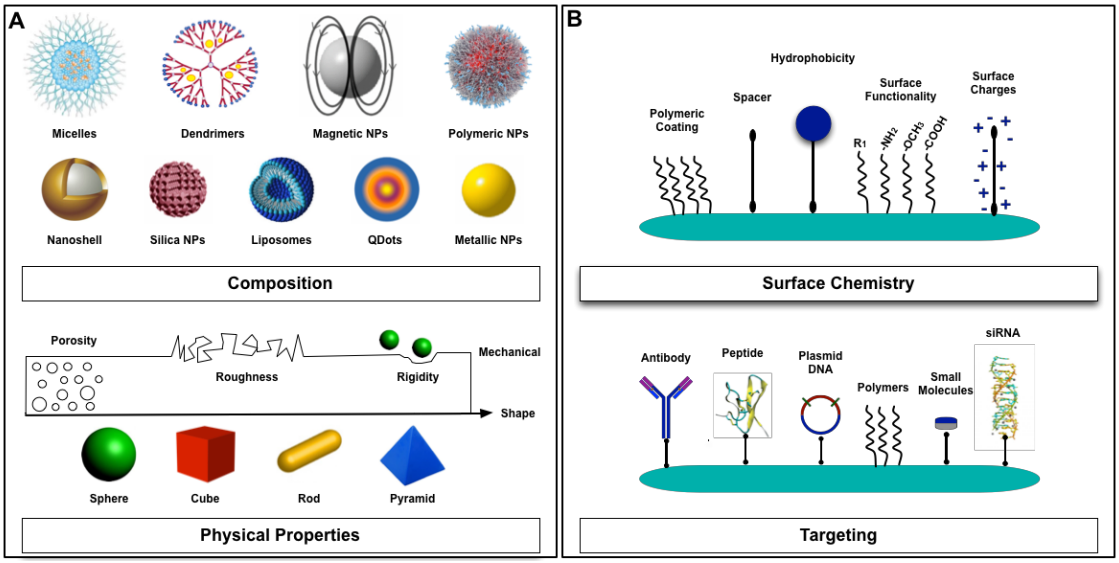


**Figure 1.1 - Nanoparticle properties affecting drug release.** A) Nanoparticles can be differentiated in terms of material composition and physical properties. B) Surface modification with different ligands confers specific properties and enables conjugation with different molecules for targeting and drug delivery. Image from [27].

A relevant aspect in nanocarrier design is the interaction between the payload and the nanocarrier. Cargos can be immobilized by covalent bonds or non-covalently via weak forces such as electrostatic and hydrophobic interactions, by hydrogen bonding or physically entrapped in a matrix. Moreover, the cargo can be immobilized on the particle surface or encapsulated. In the latter approach, the drug is incorporated at the time of the nanoparticle formation whereas in the former strategy the drug is usually loaded after nanoparticle synthesis. The synthesis flexibility of nanocarriers has enabled extraordinary control in the loading of wide range of therapeutics. Nanoparticles are also being designed as systems for multidrug delivery[16], namely for cancer treatment as a form of combinatorial therapy[4]. Furthermore, nanocarriers are evolving into smart multi-functional systems, i.e, systems that besides delivering drugs, are able to respond to stimuli, to target specific tissues, cells and subcellular compartments and additionally function as imaging agents or diagnosis sensors[28].

## 1.2.2 - Multidrug delivery systems

When compared to combinations of free drugs, nanoparticle formulations for multidrug delivery offer several advantages: 1) normalized biodistribution and pharmacokinetics through the controlled released of drugs from the nanocarrier; 2) stability of chemically dissimilar drugs; 3) possibility to tune independently the release of each drug; 4) targeted co-release of drugs in the same organ, tissue or cell to increase efficacy and to reduce toxicity[16].

Multidrug delivery systems may be categorized according to two models [29]. The synergistic model, in which two or more therapeutics are combined to achieve maximum efficacy, and the sequential model, in which a single therapeutic is released after a first activation followed by the release of the second therapeutic after a second activation, and so on. In this model, the temporal control over the release of each therapeutic is crucial for the efficacy of the therapy. Several formulations following the synergistic model have been reported mainly in the context of cancer treatment [30, 31]. In some formulations, chemotherapeutic doxorubicin is delivered in combination with a siRNA that sensitizes the cells to the chemotherapeutic agent. Other systems have been developed to combine drug release with photothermal therapy [32-34]. A synergistic gold nanorod (AuNR) system has been reported to deliver siRNA for gene silencing, followed by the induction of hyperthermia upon NIR irradiation to cause cell death[32]. In this study, when each of the therapeutics was applied separately, cell viability decreased to 60%, contrasting to 80% decrease when both therapeutics were applied. The synergistic co-delivery has also been reported for tissue engineering purposes. Co-delivery of a siRNA and SOX9 protein in PLGA nanoparticles was able to induce chondrogenesis of mesenchymal stem cells [35].

The sequential delivery model has been applied for the sequential release of two drugs from a nanocarrier[36-38]. Zhang and colleagues designed hollow gold nanoparticles (HGNPs) to control by NIR light the sequential delivery of miR-21 inhibitor (miR-21i) and doxorubicin to cancer cells [36]. MiR-21i, which was bound through electrostatic interactions to PAMAM dendrimers immobilized on the surface of HGNPs, was released without the need of NIR light. PAMAM dendrimers were used to escape the endosomes and promote release of miR-21i into the cytosol. Doxorubicin adsorbed on the surface of HGNPs was then released after NIR irradiation. The sequential release of both therapeutics was fundamental, since miR-21i sensitized the cells to the chemotherapeutic drug, achieving better results than co-administration therapy. Sequential activation of nanoparticles has also been explored for cell targeting and subsequent drug release[39-41]. In a recent work[41], mild near infrared (NIR) irradiation of AuNRs resulted in shrinkage of a thermosensitive PEG corona and exposure of an RGD coating. A higher energy stimulus was then applied to

promote the intracellular release of siRNA and doxorubicin to induce cell death. The PEG corona was used to protect the siRNA against nuclease digestion. The first irradiation at the tumour site increased nanoparticle uptake by cancer cells, by exposing an RGD shell on the surface of AuNRs for specific uptake via receptor-mediated endocytosis. Cancer cells were then treated with siRNA targeting polo-like kinase 1 (PLK1) and doxorubicin after a second laser irradiation.

## 1.2.3 - Nanoparticle design for controlled multidrug delivery

Combinatorial therapies involve the precise control of drug dosages and timing of delivery. Several formulations have already been developed for co-delivery of different drugs[10, 6], but fine-controlling the loading and timing of release of each drug remains a challenge. The simplest approach to achieve this purpose consists in the administration at different times of multiple nanocarriers loaded with each drug[42]. Technically, it allows an easier optimization process for the immobilization of drugs with different physicochemical properties, albeit the pharmacokinetics and biodistribution of each system may not be correlated. Consequently it may be difficult to attain co-localization of sequential treatments, even if the carriers are similar[43].

During the last years, different strategies have been adopted in order to achieve a controlled release of each drug from the same carrier (Figure 2). A single nanocarrier-based delivery has advantages over separate administration of drugs in synchronizing pharmacokinetics and biodistribution of drugs, despite being technically challenging. The immobilization is usually achieved in a multistep process that can impact the stability of the formulation. Also, the amount of each drug in the same nanocarrier may be difficult to control. This is one important aspect, since, in some cases, the ratio of combined drugs determines whether they will provide synergistic, additive or antagonist effects[44]. One approach for multidrug delivery is based on the use of hydrolytically degradable polymers, for example, in hydrogels[45] or nanoparticles[46, 47] (**Figure 1.2 a**). In order to have sequential release of multiple drugs, distinct immobilization strategies and localization of each drug within the same nanocarrier have been explored as well[48, 49] (**Figures 1.2 b and 1.2 c**). In a polymeric nanocapsule system tested *in vitro* and *in vivo*, one of the drugs (Paclitaxel) was covalently attached to the polymer, whereas combretastatin A4 was encapsulated in the core of the nanostructure[47]. The encapsulated drug was the first being released while the covalently immobilized drug took longer to be released. The same principle was applied in the development of polymeric nanomicelles to deliver sequentially an autophagy inhibitor and a chemotherapeutic drug [50]. A recent study reported a sequential release of two drugs

from silicon dioxide self-decomposable nanoparticles. Different loading methodologies allowed a differential distribution of the drugs within the nanocarrier and consequently a sequential release.[51] Other methodology consists in the covalent attachment of drugs to the carrier via different linkers with distinct hydrolysis rates [52].

The release of different molecules from the same system may also be modulated by using stimuli-responsive materials, attaining a higher level of spatio-temporal control (**Figure 1.2 d**). Recently, Segura's group developed enzyme responsive polymeric nanocapsules dispersed in an injectable hydrogel for the delivery of proteins [10]. In this study, the spatial and temporal patterns of protease expressions in the diseased tissue were exploited for the sequential release of two growth factors through the integration in the polymer shells of protease-specific peptides. Polymeric nanoparticles responsive to three distinct stimuli (hydrolysis, pH and irradiation) have already been reported for the release of three chemotherapeutic drugs [53].

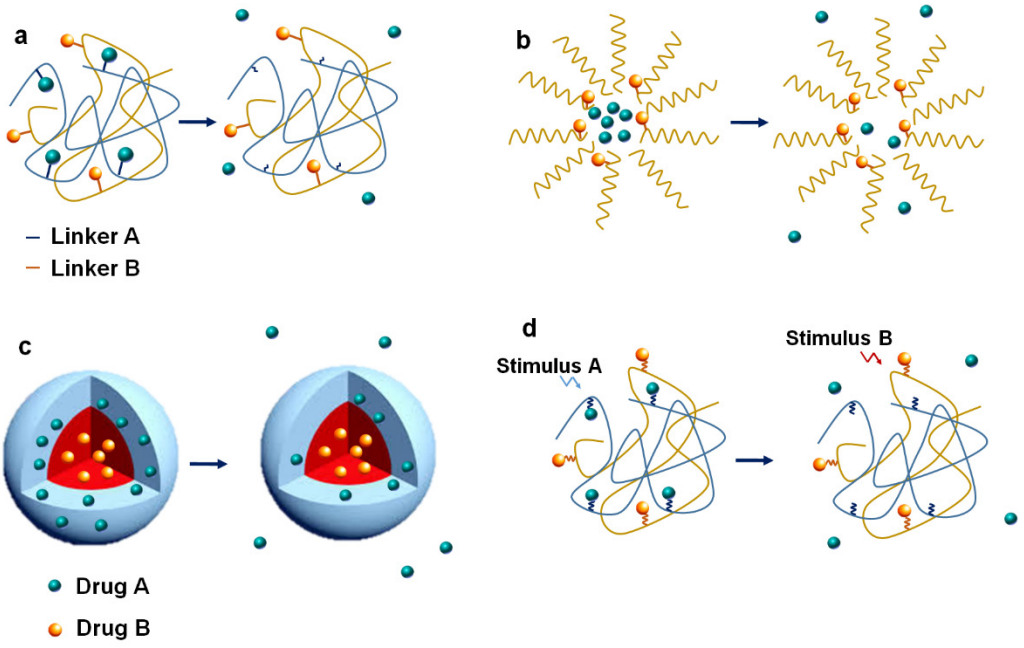


**Figure 1.2 – Nanoparticle design for multidrug delivery**. (a) polymeric nanoparticle modified with linkers (A and B) with different degradation/hydrolysis rates for sequential release of drugs A and B. (b) Nanocarrier with a drug covalently attached to its components and another drug encapsulated in the core of the nanostructure. (c) Nanoparticle with two drugs encapsulated/bound at different locations of the nanocarrier. The drug in the outer layer is the first being released, (d) Nanocarrier responsive to different stimuli (pH, proteases, light – λ1, λ2, etc). Sequential application of stimuli A and B leads to controlled release of each drug.

So far, only a limited number of studies have reported an independent delivery of multiple molecules from the same carrier using external stimuli as a trigger[54, 55]. A recent study showed the potential of light stimulus for the orthogonal release of multiple proteins

from hydrogels modified with photocleavable units responding to different wavelengths in the UV region [55]. It has also been reported the sequential release of cargos in response to one internal and one external stimulus [36, 37]. Although nanomaterials sensitive to stimuli have provided a higher control over the release of drugs, sequential release of multiple drugs from the same using step-by-step external activation is still an unmet need. Also, the majority of the systems reported until now for multidrug delivery were designed for the delivery of small drugs. Few works have reported tuned delivery of more than one macromolecule from the same carrier [10, 55].

## 1.3 - Stimuli-responsive nanoparticles

The design of stimuli-responsive systems for controlled release of drugs has attracted much attention[56, 57]. The relevance of strategies for controlled release is driven by the possibility of reaching different levels of control: i) timing; ii) duration; iii) location iv) dosage and v) independent release of multiple drugs. In line with this, new methods have been developed to control drug delivery either by the susceptibility of the nanocarrier to changes in its microenvironment or by an external stimulus triggered by an operator. Accordingly, stimuli-responsive nanomaterials may respond to endogenous stimuli such as pH[58], enzymatic activity[10], redox environment/glutathione concentration[59, 60], among others. A controlled drug delivery may also be achieved using magnetic[61], ultrasound[62], thermo[63] and light[64] sensitive materials that respond to an external stimulus. The remote activation of the nanocarrier may enable repeated and reproducible dosing of the drug, reducing risks associated with toxicity while increasing efficacy.

### 1.3.1 - Light as a stimulus

When compared to other external triggers, light offers some advantages: i) precise control of the size of the area being irradiated by varying the beam of the laser, providing a higher level of spatial control; ii) the possibility of having a system that responds to different wavelengths for multiple drug release. Although no light-triggerable drug delivery system has yet been translated into clinical trials[65], light has already been used in clinical setting to treat different diseases[66]. Light-triggerable systems can respond to ultraviolet (UV), visible or near infrared (NIR) light depending on the type of materials and light-responsive mechanisms associated. A considerable part of the light-triggerable systems is constituted by compounds that respond only to UV light[67, 68], since it is a high-energy radiation capable

of inducing conformational changes or break covalent bonds. However, a major drawback associated to UV light as an external stimulus is the low penetration depth, narrowing potential biomedical applications to organs easily accessible, such as the skin and the eye. Furthermore, UV light may have deleterious effects in biological tissues. These may arise from the generation of radical oxygen species by intracellular photosensitizers like porphyrins[69], causing DNA damage and lipid peroxidation. Additionally, light may trigger photothermal damage, leading to protein denaturation or even cell apoptosis if the rate of energy delivery is higher than the rate of energy dissipation in the tissue[70].

In order to overcome the disadvantages associated to UV light, new systems using nanomaterials responsive to NIR irradiation have been developed. The main advantage of NIR irradiation (650-900 nm) is the low absorbance by skin and tissue, enabling a penetration depth on the order of hundreds of micrometres to centimetres[71]. This makes NIR light extremely attractive for biomedical applications including bioimaging and drug delivery.

#### 1.3.1.1 – Light-responsive mechanisms

Light can interact directly with chromophores and induce structural and conformational changes through different mechanisms. These changes may be reversible or irreversible. This principle has been applied to the development of several drug delivery systems. Besides the direct interaction between light and chromophores, mechanisms of indirect photoactivation have also been tested. These include light upconversion, photothermal effect and photo-induced generation of radicals.

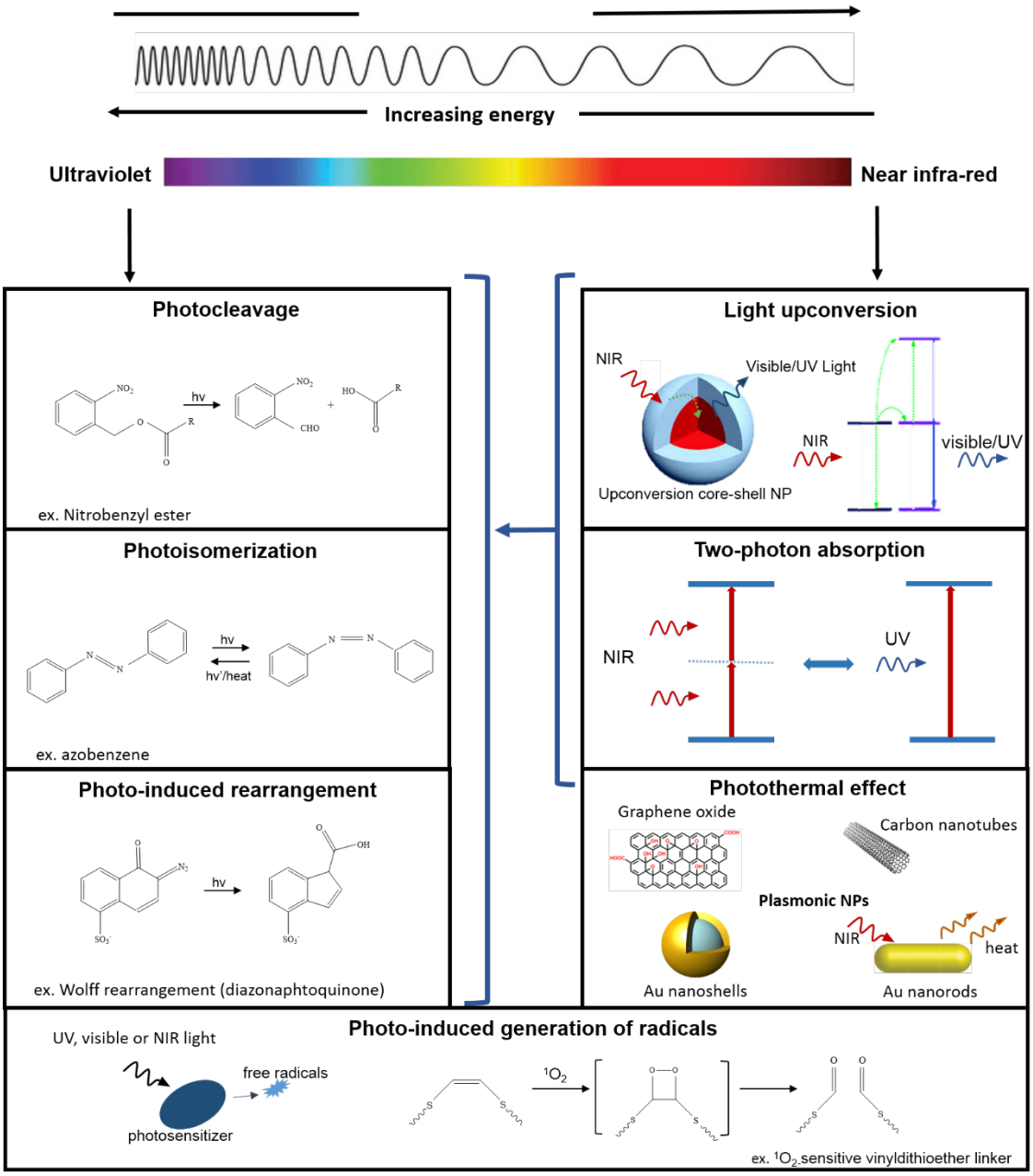


**Figure 1.3 - Schematic representation of photoresponsive mechanisms in light-sensitive nanocarriers**. Light can interact directly with chromophores via absorption of one UV photon or two NIR photons inducing structural or conformational changes, such as photocleavage, isomerization and molecular rearrangements. Indirect strategies include: light upconversion, where the upconverted light interacts with photo-sensitive compounds; photothermal effect; photo-induced generation of radicals. Adapted from ref [65].

## Photocleavage

A variety of formulations for drug delivery have included photolabile protective groups that can be cleaved upon light irradiation. Among these photosensitive compounds, the ortho-nitrobenzyl-based and their dimethoxy derivatives[72] are by far the most studied protective groups (**Figure 1.3**). Recently, coumarin-based compounds[73] have also received

increased attention, mainly because of their longer wavelength absorption and large two-photon cross-section. These photolabile compounds have found a range of applications in light-responsive delivery systems. They have been used as linkers[55], binding covalently the drug to the nanocarrier. In this case, the photo-induced cleavage leads to the release of the drug. Photolabile compounds have also been extensively used as protective caging groups.[74] In this approach the caged molecule/drug is inactive until light irradiation and cleavage of the photolabile molecule. Photocleavable compounds have been integrated in diblock copolymers as well[75]. Usually this strategy is used to affect the hydrophilic-hydrophobic balance of nanostructures formed by the polymers upon irradiation, leading to the release of the encapsulated drug.

**Photoisomerization**

Drugs can also be released from nanocarriers by reversible changes in the conformation of molecules. For example, azobenzene and spiropyran can be photoisomerized from trans to cis conformation when irradiated with UV light, and from cis to trans conformation when irradiated with visible light [76] (**Figure 1.3**). Azobenzene has been integrated in micellar formulations, where UV-induced isomerization leads to a change in the hydrophilic-hydrophobic balance, causing disruption of the micelles[77]. Azobenzene has also been used in mesoporous silica nanoparticles, usually as part of a pore-capping system. For example, the incorporation of azobenzene in a nanovalve system with DNA oligonucleotides allowed the control over hybridization/dehybridization of DNA strands with a consequent capping/uncapping of the nanoparticle pores to hold/release doxorubicin[78].

**Photo-induced rearragement**

UV light has been used to induce molecular rearrangements as well. For example, when hydrophobic 2-diazo-1,2-naphthoquinone (DNQ) is irradiated, it undergoes a Wolff rearrangement, becoming hydrophilic[79] (**Figure 1.3**). This principle has been applied in micellar formulations triggering their destabilization by UV irradiation[80].

**Photo-induced generation of radicals**

The use of photosensitizers has also been reported in drug delivery systems. Photosensitizers are able to generate radicals when they are irradiated with an appropriate wavelength. These radicals may be used to induce chemical changes in the nanocarrier components. This approach was used in a formulation based on mesoporous silica

nanoparticles coated with singlet oxygen-sensitive crosslinkers[81, 82]. Irradiation of a photosensitizer loaded in the MSNPs induced the generation of singlet oxygen, causing the cleavage of the linker and the release of a model drug. Light-induced disassembly of amphiphilic block copolymer micelles bearing a singlet oxygen sensitive linker was also reported[83]. Irradiation with visible light of micelles containing chlorine e6 (photosensitizer) and doxorubicin resulted in the destruction of the micelle. A similar approach was used in a photosensitive hydrogel formulation[84]. Upon UV light irradiation, a photoinitiator produced free radicals, which attacked disulfide bonds in the hydrogel, leading to its fragmentation.

### 1.3.1.2 - NIR light triggering

Although the use of nanomaterials that respond to UV light has been extensively explored, their biomedical application is hampered by the low penetration depth of UV irradiation in biological tissues and also by the potential toxic effects of this high energy irradiation, which is driving research in NIR-responsive systems.

**Two-photon absorption**

Using the two-photon technology, the photolabile compound absorbs two photons in the NIR region leading to the same structural modifications achieved with one photon in the UV region (**Figure 1.3**)[85, 86]. Generally, the probability of excitation by the absorption of two photons is very low, therefore this process requires the use of pulsed lasers in order to provide a high density of photons in short pulses (nanosecond to femtosecond scale). In fact, researchers have tried to improve the efficiency of this process, increasing the photosensitivity of photolabile groups for two-photon excitation[87]. Typically, that is achieved by an increase in the two-photon absorbance cross-section of the photolabile group[88]. Among the various chromophores, coumarin derivatives have a larger two-photon cross-section. The use of [7-(diethylamino)coumarin-4-yl]methyl has been reported in micelles constituted by amphiphilic block copolymers[89]. NIR irradiation induced the photocleavage of the chromophore, leading to changes in hydrophilic/hydrophobic balance and the consequent disassembly of the micelle.

**Ligth upconversion**

Recently, the use of inorganic materials responsive to NIR light in drug delivery systems has also been exploited. Examples of such systems comprise nanoformulations

incorporating upconversion nanoparticles (UCNPs) constituted by lanthanides[90, 91]. UCNPs are able to absorb long wavelength NIR light and give origin to sharp emissions in the visible and UV region[92]. Taking advantage of this effect, researchers have combined UCNPs with UV-responsive compounds, enabling the release or uncaging of drugs. UCNPs have been used in photo-triggerable drug delivery systems to induce photoisomerization of azobenzene, for the destabilization of azobenzene-modified liposomes[92] or to promote mechanically the release of drugs encapsulated in mesoporous silica[93]. Additionally, upconversion of NIR light has been used as well for the photocleavage of photolabile groups, such as nitrobenzyl derivatives. A photodegradable polymer bearing nitrobenzyl moieties was used to encapsulate UCNPs and a fluorophore[94]. Upconverted UV light led to the photodegradation of the polymer and to the release of the payload. UCNPs have also been reported for the intracellular delivery of macromolecules. For example, UCNPs modified with a positively charged nitrobenzyl linker are able to carry siRNA through electrostatic interaction. Upon irradiation at 980 nm, the UV light emitted by the UCNP cleaves the linker, leading to the release of siRNA[95].

**Photothermal effect**

The photothermal effect refers to the conversion of light energy into heat by a nanomaterial. So far, several nanomaterials have shown efficient conversion of visible and NIR light into heat, including carbon nanotubes[96], graphene oxide[97] and plasmonic gold nanoparticles[98]. This effect was brought into drug delivery systems mainly by the possibility of combining the aforementioned photothermal converters with thermo-sensitive materials. Recently, near infrared absorbing plasmonic nanoparticles have emerged as promising candidates for light-controlled delivery systems. Indeed, some plasmonic nanoparticles, such as AuNRs, can act as efficient nanoantennas, with molar extinction coefficients in the near infrared region four orders of magnitude higher than most organic dyes[99, 100]. It has been demonstrated that a steady state temperature of 95 ºC in the vicinity of AuNRs could be reached after 10 min irradiation at 800 nm with 10 $mWcm^{-2}$ [101].

The excellent photothermal conversion achieved by plasmonic nanoparticles has been harnessed not only to induce changes in thermosensitive polymers[102], but also to release DNA oligonucleotides through dehybridization [103] and to destabilize liposomes[104, 105]. For example, the well-studied thermosensitive polymer poly(N -isopropylacrylamide) (PNIPAM) was used in hybrid plasmonic nanocarriers [106, 107]. Irradiation with a NIR laser led to a local increase of temperature and a concomitant phase transition of the polymer. This principle has already been exploited for the release of anticancer drugs in mice[107].

The heat generated by these nanostructures may be sufficient to induce irreversible changes in the nanostructure as well. For example, NIR irradiation of graphene oxide composite capsules caused rupture of the capsules leading to the release of encapsulated doxorubicin[108]. Plasmonic gold nanoparticles have also been reported to suffer changes in their shape upon certain conditions of laser irradiation[109, 110], which can lead to the controlled release of molecules immobilized on the gold surface.

## 1.3.2 - Delivery of macromolecules

Macromolecules such as nucleic acids and proteins are increasingly important as new therapeutic agents[111, 112]. Due to the susceptibility of these biomolecules to degradation and instability in serum, appropriate delivery systems must be designed. However, because of their intrinsic properties, the immobilization in nanocarriers is not straightforward. For example, proteins have large sizes, variable surface charges and fragile three-dimensional conformations that should be preserved in order to maintain protein activity. Proteins are sensitive to mechanical stress, temperature and organic solvents, which needs to be taken into account when immobilizing proteins in a nanocarrier.

### 1.3.2.1 - Light-controlled delivery of proteins

Protein therapeutics offer several advantages relatively to small molecules including (1) high specificity and complex set of functions that cannot be mimicked by chemical compounds, (2) less potential to interfere with normal biological processes and cause side effects, (3) less likely to induce immune responses, since many of the proteins approved for therapeutics are naturally produced in the body [1]. There are more than 130 different proteins or peptides approved for clinical use by the US Food and Drug Administration (FDA), and many more are in development[1]. Almost all of these protein therapeutics, such as immune-modulating cytokines, antibodies and growth factors target cell membrane receptors and do not require internalization to exert a biological effect. Nevertheless, intracellular delivery of several proteins, such as superoxide dismutase[113], caspase 3[114], ribonuclease A[115] has already demonstrated potential to treat different diseases, like neuro-cardiovascular diseases[113] and cancer[114, 115]. Recent advances in cell reprogramming using cocktails of transcription factors for induction of pluripotency[116] or for direct reprogramming of somatic cells into another type of somatic cell[117] also open the way to a repertoire of new intracellular protein therapeutics.

The delivery of proteins poses some challenges. When administered systemically, proteins can suffer from instability or be cleared rapidly from the body. Furthermore, because most native proteins are negatively charged at neutral pH, they tend to be cell-membrane impermeable, which is not adequate if intracellular targeting is needed[118]. Finally, endosomal sequestration can also hamper the therapy if cytosolic delivery is required. These issues have elicited the development of several non-viral-based strategies for the delivery of proteins. For example, the utilization of adjuvants to increase protein uptake and endosomal escape has been reported. Recently, the group of Niels Geijsen developed a protein transduction methodology based on the induction of macropinocytosis with hypertonicity and on the use of non-detergent sulfo-betaine that helps releasing the proteins from internalized macropinosomes [119]. Likewise, another study reported efficient delivery of proteins into the cytosol by using dimerized TAT as an endosomolytic agent[120].

The conjugation of proteins with transduction domains and the development of nanoparticles for protein delivery have also been explored. These systems include, among others, liposomes, polymeric nanoparticles, gold nanoparticles, mesoporous silica nanoparticles and natural vectors such as cell-penetrating peptides (CPP)[118]. Although there is an increasing number of stimuli-responsive nanocarriers for "on demand" delivery of proteins[121], the examples of light-responsive systems are still scarce (**Table 1.1**) and so far only one system reported the controlled sequential delivery of more than one protein using UV light (although this system is a gel and not a nanoparticulate system which is required for intracellular delivery of some proteins) [55]. Light-controlled intracellular delivery of proteins has been mainly restricted to proof-of-concept studies with fluorescent proteins, therefore the delivery of proteins for modulation of cell activity is yet to be validated. Norbert Reich and colleagues reported a gold nanoshell (AuNS) system for NIR light-induced release of transcription factors (Sox2 and p53) without inducing their degradation, albeit the effect of these proteins was not evaluated in cells [122]. So far, no light-activatable formulation has been reported for the delivery of proteins with intracellular biological effect that could be used to modulate cell activity. Finally, until now, no light-controlled delivery system of proteins has been tested *in vivo*.

**Table 1.1 - Examples of light-responsive formulations for protein delivery.**

| Nanocarrier | Cargo | Immobilization strategy | Photo-responsive mechanism | Stimulus | Ref. |
|---|---|---|---|---|---|
| Polymeric nanogel modified with metoxy-nitrobenzyl-ether | Alkaline phosphatase and BSA | Encapsulation | Photocleavage-photodegradation of nanogel | UV 365 nm<br>10 $mWcm^{-2}$; 2min | 123 |
| Hydrogel modified with nitrobenzyl ether and coumarin methylester | BMP-2 and BMP-7 | Covalent bond | Photocleavage | 365 nm – 5 $mWcm^{-2}$; 6min<br>400nm – 5 $mWcm^{-2}$; 12min | 55 |
| Micelles formed by block copolymer containig *o*-nitrobenzyl groups | FITC-BSA | Electrostatic interactions | Photocleavage | UV 365 nm<br>UV Lamp-8 W | 124 |
| Hollow upconversion NPs modiifed with spyropiran | β-Galactosidase | Encapsulation/ electrostatic interaction | Upconversion-isomerization | NIR 980 nm<br>0.5$Wcm^{-2}$; 20 min | 125 |
| Polyelectrolyte multilayer microcapsules with AuNPs in the capsule walls | GFP | Encapsulation | Potothermal | NIR 830 nm<br>3.8 $mW\mu m^{-2}$; < 2s | 54 |
| Gold nanoshells | GFP | Thiol-gold bond | Photothermal | NIR 800 nm<br>$8x10^3$ $Wcm^{-2}$; 300μs | 122 |

### 1.3.2.2 - Light-controlled delivery of nucleic acids

Gene therapy comprises the delivery of genes encoding proteins or gene silencing therapies. Gene silencing therapies include the delivery of antisense DNA oligonucleotides complementary to target mRNA sequences and also the delivery of small interfering RNA (siRNA) or microRNAS (miRNA) that block the translation of mRNA sequences and knockdown specific proteins. SiRNAs and miRNAs have gained much attention due to their role in gene regulation. SiRNAs and miRNAs have very similar physicochemical properties but distinct modes of action (**Figure 1.4**) [126]. MiRNAs are transcribed as primary microRNAs (pri-miRNAs) in the nucleus by RNA polymerase II, which are then cleaved by drosha to form pre-miRNAs with hairpin-like structure. The pre-miRNA is transported by exportin 5 to the cytoplasm where it is processed by Dicer into miRNA duplex of 20-24 nucleotides. The miRNA is loaded into the RNA induced silencing complex (RISC) where the passenger strand is discarded, and the miRNA-RISC complex is guided by the remaining guide strand to the target mRNA through partially complementary binding. The target mRNA is inhibited via translational repression, degradation or cleavage. One miRNA can target multiple genes. SiRNAs have origin in double stranded RNA molecules (transcribed from cellular genes or infecting pathogens, or artificially introduced into the cells) that are processed by

DICER into duplexes with 21-23 nucleotides. Subsequently, siRNA associates with RISC where the endonuclease argonaute 2 (AGO2) cleaves the passenger strand (sense strand) of the siRNA while the guide strand (antisense strand) remains associated with the RISC. Afterwards, the guide strand guides the RISC to its target mRNA for cleavage by AGO2. The guide strand binds to fully complementary mRNA strands causing specific gene silencing.

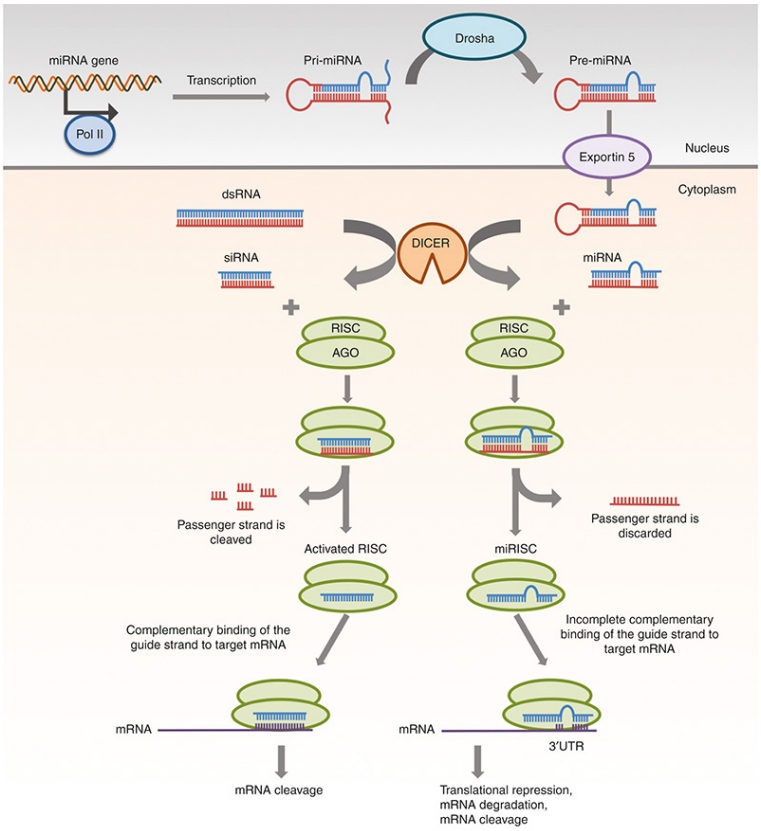


**Figure 1.4 - Gene silencing mechanisms of siRNAs and miRNAs**. Long dsRNAs (left side of the figure) are processed by Dicer into small interfering RNAs (siRNAs) that associate with RNAi-induced silencing complex (RISC) where AGO protein cleaves the passenger siRNA strand. Then, the mature RISC containing AGO2 and the guide strand associates with the target mRNA for cleavage. Primary microRNAS are transcribed by polymerase II in the nucleus and then processed by Drosha into a precursor called pre-miR. pre-miRNAs associate with exportin 5 and are exported to the cytoplasm where it is processed by DICER into miRNA. The duplex associates with an Argonaute (AGO) protein within RISC. One strand of the duplex (the passenger strand) is removed. The mature RISC contains the guide strand, which directs the complex to the target mRNA for post-transcriptional gene silencing. Scheme from [126].

Although viral particles still represent the majority of current gene therapy trials, a significant effort has been done in the last 10 years to develop safer methods based in non-viral vectors [127]. Nucleic acids and, in particular siRNA and miRNA, are highly susceptible

to degradation by serum nucleases. Moreover, the cellular uptake of these molecules is very low because of the high molecular weight and negative charge, requiring the use of delivery vectors. In order to achieve this goal, researchers have focused on the chemical modification of nucleic acids to enhance stability[128], conjugation with small molecules or peptides for targeting and uptake[129] and also on the development of nanocarriers[130]. Moreover, several stimuli-responsive nanomaterials have been designed for increased uptake, endosomal escape and cytosolic release of nucleic acids[131]. A significant part of these nanomaterials respond to internal stimuli such as pH, redox potential and temperature[131]. Systems controlled externally by light have also been reported for the delivery of plasmid DNA, antisense oligonucleotides and siRNAs (**Tables 1.2 and 1.3**)**.** For plasmid DNA, the immobilization is usually achieved through electrostatic interactions with the nanocarrier, avoiding chemical modification of the biomolecule, whereas for siRNAs it has been reported the electrostatic interactions and the direct immobilization on gold nanocarriers via thiol-gold bonds that are cleaved upon irradiation. **T**he immobilization of the nucleic acid in the nanocarrier is usually achieved via electrostatic interactions. The release can be triggered by changes in the electrostatic balance after photocleavage or photoisomerization of a light-sensitive moiety in the nanocarrier (**Table 1.2**) or via photothermal effect (**Table 1.3**)

**Table 1.2 - Examples of light-responsive formulations for nucleic acid delivery.**

| Nanocarrier | Cargo | Immobilization strategy | Photo-responsive mechanism | Stimulus | Ref. |
|---|---|---|---|---|---|
| Micelles | T4-phage DNA | Electrostatic interaction | Photoisomerization micelle disassembly | UV 365 nm Lamp-84 W; 10 min | [32] |
| AuNPs | Oligonucleotides | Electrostatic interaction | Photocleavage surface charge change | UV 350 nm 2h | [33] |
| Diblock copolymer micelles | siRNA | Electrostatic and hydrophobic interactions | Photocleavage micelle disassembly | UV 365 nm 200 $mWcm^{-2}$; 20 min | [34] |
| Polymeric NPs | Plasmid | Electrostatic interactions | Photocleavage photodegradation of the polymer | UV 365 nm Power? 10 min | [35] |
| Helical polypeptides | Plasmid | Electrostatic interaction | Photocleavage polyplex disassembly | UV 365 nm 20 $mWcm^{-2}$; 5 min | [36] |
| Polymeric NPs | DNA | Electrostatic interaction | Photo-induced generation of ROS cleavage of ROS sensitive polymer | White light 50 $mWcm^{-2}$; 5min | [37] |

**Table 1.3 - Light-induced release of nucleic acids from plasmonic gold nanoparticles using photothermal effect**

| Nanocarrier | Cargo | Surface functionalization | Immobilization strategy | Laser | Stimulus | Ref. |
|---|---|---|---|---|---|---|
| AuNR | Plasmid DNA | CTAB | Electrostatic interaction | Pulsed, 800 nm | 1.14 $Wcm^{-2}$ | 138 |
| AuNR and AuNS | ssDNA | ssDNA | Hybridization | CW, 800 nm | 1.3 $Wcm^{-2}$ | 103 |
| AuNR | Antisense oligonucleotide | CTAB | Electrostatic interaction | CW | 0.9 $Wcm^{-2}$ | 139 |
| AuNR | siRNA | Oligofectamine | Electrostatic interaction | CW, 785 nm | 1.6 $Wcm^{-2}$ | 140 |
| AuNR | siRNA | PSS/PDDAC | Electrostatic interaction | CW, 810 nm | 2.7 $Wcm^{-2}$ | 141 |
| AuNR | Plasmid DNA | PEI-PEG-RGD | Electrostatic interaction | CW, 808 nm | 3 $Wcm^{-2}$ | 142 |
| AuNS | siRNA | Poly-L-lysine | Electrostatic interaction | CW, 800 nm | 2.5 $Wcm^{-2}$ | 91 |
| AuNS | siRNA | Citrate | Thiol-gold bond | Pulsed, 800 nm | 2.4 $Wcm^{-2}$ | 143, 144 |

# 1.4 - Plasmonic gold nanoparticles

During the last decades, advances in nanotechnology originated a diversity of nanoscale materials suitable for several biomedical applications. In particular, noble metal nanoparticles have shown to be one most versatile nanostructures due to the synthetic control of their size, shape and assembly. Different methods have been applied to synthesize gold nanostructures in a variety of shapes (**Figure 1.5**), including gold spherical nanoparticles, nanorods, gold pyramids and nanoshells[145]. Furthermore, interesting optical properties can be achieved by reducing noble metals to a nanometre scale[98].

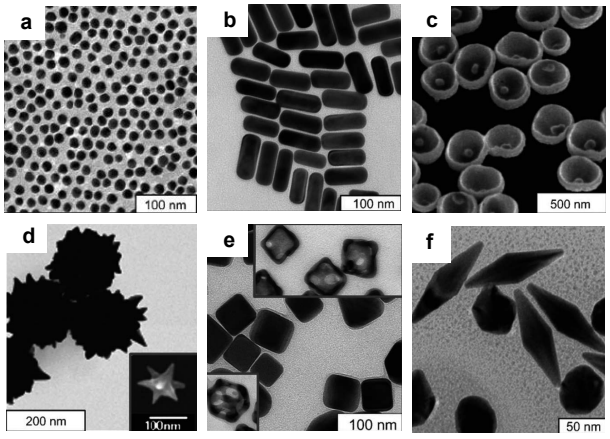


**Figure 1.5 - TEM images of different types plasmonic gold nanoparticles.** a) gold nanospheres; b) gold nanorods; c) nanobowls; d) spiky $SiO_2$/gold nanoshells; e) gold-silver nanocages; f) gold bipyramids. (Adapted from ref.[146])

The relatively easy functionalization of the gold surface with a variety of ligands bearing functional groups with affinity towards gold such as thiols, amines[147] and phosphines[148] is one of the advantages of these inorganic nanoparticles and has amplified their potential for diagnostic and therapeutic applications. In addition, the gold core is essentially inert and non-toxic. Extensive research has been done in this field and gold nanoparticles have been modified with different biomolecules, namely DNA oligonucleotides[149], peptides[150] and antibodies[151]. The unique chemical, physical and optical properties of these nanoparticles has leveraged their potential for biomedical applications, ranging from drug delivery[152], to biosensing[153], diagnosis and cancer therapy[154].

## 1.4.1 - Optical properties

Noble metal nanoparticles and, in particular, gold nanoparticles, have unique electronic and optical properties which are originated from the large surface area-to-volume ratio and from the spatial confinement of the surface electrons in the gold nanostructures [98]. One of the most characteristic properties is the localized surface plasmon resonance (LSPR), which is caused by the coherent collective oscillation of the free electrons, forming a dipole oscillation along the direction of the electric field of light (**Figure 1.6**). At a specific frequency, the amplitude of this oscillation reaches resonance maximum. Under resonant excitation, noble metal nanocrystals have interesting and useful effects, such as large electric field enhancement, increased light scattering and absorption and high photothermal conversion. Furthermore, a remarkable feature of these nanomaterials is that their LSPR can be tuned by controlling their size and shape. For example, comparing to spherical nanoparticles, rod shaped particles have anisotropic optical properties, which are determined by the oscillation of the electrons along the transversal and longitudinal direction. These coherent oscillations along different axis of the nanorods originate two LSPR bands. A lower peak around 520 nm is due to the oscillation along the transversal direction and is similar to the LSPR band characteristic of nanospheres. This peak is insensitive to size changes. A more intense peak, caused by the oscillation along the longitudinal direction, can be tuned by controlling the synthesis parameters and consequently the size of nanorods, thus ranging from 650 to 1050 nm[155]. The longitudinal LSPR band varies linearly with the aspect ratio. Also, the increase in size of spherical nanoparticles or aspect ratio of gold nanorods has an impact on absorption and scattering of light. For example, for gold nanorods, as the aspect ratio increases, both absorption and scattering efficiencies increase[156], making these nanostructures good candidates for photothermal therapy as well as for imaging purposes. Additionally, nanorods can be

assembled into a variety of superstructures with several geometries for enhanced plasmonic properties [157].

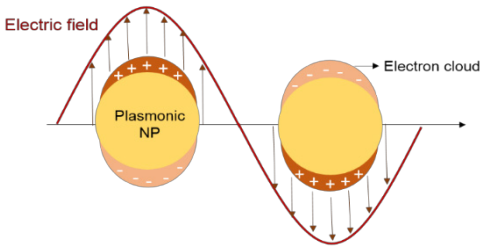


**Figure 1.6 - Schematic representation of the localized surface plasmon resonance.** Free electrons are driven into oscillation due to the coupling with incident electromagnetic radiation.

## 1.4.2 - Photothermal conversion

Besides the enhanced radiative properties, plasmonic gold nanoparticles are also able to convert the absorbed light into heat through non-radiative processes. This effect has been explored for several biomedical applications, including photothermal therapy to kill cancer cells[158, 159], controlled drug delivery[160] and photothermal imaging[161].

Upon laser excitation, surface electrons oscillate coherently, followed by a thermalization process with the lattice, where the kinetic energy is transferred on a picosecond time scale via electron-electron interactions and by phonon-phonon relaxations with the surrounding medium[162], which in turn will increase the temperature (**Figure 1.7**). Specifically, after electronic excitation, a relaxation process starts through electron-electron scattering. Then, hot electrons transfer vibrational energy to the lattice, generating a coherent vibrational state (phonon). This excited vibrational state leads to an increase in the temperature of the lattice that decays through phonon-phonon interactions between the lattice and the surrounding medium. The heat decay in the nanoparticle is followed by an increase in the temperature of the surrounding medium.

The photothermal conversion efficiency may be highly affected by different factors such as the particle volume, shell coating and assembly state[163]. For nanoparticles with similar shape, the increase in nanoparticle size leads to an increase in light scattering and consequently decreases the fraction of absorbed light, which is responsible for the photothermal effect. The coating can affect the photothermal conversion by increasing the light absorption with semiconductor materials or by changing the refractive index of the medium. The assembly state can cause shifts in the LSPR and change its intensity, thereby influencing the photothermal conversion efficiency.

The effect of optical heating on plasmonic AuNPs has been described[164, 165]. The temperature increase on the surface of an individual NP in aqueous solution is determined by:

$$\Delta T = \frac{AR^3}{3D.\mathrm{K}water}$$

where *A* corresponds to heat input per volume, which is given by IC/V (*I* is the light intensity, *C* is the absorption and *V* is the nanoparticle volume). *R* is the nanopaticle radius, *D* is the distance from the nanoparticle centre and $K_{water}$ is the thermal conductivity of water. For example, laser irradiation of gold NPs with 100 nm can lead to a surface temperature increase between 100 K and more than 300 K when the power of the laser varies from 0.3 to 1 W [165]. The heat generated in a suspension of NPs has been attributed to an accumulative heating effect, which comes from heat fluxes generated by single NPs[166]. As a result, the accumulative effect will be highly dependent on the concentration of NPs.

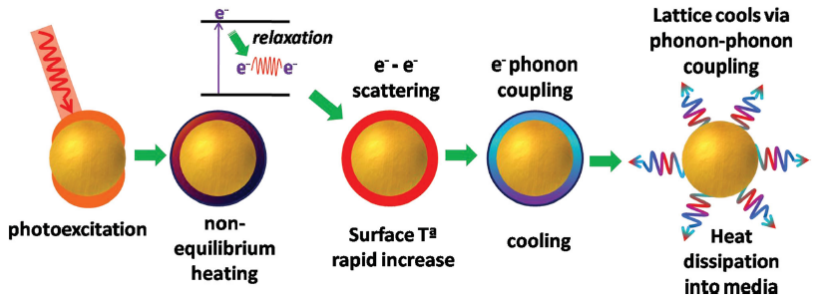


**Figure 1.7 - Schematic representation of the photothermal conversion process in plasmon resonant NPs**. Upon laser irradiation, energy is transferred on a picosecond scale through electron-electron interaction leading to non-equilibrium heating and to a rapid increase of temperature on the NP surface. The heat is then dissipated into the medium through phonon-phonon interactions. Adapted from ref. [167].

Photo-excitation of plasmon resonant NPs can be done with different laser sources, such as continuous wave (CW) laser, nanosecond pulsed and femtosecond pulsed lasers[110]. In a CW mode, the laser emits a steady laser beam over a certain period. On the other hand, when using pulsed lasers, the energy is given in short pulses in nanosecond or femtosecond time scale. The reduction in the duration of the pulses results in lower energy pulses but with higher powers. This can lead to an increase of the metal lattice temperature above its melting temperature within picoseconds, resulting in nanoparticle reshape, while maintaining the temperature of the surrounding environment. This occurs since the heat loss to the surrounding solvent (above 100 picoseconds) is slower than the heat transfer

between the electrons and the lattice (below 10 picoseconds)[110], which generates a massive heat accumulation within the lattice. Taking advantage of this process, several formulations based on plasmonic NPs have been used for the delivery of biomolecules through cleavage of thiol-gold bonds [168, 169].

## 1.4.3 - Plasmonic nanoparticles for light-triggered drug delivery

Plasmonic nanomaterials with their strong LSPR absorption are extremely efficient in converting the absorbed light into heat. This interesting phenomenon has been applied to the development of drug delivery systems in order to provide spatio-temporal control on drug delivery. Plasmonic gold nanoparticles (AuNPs) exhibit LSPR centred at different wavelengths depending on their size and shape. Therefore gold nanorods and gold nanoshells, which have LSPR bands in the NIR region, have more potential for these types of technology. The photothermal-triggered release using plasmonic nanocarriers has been applied to the delivery of small molecules and also macromolecules. The delivery of small drugs has been achieved with three different approaches:

i) Embedding of the drug in a thermosensitive polymeric matrix surrounding the plasmonic NP. The heat generated by the gold nanoparticle causes changes in the polymer structure inducing the release of the drug. In 2000, Sershen *et al* published the first study reporting the photothermally-triggered release of molecules. In this study, gold nanoshells were embedded in a hydrogel formed by N-isopropylacrylamide (NIPAAm)-co-acrylamide (AAm)[170]. NIPAAm-co-AAm hydrogels are temperature-sensitive polymers with lower critical solution temperatures (LCST) slightly above body temperature. When the temperature of the polymer raises above its LCST, it undergoes a reversible phase transition, resulting in collapse of the hydrogel structure (**Figure 1.8 a**). The heat generated by gold nanoshells irradiated at 1064 nm was sufficient to cause the collapse of the hydrogel releasing methylene blue and proteins as well. The photothermal triggered release was also reported using polyelectrolyte layers deposited on AuNRs[171]. Continuous wave laser irradiation at 785 nm caused release of rhodamine loaded between the polyelectrolyte layers. Isothermal calorimetry data indicated a strong interaction between rhodamine and the polyelectrolyte, which weakens upon laser irradiation. The authors also suggested a thermal expansion of the polyelectrolyte layers as a possible explanation for the controlled release of rhodamine (**Figure 1.8 b**). DNA complementarity has also been employed in the development thermosensitive polymeric shells on gold AuNRs [172]. The hydrogel layer around AuNRs was formed by polyacrylamide polymers grafted with oligonucleotides for

cross-linking through DNA hybridization. DNA dehybridization induced by the photothermal effect resulted in dissolution of the hydrogel and release of doxorubicin and fluorescein (**Figure 1.8 c**).

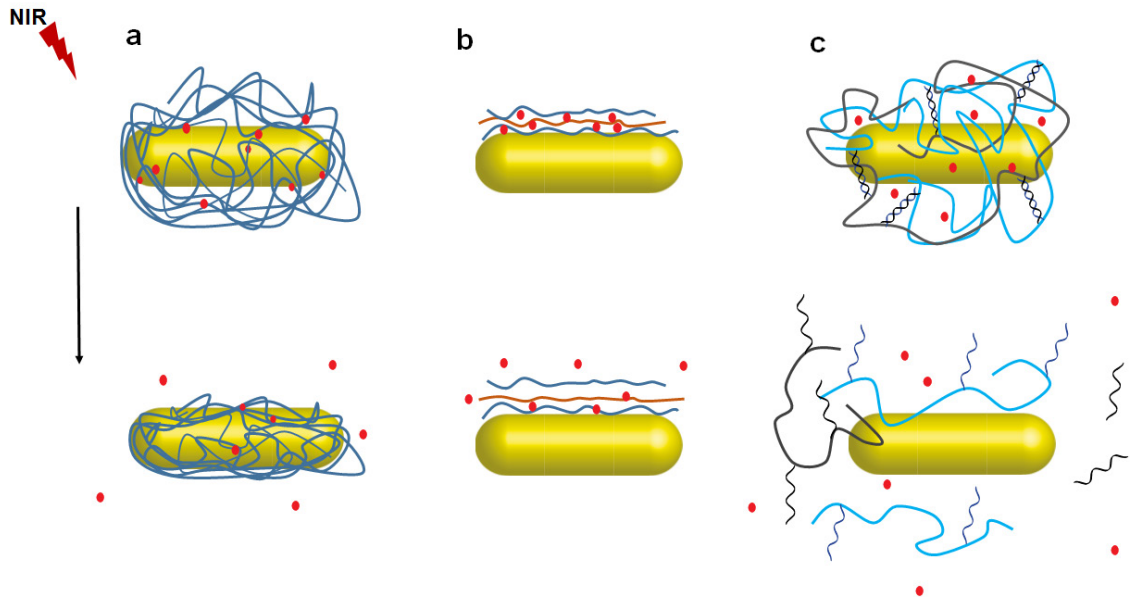


**Figure 1.8**. **Schematic representation of light-induced release of small drugs entrapped in a thermosensitive coating surrounding a plasmonic NP.** (a) AuNRs coated with NIPAAM hydrogels that collapse when LCST is achieved. Collapse of the hydrogel leads to release of drugs embedded in the polymeric matrix. (b) Photothermal release of a drug embedded in a polyelectrolyte matrix, probably due to the expansion of the polyelectrolyte layers. (c) Photothermal-induced dissolution of dsDNA polymeric hydrogel surrounding a AuNR through dehybridization of dsDNA crosslinking the polymer chains.

ii) Embedding of the drug in liposomes, which are ruptured upon laser irradiation of the gold nanocarrier, releasing their content. The coupling between plasmonic nanocarriers and liposomes has emerged as one approach to overcome one the drawbacks of liposomes, the slow release of drugs. Burst release of encapsulated drugs has been shown after irradiation of gold nanoshells either encapsulated in liposomes (**Figure 1.9 a**) or tethered to the liposome membrane [173] (**Figure 1.9 b**). To take advantage of the photothermal effect, researchers have also developed nanoformulations with thermosensitive liposomes[104, 105] (**Figure 1.9 c**). A similar principle has been applied to the development of cholesteryl succinyl silane (CSS) nanomicelles coated with gold nanoshells [174]. The increase in temperature leads to a phase transition in the CSS molecules triggering the release of doxorubicin.

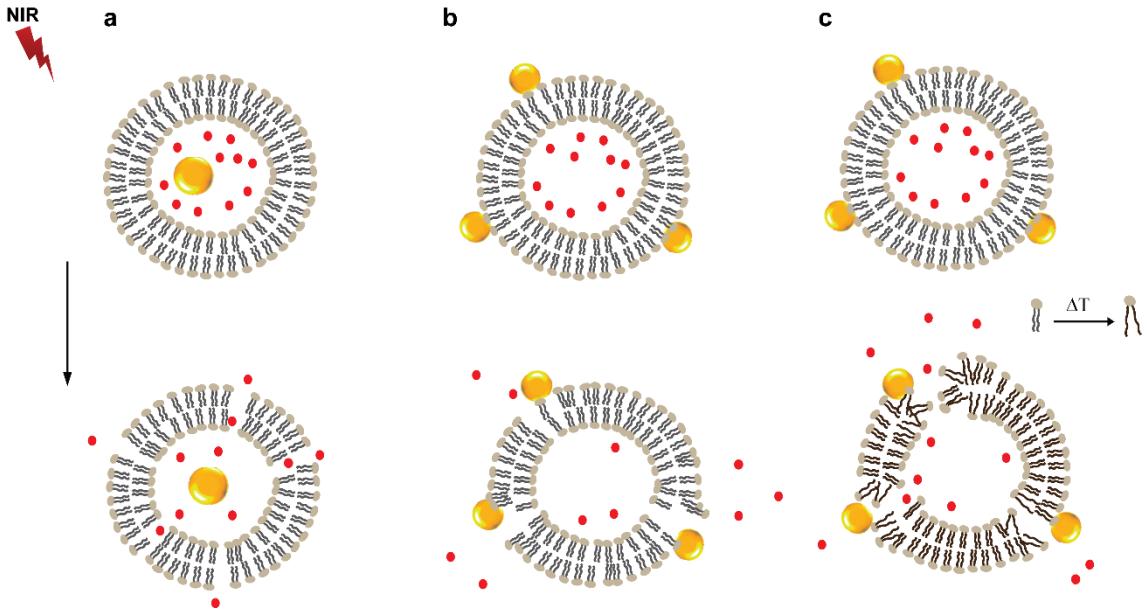


**Figure 1.9 - Schematic representation of light-induced release phenomenon of small drugs encapsulated in liposomes containing plasmonic NPs**. Release of drugs encapsulated in liposomes with gold nanoshells encapsulated (a) or tethered (b) to the liposome. Release of drugs encapsulated in thermosensitive liposomes (c).

iii) Embedding of the drug in mesoporous silica nanocomposites[175-177]. In these formulations, mesoporous silica nanomaterials function as a reservoir for the drug. The drug is kept in the reservoir by a system of valves or gates designed to respond to a thermal stimulus. The use of DNA oligonucleotides in photothermally-controlled valves has been reported. A study showed the release of doxorubicin after photohermally triggered dehybridization of double stranded DNA gatekeepers in mesoporous silica coated AuNRs (**Figure 1.10 a**)[175]. A slightly different system was designed with reversible single stranded DNA valves (**Figure 1.10 b**). The electrostatic interaction between the DNA strands and the silica surface weakens upon irradiation at 808 nm controlling the release of cargo molecules[178]. Other gatekeeper systems have been reported, such as calixarenes[177] (**Figure 1.10 c**) and phase-changing materials[176, 179].

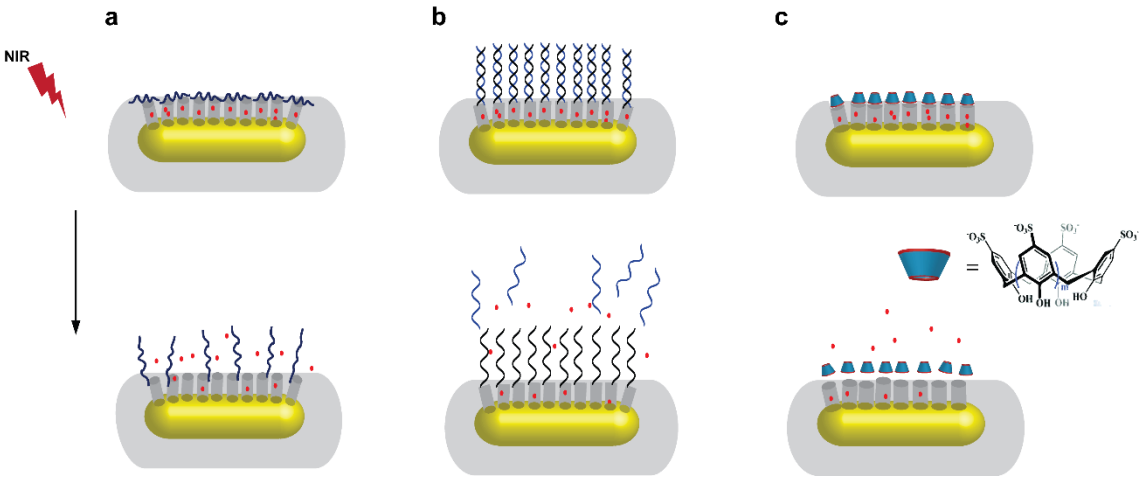


**Figure 1.10** - **Light-induced release of small drugs encapsulated in mesoporous silica-coated plasmonic NPs**. Silica pores are coated with a thermoresponsive material that allows release of molecules through a photothermal effect. (a) AuNR with ssDNA adsorbed to the silica coating closing silica pores. The photothermal effect leads to desorption of DNA strands and opening of the pores. (b) Silica-coated AuNR with dsDNA valves. Thermal-induced dehybridization leads to drug release. (c) AuNR with calixarene that closes silica pores though host-guest interactions. Photothermal effect reduces the interaction and opens the pores.

The strategies adopted for the controlled release of macromolecules from plasmonic nanocarriers differ from the approaches developed for the release of small drugs. In general, the main difference is that the macromolecule is not entrapped in a polymeric matrix or encapsulated, although macromolecule encapsulation has been reported with AuNRs coated with NIPAAM hydrogels (strategy (i) for small molecules, **Figure 1.8 a**)[170]. The controlled delivery of siRNA and plasmid DNA has been achieved after their electrostatic immobilization in the nanoparticle surface[140, 168] as well as after their direct binding to the surface of the nanoparticle via thiol-gold chemistry[169]. Regarding the first strategy, the cargo is released through photothermal destabilization of the interaction between siRNA and the polymers covering the nanoparticle surface. Regarding the second strategy, the release of the cargo is achieved after the cleavage of thiol-gold bond induced by a femtosecond pulsed laser. In this case, the near covalent thiol-gold bond is destabilized and cleaved by photoexcited electrons from the gold plasmons that do not thermalize with the lattice of the material [180]. This leads to a selective and localized increase of temperature at the nanoparticle surface, decreasing exponentially with the distance to the surface[101]. Different formulations based on plasmonic NPs for light-triggered release of macromolecules are summarized in Table 1.3 (section 1.3.2).

Although light-triggered drug delivery with plasmonic NP has not yet reached clinical trials, plasmonic NPs for photothermal therapy are under clinical evaluation[181], which also validates the relevance of light irradiation of nanoformulations in a clinical setting.

## 1.4.4 - Gold nanorods

The controllable synthesis and tuneable optical properties of AuNRs have made them good candidates for controlled drug delivery, among other applications. AuNRs can be prepared by different methods, including top-down and bottom-up methods. In top-down methods, AuNRs are obtained through the deposition of gold using lithography processes. The bottom-up methods comprise, among others, electrochemical[182], and wet chemical synthesis [183]. Usually, in these techniques, a template is used in order to confine the growth of nanorods along one direction during reduction of gold salt. One of the most common procedures for nanorod synthesis is a wet-chemical CTAB mediated method developed independently by Murphy *et al*[184] and El Sayed *et al*[155], also designated as seed mediated method. In this method, the CTAB surfactant micelles work as "soft templates" for growing nanorods, producing nearly monodisperse AuNRs in high yields. The methodology involves the production of small gold nanoparticle seeds from the reduction of chloroauric acid with sodium borohydride in a CTAB solution. Then, the seeds are added to a growth solution, containing Au(I) complex ions obtained from reducing Au(III) complex ions with ascorbic acid in aqueous CTAB solution. An important step of the process is the addition of $AgNO_3$ to this solution, which increases the yield of AuNRs and reduces the amount of nanocrystals with different shapes, such as spheres and triangular plates. Furthermore, it has been shown that the pH and temperature of the growth solution, the amount of each reagent and the ratio between them has impact on the aspect ratio of the rods and consequently on the wavelength of the LSPR peak[155]. For example, increasing the amount of silver nitrate or gold chloride leads to a higher wavelength LSPR band, however only up to a certain concentration, after which it has an opposite effect. Although this bottom-up method is able to produce AuNRs with high uniformity, reproducibility of shape and size between batches may be difficult to achieve[185].

### 1.4.4.1 - Surface functionalization

In order to grant stability under different conditions, AuNRs should be functionalized with appropriate organic or inorganic compounds. CTAB-capped nanorods are the most

used type of gold nanorods, however they present several challenges in terms of toxicity, stability and functionalization, limiting their usefulness for further biomedical applications[186]. One of the major drawbacks of CTAB-capped nanorods is their poor stability in high salt content at low CTAB concentration. Moreover, they are also susceptible to aggregation in the presence of organic solvents, which may disrupt the CTAB bilayer. Several strategies have been developed to modify the surface of AuNRs, including layer-by-layer deposition of polyelectrolytes[32, 187, 188] or the displacement of the CTAB bilayer with thiolated compounds[189, 190]. In the layer-by-layer technique, alternate layers of anionic and cationic polyectrolytes are deposited onto the gold surface via electrostactic interactions. Briefly, first a negatively charged polymer is incubated with AuNRs, decreasing the net charge from positive to negative and then a second layer is deposited on the surface using a cationic polymer, such as PEI. The thiol-gold bond chemistry has been explored for the replacement of the CTAB bilayer with thiolated compounds. The functionalization of AuNRs with alkyl thiols like mercaptoundecanoic acid and mercaptohexanoic acid was achieved through a round trip phase transfer[191]. In this methodology, the nanorods are transferred to an organic phase with acetone and dodecanethiol and then are reacted with an alkyl thiol at high temperature, becoming water soluble. The surface exchange under aqueous conditions has also been reported, for example, using PEG thiols to improve stability and biocompatibility[104, 192, 193]. In 2011, Vigderman *et al*[189] reported the complete exchange of CTAB with an analogue MTAB (mercaptohexadecyl)trimethylammonium bromide) that binds directly to the gold surface and confers increased stability to the nanorods.

AuNRs can also be conjugated with a variety of molecules, such as peptides, aptamers and antibodies for biosensing applications[153, 194], cell targeting[195, 196] and payload delivery[32, 103, 175]. In particular, conjugation of gold nanoparticles with DNA has been explored for these applications and also to create building blocks for the formation of self-assembled nanostructures[197]. Immobilization of ssDNAs modified with thiol group on AuNRs stabilized with CTAB was reported[139]. However, high ratios of ssDNA to AuNRs should be used in order to prevent aggregation promoted by the electrostatic interaction between anionic DNA phosphates and CTAB and consequent charge neutralization. The thiol-gold chemistry has been used to functionalize anionic citrate-stabilized gold nanoparticles with thiolated DNA strands[198]. However, in the case of CTAB-stabilized gold nanorods, this strategy is very difficult to employ due to the prevalence of strong electrostatic interactions and to the high density of surfactant that decreases the access of thiol-modified DNA to the gold surface. To overcome this, researchers have explored ligand exchange with short chain alkanethiols[191] or with a mixture of small molecules (sodium dodecylsulfate) and polymers (polyvinylpyrrolidone)[199] that could then be easily replaced by thiol-modified-ssDNA. In these methodologies, AuNRs become negative after ligand exchange and this

requires addition of salt solutions to decrease the electrostatic repulsion between DNA strands and the nanorod surface. A recent study demonstrated that the CTAB bilayer could be displaced using a mixture of mPEG-thiol and Tween 20[200]. The amount of oligonucleotides immobilized (between 50 and 250) could be tuned by changing the amount of mPEG-thiol and Tween 20 used in the displacement process. Other strategy is based on the encapsulation of gold nanorods in a thin silica coating. The surface of this silica layer is then modified to bind amine or thiol-functionalized oligonucleotides[201].

DNA-conjugated gold nanorods have also been used for hybridization of complementary DNA strands. Interestingly, several works have reported the use of ssDNA spacers in gold surfaces or spherical nanoparticles as a strategy to increase hybridization efficiency[202, 203] . Usually, the ssDNA that is bound to the surface has a poly-thymine spacer (between 10 and 15 thymines) that separates from the surface the sequence that hybridizes with complementary strands. These spacers have been adopted due to the lower interaction between thymine and gold when compared to the other nucleotides [204], reducing hindrance effects and increasing chain flexibility. For immobilization of double stranded DNAs on gold nanorods two strategies were described. One is based on the hybridization of ssDNAs of variable length (between 15 and 50 bases) on CTAB-functionalized gold nanorods conjugated with ssDNAs[139]. Complementary strands were designed with the same number of nucleotides and without any spacer in order to have full complementarity. However, the authors did not provide quantification of DNA immobilization and hybridization for each of the strands. In the other approach, hybridization of complementary DNA strands is performed first at 95 ºC, followed by immobilization of DNA duplex on gold nanorods[103].

Interestingly, it has been shown that surface functionalization has impact on the thermal dissipation from gold nanorods [205]. In relation to this, for applications that rely on the melting of the nanorod upon irradiation, one should use ligands that do not promote heat dissipation, whereas for applications relying on the increase of temperature in the vicinity of the nanorod, ligands should promote heat dissipation.

## 1.5 - Nanoparticle uptake and intracellular trafficking

One of the challenges associated to the development of nanocarriers is related to their uptake and intracellular trafficking, which has impact on the dose and bioavailability of the drugs delivered intracellularly.

The plasma membrane is a dynamic structure of lipid bilayers and membrane proteins that segregates the chemical distinct intracellular milieu from the extracellular environment regulating the entry and exit of molecules. Essential small molecules and ions can enter in

the cell through a system of protein pumps and channels, whereas macromolecules and nanostructures are transported into the cell in membrane bound vesicles through mechanistically diverse and highly regulated endocytic pathways[206, 207] (**Figure 1.11**). Endocytosis has been classified in two broad categories: phagocytosis (uptake of large particles) and pinocytosis (uptake of fluids and solutes). Phagocytosis is restricted to certain types of mammalian cells and pinocytosis occurs in all cells. Pinocytosis can occur by at least four different mechanisms: macropinocytosis, clathrin-mediated endocytosis, caveolae-mediated endocytosis, and clathrin and caveolae independent endocytosis. Endocytosis is a multiple step process. After interaction with the cell membrane, the cargo enters in the cell following invagination of the membrane, which leads to the formation of intracellular vesicles, also known as endosomes. Then, sorting of the entrapped cargo occurs, leading to different itineraries. Part of the endocytosed cargo may be recycled back to the membrane and exocytosed. Other part can go through trafficking from early endosomes to late endosomes and lysosomes for degradation or to the trans-Golgi network. The trafficking to the lysosomes occurs via acidification of the endosomes from pH 6.0 to pH 4.9 by the action of ATPase proton pumps. Late endosomes can then fuse with lysosomes (pH 4.5) where the low pH facilitates substrate denaturation and aids several degradative enzymes to digest the vesicular content.

It has been shown that nanoparticle uptake is highly dependent on their physicochemical characteristics. Charge is one of the most important factors driving nanoparticle uptake via interaction with the negatively charged phospholipid head groups or protein domains on the cell membrane, which is favourable for positively charged nanoparticles. Size and shape also influence nanoparticle uptake. For example, spherical gold nanoparticles are more easily internalized than gold nanorods[21], which is attributed to a greater membrane wrapping time required for elongated nanoparticles[208]. Surface chemistry plays an important role in uptake as well. Interestingly, not only the type of ligands but also their arrangement on the nanoparticle surface influence the interaction with the cell membrane [208].

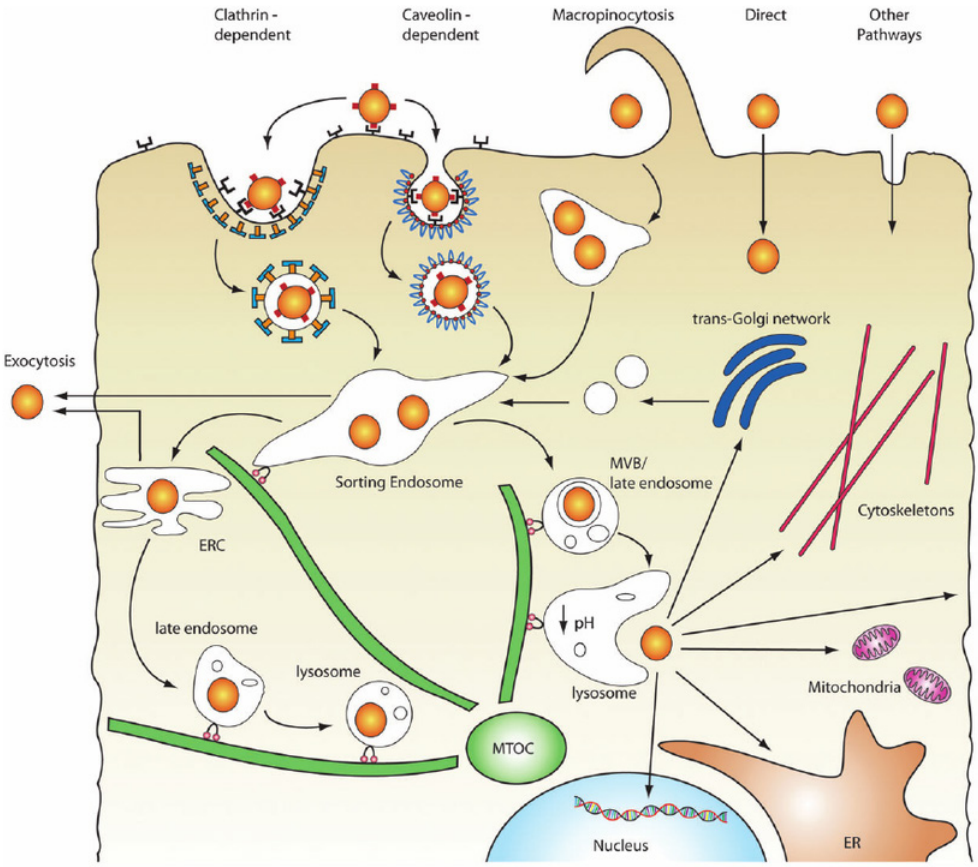


**Figure 1.11 - Endocytic pathways and intracellular trafficking**. The endocytic pathway can be initiated by different mechanisms. After internalization, nanoparticles are trafficked along the endolysosomal network within vesicles with the help of motor proteins and cytoskeletal structures. Vesicles can transport their contents into sorting endosomes, or excrete/recycle them back to the cell surface by fusing with the plasma membrane. Alternatively, endosomes can mature into lysosomes via luminal acidification and recruitment of degradative enzymes, which target the vesicle contents for degradation. In order to access cytoplasmic, nanoparticles must be capable of escaping from the endolysosomal network**.** (Image from ref.[209])

## 1.5.1 - Strategies for endosomal escape

The biological activity of small drugs or macromolecules, such as siRNA or proteins carried in nanoparticles that are internalized via endocytosis may be hampered by their accumulation in the endosome and consequent hydrolytic and/or enzymatic degradation. Even if the cargo is not degraded, if it remains entrapped in the lysosomes it is unable to exert its effect in any other cell compartment. In order to overcome this problem and ensure cytosolic delivery of the drug, several approaches have been adopted. These can be divided in different categories, such as fusion with the lipid bilayer[210], proton sponge effect[211], pore formation[212] and photochemical mechanism[213].

For example, concerning transduction of proteins, the use of fused protein transduction domains has enabled a higher efficiency in uptake, usually through the endocytic pathway, however with a concomitant degradation of the protein decreasing its biological activity. A supercharged green fluorescent protein fused to Cre recombinase was reported to induce higher uptake and an extended temporal window during which Cre recombinase could escape into the cytoplasm[214]. Another recent strategy involves the co-incubation of the protein with an endosomolytic agent composed of a tetramethylrhodamine labelled dimerized TAT[120].

#### 1.5.1.1 - Membrane destabilization

Endosomal escape can only occur if the endosomal membrane is destabilized and becomes compromised or leaky. Until now, several agents have been used to directly destabilize the endosomal membrane through different mechanisms, such as membrane active peptides and cationic nanocarriers that interact directly with the endosomal membrane. For example, cationic lipoplexes are able to induce a flip-flop mechanism in the lipids of the endosomal membrane[215]. Negatively charged lipids of the cytoplasmatic leaflet of the membrane will revert their position to the luminal side of the endosome to interact with the cationic lipoplexes, which leads to a destabilization of the endosomal membrane.

Several peptides have shown membrane perturbing characteristics that can induce endosomal escape. Membrane-active peptides from viral and bacterial pathogens have proven to be able to interact with membranes triggering different mechanisms, such as membrane fusion, membrane disruption, translocation and pore formation (**Figure 1.12**). Well known examples of such peptides are found in the viral envelope, like the HA-2 subunit of the influenza virus hemagglutinin. This fusogenic peptide mediates a mechanism for the delivery of the viral genome to the cytosol[216]. In general, the interaction with the endosomal membrane is triggered by a change in the conformation of the peptide as the endosomal pH decreases. For example, GALA, an anionic synthetic peptide, was also found to undergo conformational changes when the pH of the surrounding environment drops from 7.0 to 5.0, changing from random coil to amphiphilic α-helix [217]. Addition of this peptide to cationic complexes has been able to increase endosomal escape[218, 219]. Another strategy to promote endosomal escape involves the use of agents to destabilize directly the endosomal membrane through the formation of pores. Antimicrobial peptides[220] and bacterial exotoxins[221] have been reported to follow this mechanism. These peptides tend to align and insert perpendicularly in the membrane to form a pore cooperatively and in a concentration dependent manner.

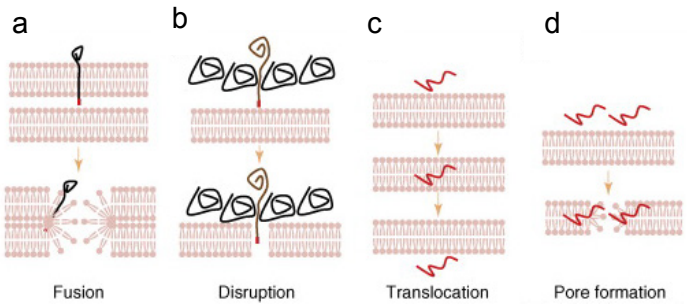


**Figure 1.12 - Schematic representation of membrane-perturbing mechanisms**. (a) Membrane fusion promoted by fusogenic peptides (red segments) that are usually found at the solvent-exposed ends of transmembrane proteins (black lines) of enveloped viruses. (b) Membrane disruption is promoted by endosome-disrupting peptides (red segments) of proteins (brown lines) that are usually embedded in protein macromolecular complexes (ex. in naked viruses). After membrane breakage, protein complexes can diffuse freely into the cell. (c) Translocation allows the membrane crossing of peptides and short proteins (red segments) without altering the physicochemical integrity of the cell membrane. (d) Pore formation is promoted by several types of antimicrobial peptides (red segments) that act cooperatively on localized areas of the cell membrane (Image from ref. [222])

### 1.5.1.2 - Antimicrobial peptides for endosomal escape

Antimicrobial peptides (AMPs) are a class of membrane-active peptides that have been studied for their ability in forming pores in biological membranes[220]. AMPs have a higher affinity towards microbial membranes, providing protection in multicellular organisms against bacteria, fungi and viruses[223]. The mode of action of these peptides on biological membranes differs from the mechanism of viral peptides which are essentially fusogenic[224]. AMPs are cationic amphiphilic molecules (15-45 amino acids) with nearly 50% of hydrophobic residues. They can adopt secondary structures with spatially separated hydrophobic and charged regions, conferring water solubility but also the ability to interact with phospholipid bilayers. Due to their membrane lytic properties, AMPs have already been used in different systems to increase endosomal escape. A recent study reported the ability of antimicrobial peptides to increase endosomal escape of proteins fused to superpositively charged GFP, without disrupting the cell membrane[225]. Melittin, a naturally occurring AMP, has been covalently attached to PEI gene delivery vectors to promote endosomal escape[226, 227]. Melittin was also utilized to improve endosomal escape of hepatocyte targeted chol-siRNA leading to a 500-fold improvement in protein knockdown[228]. Recently, different amphiphilic peptide segments were combined with TAT peptide and a DNA binding segment for efficient cytosolic delivery of plasmid DNA[229]. Membrane-disruptive properties of a chimeric peptide in which $TAT_{11}$ motif was fused to hybrid peptide cecropin-melittin have been studied[230]. After reaching a critical concentration, the fusion peptide is able to

dissolve the bilayer integrity by a carpet mechanism, whereas the hybrid cecropin-melittin induces the formation of pores through a "toroidal pore" mechanism (**Figure 1.13**). The chimeric peptide has been already reported to enable the endosomal escape of membrane impermeable molecules[212].

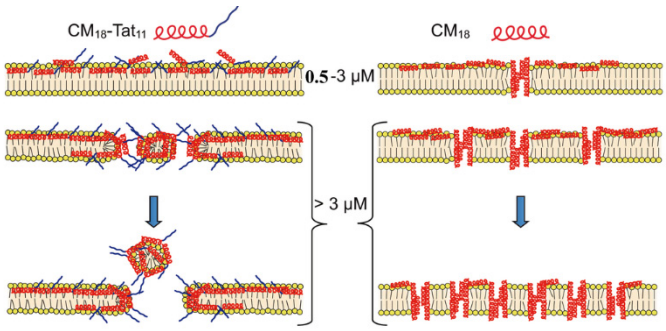


**Figure 1.13 - Schematic representation of membrane-perturbing mechanisms proposed for cecropin-melittin-TAT (CM18-TAT11) and for cecropin-melittin (CM18).** At concentrations above 3 μM, CM18-TAT11 acts through a carpet model disrupting the membrane in a detergent-like mechanism. CM18 induces the formation of toroidal pores in the membrane. The two hypothetical models were supported by patch-clamp analysis in Chinese Hamster Ovary (CHO-K1) cells exposed to different concentrations of peptides. (Image from ref. [230])

### 1.5.1.3 - Rupture of the endosomal membrane

Besides the induction of pores on the endosomal membrane, enabling the leakage of membrane impermeable molecules, other methods have been exploited for the rupture of the endosomal membrane.

#### Proton sponge effect

One of the most reported strategies for endosomal escape and, in particular, for efficient transfection of plasmid DNA, relies on the use of cationic polymers or lipids with excess protonable amine groups, which are able to generate a "proton-sponge" effect. Briefly, these polymers and lipids have high buffering capacity and tend to become protonated as the pH decreases, leading to an increased osmotic pressure with a consequent swelling and bursting of the endosome. Among these polymers, polyethyleneimine (PEI) is by far one of the most studied[211, 231]. Polyamidoamine (PAMAM) dendrimers and lipopolyamines have also achieved high transfection efficiency due to their buffering capacity[232, 233]. Recently, Perche *et al*[234] showed improved endosomal escape of

siRNA by conjugating gold nanoparticles with hydroxychloroquine, a small molecule that is able to produce an effect similar to the proton sponge effect described for PEI. Chloroquine is a weak base that is able to increase the pH of the acidic compartments and consequently inhibit hydrolytic enzymes such as proteases and nucleases[235]. Chloroquine also causes rupture of the endosomal membrane by increasing the osmotic pressure inside the endosome.

Endosomal escape can occur through a combination of proton sponge effect and other mechanisms. For example, dendrimers were found to expand and insert into the endosomal membrane, promoting rupture of the membrane at lower tensions, in addition to the proton sponge effect[236].

**Light-induced endosomal escape**

Several works have reported the use of light as an external stimulus for endosomal disruption. One of the strategies adopted for the spatio-temporal control of endosomal escape, relies on the use of photosensitizers that upon light excitation are able to produce singlet oxygen, inducing lipid peroxidation and disrupting the endosomal membrane[237]. In this approach, after internalization of the nanocarrier and photosensitizer through endocytosis, light is applied to promote endosomal escape of the nanocarrier. This methodology has been designated as photochemical internalization[237]. In 2010, Febvay *et al* [238] loaded a fluorescent dye in mesoporous silica nanoparticles, which after laser excitation originates a photochemical mechanism of endosome disruption through the production of reactive oxygen species. Harnessing this photochemical mechanism, Wang *et al*[239] reported the intracellular light-controlled delivery of antibodies targeting the Ki-67 protein in HeLa cells. This strategy has also been used for the delivery of siRNA[240, 241] with photosensitizers responsive to UV light. Recently, the photo-induced endosomal escape using wavelength in the NIR region was achieved with a formulation based on upconversion nanoparticles that upon irradiation at 980 nm emit visible light that excites a photosensitizer (mesotetraphenylporphine TPPS2a) which in turn produces reactive oxygen species for endosomal membrane destabilization [242].

Plasmonic gold nanoparticles also offer a means of controlling endosomal escape by light. Krpetic *et al*[243] demonstrated that CW irradiation of endocytosed gold nanoparticles with laser powers below 20 $Wcm^{-2}$ leads to the rupture of the endosomal membrane. The authors suggested that this was not a photothermal effect, since the increase in temperature was minimal and that it was probably mediated by reactive oxygen species (ROS) generated upon irradiation. Conversely, other authors have associated the mechanism of

endosome rupture to a thermal effect and cavitation triggered by irradiation of gold nanoshells with NIR pulsed laser[168].

## 1.6 – Outgrowth endothelial cells and miRNAs

Since the first work reporting the isolation of endothelial progenitor cells (EPCs)[244], extensive research has been done to leverage their therapeutic potential. EPCs can be isolated from peripheral blood, bone marrow and umbilical cord blood. Different subtypes of EPCs have been described. Early EPCs are spindle-shaped cells and can be obtained after short-term culture (4-7 days) of isolated mononuclear cells and regulate angiogenesis through the secretion of paracrine factors. Outgrowth endothelial cells (OECs) or late endothelial progenitors have a cobblestone morphology and can be derived from long term culture (2-3 weeks) of mononuclear cells. They are characterized by their high proliferative potential[245] and also by the unique capacity of contributing to the formation of functionally active vessels *in vivo* by differentiating into endothelial cells[246]. Therapies based on these cells may be extremely beneficial for the treatment of several diseases related to vascular ischemic injury, such as stroke[247], myocardial infarction[248], hind-limb ischemia[249] and ischemic retinopathies[250].

Regulatory pathways of endothelial cell-mediated vascular repair are being established in terms of transcriptional regulation of endothelial cells, epigenetic regulation, and post-transcriptional regulation with non-coding RNAs[251]. Research on the role of miRNAs in modulation of angiogenesis has been mostly focused on endothelial cells and less on progenitor endothelial cells[252]. A study identified dysregulation of some angiogenesis-related miRNAs in EPCs from patients with coronary artery disease (CAD)[253]. This suggests the important role of miRNAs on cell behaviour and creates new therapeutic possibilities to restore the function of these cells. MiRNAs could be helpful in: 1) enhancing the proliferation of cells available for cell-based therapies; 2) promoting the differentiation of vascular progenitor cells into endothelial cells; 3) improving the cell function by the amplification of proangiogenic pathways and 4) correcting antiangiogenic molecular defects.

MiRNAs have been identified as critical regulators of the neovascularization process. MiRNA profiles in early EPCs, OECs and human umbilical endothelial vein cells (HUVEC) have been identified[254]. Interestingly, it was found that 38 miRNAs are specifically expressed in OECs and 30 miRNAs are specifically expressed in early EPCs. A comparison between EPCs healthy old individuals and EPCs from young individuals revealed a significant down-regulation of several miRNAs, namely miR-221/222, miR-130a and miR-

155.[255]. In fact, miRNAs have been correlated with the modulation of EPCs at different levels. Some works have reported the impact of miRNAs in the proliferative potential of EPCs [256, 257]. It was reported that overexpression of miR-221 in bone marrow-derived EPCs reduced significantly their proliferation [257]. Interestingly, EPCs from patients with CAD have increased levels of this miRNA when compared to EPCs from healthy donors [258]. MiR-221 is also upregulated in mature endothelial cells, which is consistent with their less active nature. A study reported the anti-angiogenic impact of overexpressing miR-221 in OECs, affecting genes involved in hypoxia response, cell migration and energy supply[254]. Overexpression of miR-126 increases proliferation and decreases apoptosis by targeting SPRED1 [259]. It was found that the expression of this miRNA was downregulated during ischemia, enhancing mobilisation of progenitor cells[260]. MiRNAs also regulate the senescence of EPCs. It has been demonstrated that overexpression of miR-10A and miR-21 could induce senescence of EPCs, impairing their angiogenic functions. Inhibition of these miRNAs in aged EPCs resulted in higher angiogenic activity [261, 262]. Likewise, miR-34a was found to inhibit EPC-mediated angiogenesis by inducing senescence via repression of silent information regulator 1 (Sirt1).

MiRNAs 155 modulate endothelial cell activity [263, 264]. Recently, miR-155 was reported as an important modulator of adaptive neovascularization in mice [264]. The authors identified an anti-angiogenic but proarteriogenic activity of miR-155 by the direct suppression of different target genes, AGTR1 (positive modulator of angiogenesis) and SOCS-1 (negative feedback regulator of Janus Kinase/signal transducers and activators of transcription signalling in monocytes and macrophages). However, a separate study showed that ectopic expression of miR-155 in HUVEC increased cell proliferation, migration and VEGF-induced network formation, revealing a proangiogenic function [265]. Moreover, a recent study showed that miR-155 is a key promoter for endothelial cell maturation [266]. This study demonstrated that VEGF stimulation could promote miR-155 expression leading to improved endothelial cell functions, such as microtubule formation and secretion of paracrine factors, by the suppression of E2F2 transcription factor. Nanotechnology has been used in combination with different cells with angiogenic potential. Nanoparticles have been reported for mobilization of cells *in vivo*[267], tracking by imaging techniques[268] and also for drug delivery[269]. Although miRNAs have a critical role in the regulation of endothelial cells, EPCs and angiogenesis, very few nanoparticle-based systems have been developed to modulate these cells and their angiogenic potential through miRNA delivery [268, 270, 271]. Fluorine-containing PLGA nanoparticles were used to track transplanted endothelial cells by magnetic resonance imaging and to deliver a miRNA to exert a pro-survival effect under hypoxia [268]. In another study, PLGA nanoparticles were used to deliver proangiogenic miR-132 to endothelial cells before incorporation in protein gel constructs for transplantation [271].

Other studies have reported the delivery of miRNAs or miRNA inhibitors with nanoparticles for antiangiogenic therapies, as a potential tool for cancer treatment[272] and also for the treatment of diabetic retinopathy [273] .

# Chapter 2

## Intracellular delivery of more than one protein with spatio-temporal control

# Intracellular delivery of more than one protein with spatio-temporal control

Miguel M. Lino, Susana Simões, Sónia Pinho and Lino Ferreira*

CNC, Center for Neurosciences and Cell Biology and Faculty of Medicine, Polo III - Health Sciences Campus University of Coimbra, Rua Larga, 3004-517, Coimbra, Portugal

*Submitted for publication*

## Abstract

Transient, non-integrative modulation of cell function by intracellular delivery of proteins has high interest in cellular reprogramming, gene editing and therapeutic medicine applications. Unfortunately, the capacity to deliver intracellularly multiple proteins with temporal and spatial control has not been demonstrated. Here, we report a near infrared (NIR) laser-activatable nanomaterial that allows precise control over the release of two proteins from a single nanomaterial. The nanomaterial is formed by gold nanorods (AuNRs) modified with single stranded DNA (ssDNA) to which complementary DNA-conjugated proteins are hybridized. Using DNA strands with distinct melting temperatures we are able to control independently the release of each protein with a laser using the same wavelength but with different powers. Studies in mammalian cells show that AuNRs conjugated with proteins are internalized by endocytosis and NIR laser irradiation promotes simultaneously endosomal escape and the release of the proteins from the AuNRs. Our results further demonstrate the feasibility of protein release from a carrier that has been accumulated within the cell up to 1 day while maintaining its activity.

**Keywords**. Gold nanorods, protein delivery, nanotechnology, near infrared laser

# 2.1- Introduction

Intracellular delivery of proteins is extremely useful for the modulation of cellular processes, cell reprogramming and gene editing.[1, 274] In many cases, this type of delivery requires the use of protein carriers to overcome proteins poor membrane permeability. In the past decade, different nanoformulations have been developed to address this need.[275-277] Yet most of these strategies are based on the passive diffusion of the protein from the nanocarrier or on the enzymatic degradation of the nanoformulation.[10] Despite the recent successes in the intracellular delivery of functional proteins,[120, 278, 279] so far, no formulation has the capacity to orchestrate the intracellular delivery of more than one protein with remote control. This is an important issue in many biological applications such as cell reprogramming. For example, lineage-switching experiments in the hematopoietic system have shown that the order in which two transcription factors become expressed in a progenitor cell may define the commitment into a given lineage.[9]

Light-sensitive nanomaterials have emerged as an attractive solution to provide spatial and temporal control over the release of molecules within cells.[65] A significant number of light-triggerable formulations that respond to UV or visible light have been described.[122, 134, 238, 280, 281] Unfortunately, the UV light has a low penetration depth in biological samples and may exert cytotoxic effects[65]. AuNRs, having a large optical cross section and tuneable plasmon optical resonance in the near infrared range[282], are promising nanomaterials for *in vivo* controlled release of biomolecules. The NIR plasmon resonance band is attractive for biomedical applications due to the “water window” (650-900nm) where there is low light absorbance by skin and tissue. These AuNRs have been mostly used for the controlled release of nucleic acids such as siRNA, small oligonucleotides and plasmid DNA.[91, 139, 142] Upon optical excitation, DNA strands hybridized to complementary strands immobilized on the surface of the nanocarrier are released by a photothermal effect.[91, 103, 139] Released siRNAs may mediate gene silencing in model cells.[91]

Although light-triggered release of proteins has been reported,[122, 283] no formulation has achieved the photo-triggered release of more than one protein from the same nanocarrier using a single wavelength. In this work, we have developed a nanomaterial and oligonucleotide chemistry for the intracellular delivery of two proteins with spatio-temporal control using NIR light as a trigger. We further show that the released protein escapes the endolysomal compartment remaining active. Proteins were immobilized on AuNRs by hybridizing complementary single stranded DNA (ssDNA) molecules having different melting temperatures. For the NIR-triggered release we have used a continuous wave (CW) excitation. CW leads to a local increase of temperature creating a gradient from the AuNR core to the bulk solvent, but does not cause cavitation or melting of the AuNR core like

pulsed lasers.[180] Although the use of pulsed lasers has been used to induce the cleavage of Au-thiol bonds releasing biomolecules such as siRNA,[168] the selective release of cargos from the same nanocarrier is only possible with CW lasers. The current work opens new opportunities for the intracellular delivery of multiple proteins with spatio-temporal control.

# 2.2 - Results

## 2.2.1 - Preparation of AuNR-protein conjugates

The AuNRs used in this work had an average length of 46.7 ± 4.1 nm and width of 13.8 ± 1.9 nm and showed a plasmon resonance band at 780 nm (**Figure 2.2**). The AuNRs were coated with ssDNA containing a thiol terminal group at the 5′ end (**Table 2.1**, Materials and Methods) to facilitate the covalent attachment to the AuNR surface (**Figure 2.1**). The two ssDNA tested in this work had a poly-thymine spacer (12 or 15 thymines) followed by an oligonucleotide sequence of 15 or 13 bases, respectively. The poly-thymine spacer was used to keep the oligonucleotide hybridization sequence distant from the AuNR surface.[204] The number of ssDNA per AuNR ranged between 120 and 480 depending on the initial ratio of ssDNA per AuNR (**Figure 2.2b**). The coupling efficiency of ssDNA to AuNR was on average 60% and it was similar for both oligonucleotide strands (**Figure 2.2b**). The hybridization efficiency for the complementary oligonucleotide was above 90%. For subsequent experiments we have used AuNRs with 120 oligonucleotide strands because this number was large enough to immobilize the proteins selected in this study.

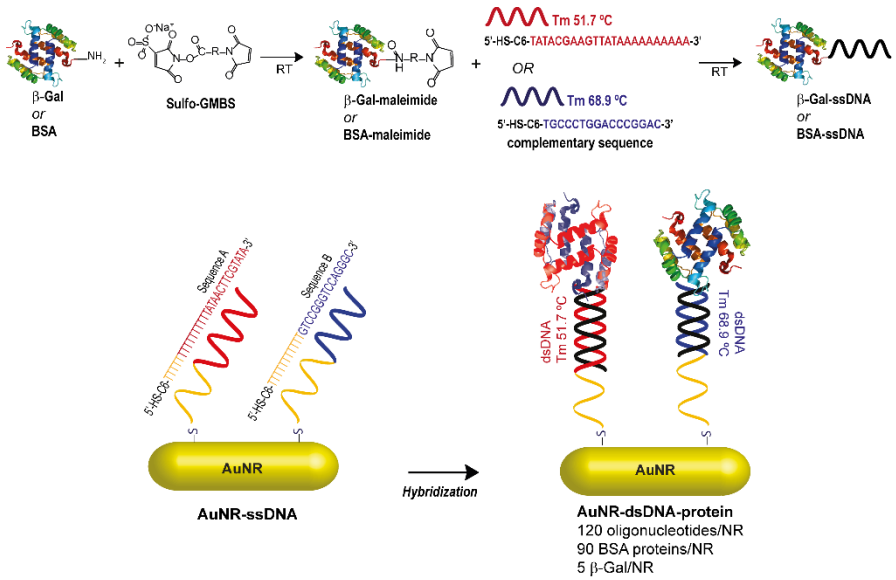


**Figure 2.1 - Preparation of AuNR-DNA-protein conjugates**. (a) Preparation of ssDNA-protein conjugates. Proteins (β-Gal or BSA) were initially reacted with a heterofunctional linker (Sulfo-GMBS) by its terminal succinimide ester. The protein conjugate was then reacted with a ssDNA having a terminal thiol group. After reaction, the protein conjugate (BSA-ssDNA or β-Gal-ssDNA) was purified by HPLC. (b) Preparation of AuNR-ssDNA. AuNRs were reacted with HS-ssDNA complementary to the strands of BSA-ssDNA or β-Gal-ssDNA conjugates. The ssDNA-protein conjugates were then bound to the ssDNA-AuNR by hybridization. Upon NIR irradiation, there is an increase in the temperature at the AuNR leading to the DNA de-hybridization and the release of proteins with different kinetics. The release kinetic depends on the heat generated (which depends on the power of NIR laser used) and the melting temperature of the oligonucleotides.

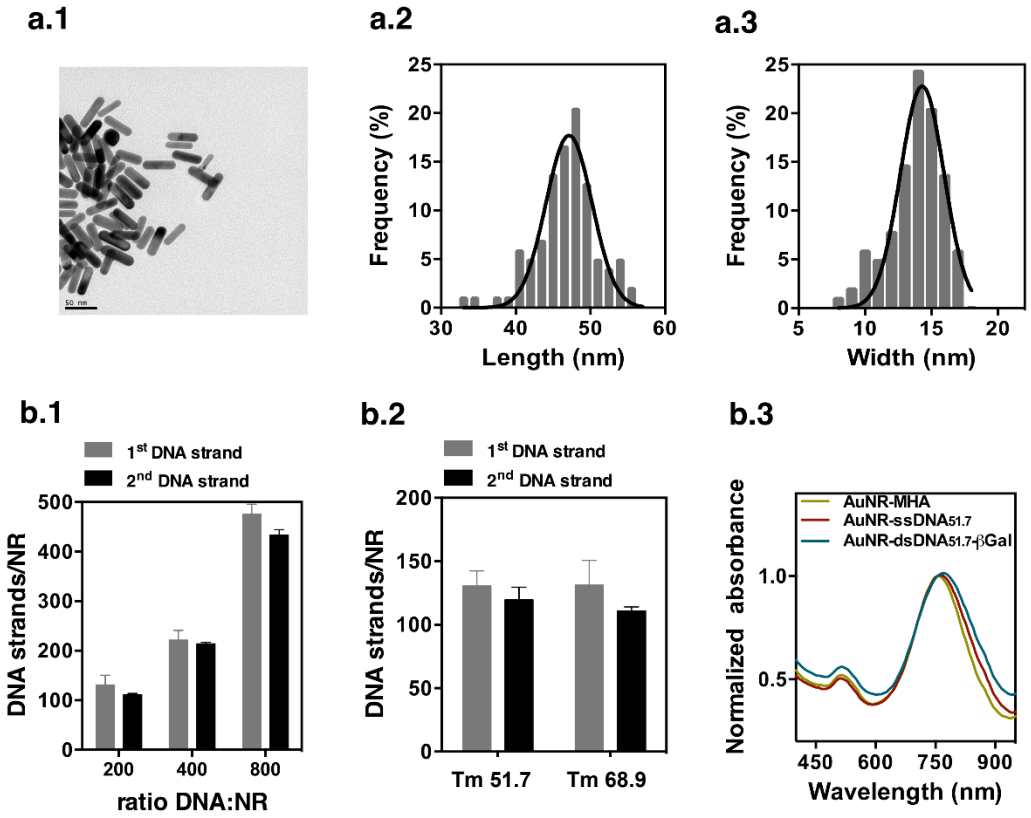


**Figure 2.2 - Characterization of AuNRs**. (a) TEM analysis. (a.1) Representative TEM image of AuNRs. (a.2-a.3) NR length (a.2) and width (a.3) distribution obtained from TEM images. The AuNRs showed an average length of 46.7 ± 4.1 nm, n=100 AuNRs and an average width of 13.8 ± 1.9 nm, n=100 AuNRs. (b.1) Quantification of oligonucleotides immobilized on NR surface via thiol gold chemistry (1st DNA strand) or hybridized to the ssDNA conjugated to the NR (2nd DNA strand). The amount of strands per AuNR was determined indirectly in the supernatant by measuring absorbance at 260 nm in Nanodrop. (b.2) Comparison of the binding efficiency of the two sequences with different melting temperatures (91.7% efficiency for DNA strand with Tm 51.7 ºC and 84.5% efficiency for DNA strand with Tm 68.9 ºC). Results in b.1 and b.2 are Average ± SD, n=3. (b.3) Absorbance spectra of AuNRs after conjugation with mercaptohexanoic acid (AuNR-MHA); after conjugation with ssDNA51.7 (AuNR-ssDNA$_{51.7}$) and after hybridization with β-Gal (AuNR-dsDNA$_{51.7}$-βGal). Surface plasmon resonance band does not change significantly during surface modification.

For initial experiments, bovine serum albumin (BSA) protein was used as a model protein due to its availability and easy to label with different fluorescent dyes. The protein was reacted with sulfo-GMBS followed by ssDNA containing a terminal thiol group (protein:ssDNA ratio of 1:2) (**Figure 2.1**). After purification, the protein conjugates had on average 1 ssDNA per protein molecule (**Figure 2.3**). The protein conjugate was then hybridized at 37 ºC, using a 300-fold excess of protein over AuNR concentration. Our results show that hybridization of the ssDNA-protein conjugate does not cause significant changes in the absorbance spectrum of the NRs (**Figure 2.2 b.3**). In addition, hybridization of the

ssDNA-protein conjugate to the AuNR was not observed when non-complementary ssDNA sequences were used.

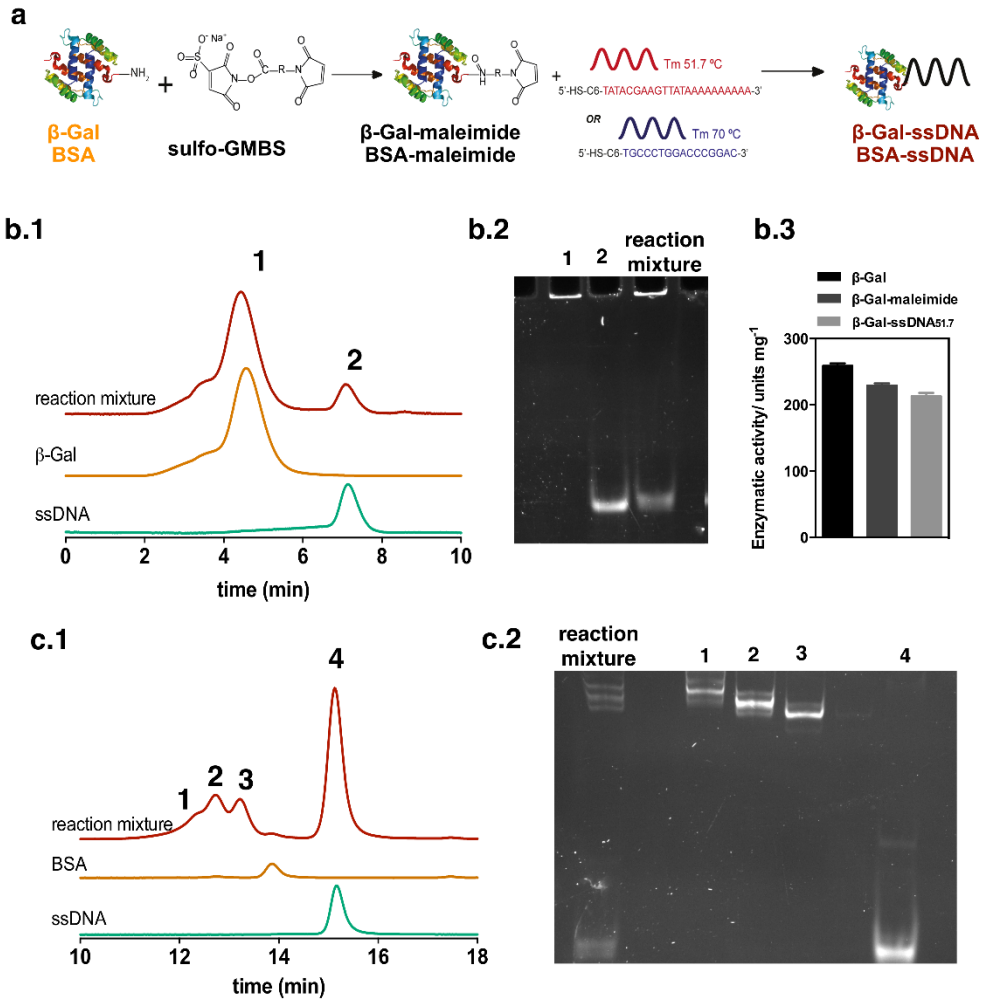


**Figure 2.3 - Characterization of oligonucleotide-protein conjugates**. (a.1) Scheme showing the coupling reaction of ssDNA to the proteins. (a.2) HPLC characterization of the reaction mixture between β-Gal and ssDNA. Representative chromatograms of β-Gal, ssDNA and the final reaction mixture of β-Gal with ssDNA. Integration of DNA peaks indicate a conjugation value of 37% of the total DNA. This means that each protein molecule was conjugated with at least one oligonucleotide. (a.3) Electrophoresis characterization of the HPLC fractions. Fractions 1 and 2 were analysed. Samples were run in polyacrylamide gel and DNA was stained with Sybr Gold. Quantification of free DNA indicates a conjugation value of 35% of the total DNA. Fraction 1, which corresponds to the β-Gal-ssDNA conjugate was used for subsequent experiments. (a.4) Enzymatic activity of β-Gal, β-Gal conjugated with sulfo-GMBS (β-Gal-maleimide) and β-Gal conjugated with $ssDNA_{51.7}$ (β-Gal$ssDNA_{51.7}$). (b.1) HPLC characterization of the reaction mixture between BSA and $ssDNA_{51.7}$.Representative chromatograms of BSA, ssDNA and the final reaction mixture of BSA with ssDNA. (b.2) Electrophoresis characterization of the HPLC fractions. Fractions 1-4 were analysed. Fraction 3 was used for conjugation with AuNR-ssDNA. We selected this fraction because each protein is conjugated with one ssDNA.

### 2.2.2- *In vitro* release of proteins from AuNR-protein conjugates after NIR laser activation

To study the release profiles of proteins, we have used AuNRs hybridized with: (i) DyLight$_{488}$-BSA conjugated with ssDNA with a melting temperature of 51.7 ºC (DL$_{488}$-BSA-ssDNA$_{51.7}$), (ii) BSA-DyLight$_{550}$ conjugated with ssDNA with a melting temperature of 68.9 ºC (DL$_{550}$-BSA-ssDNA$_{68.9}$), and (iii) both DL$_{488}$-BSA-ssDNA$_{51.7}$ and DL$_{550}$-BSA-ssDNA$_{68.9}$ (**Figure 2.4**). Each of the AuNR formulation has approximately 90 BSA molecules per NR. The AuNRs absorb the light and converted it into heat, which then disrupts the physical bonds between the double stranded DNA containing the proteins. BSA release correlated with laser power, i.e., higher concentration of BSA was released from AuNRs exposed to higher laser powers. Approximately 95% and 50% of the immobilized protein was released from DL$_{550}$-BSA-dsDNA$_{68.9}$-AuNR after a 5 min exposure to a laser power of 2 Wcm$^{-2}$ and 1.25 Wcm$^{-2}$, respectively (**Figure 2.4 b**).

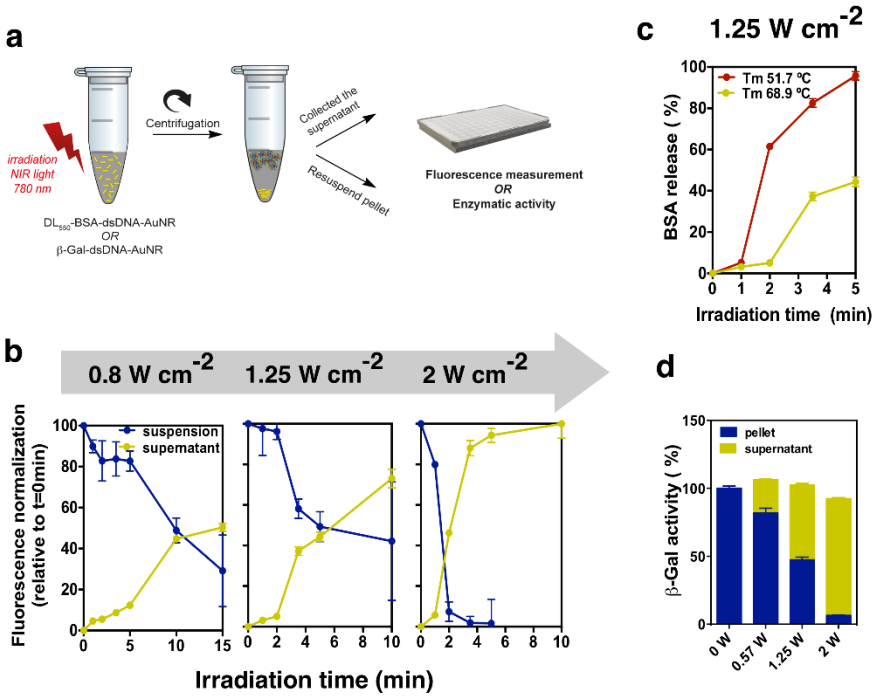


**Figure 2.4 - *In vitro* release of BSA-ssDNA or β-Gal-ssDNA from AuNRs conjugated with complementary ssDNA**. (a) Schematic representation of the *in vitro* release experiments. Fluorescently-labeled-protein-dsDNA-AuNR were irradiated by a NIR laser (780 nm) up to 15 min after which the suspension was centrifuged and the protein fluorescence (BSA) or the enzyme activity (β-Gal) measured both in the supernatant and pellet. (b) Release profile of BSA from DL$_{550}$-BSA-dsDNA$_{68.9}$-AuNR irradiated with different NIR laser powers up to 15 min. (c) Release profiles of BSA from DL$_{550}$-BSA-dsDNA$_{68.9}$-AuNR or DL$_{488}$-BSA-dsDNA$_{51.7}$-AuNR, irradiated with a NIR laser (780 nm; laser power: 1.25 Wcm$^{-2}$) up to 5 min. (d) Relative β-Gal activity in the supernatant and in the pellet after release from β-Gal-dsDNA$_{51.7}$-AuNR. Each β-Gal activity after laser irradiation was normalized by the total enzyme activity before laser irradiation. In b, c and d, results are Average ± SD (n=3).

In addition, for the same laser power, release of BSA correlated with the melting temperature of the ssDNA, i.e., higher concentration of BSA was released from AuNRs conjugated with ssDNA with low ($DL_{488}$-BSA-$ssDNA_{51.7}$-AuNR) than with high ($DL_{550}$-BSA-$dsDNA_{68.9}$-AuNR) melting temperature (**Figure 2.4 c**).

To demonstrate the dual release of proteins, we have immobilized both $DL_{550}$-BSA-$ssDNA_{68.9}$ and $DL_{488}$-BSA-$ssDNA_{51.7}$ in the same AuNR. The samples were irradiated for 2 min at 1.25 $Wcm^{-2}$, centrifuged, the pellet resuspended and irradiated for 3.5 min at 2 $Wcm^{-2}$ (**Figure 2.5 a**). Our results show that in each laser exposure, one of the proteins was preferentially released (**Figure 2.5 b**). The release of the first protein ($DL_{488}$-BSA-$ssDNA_{51.7}$) was 86%, which is higher than the value achieved in the single protein system. This may be due to a hindrance effect promoted by the other protein ($DL_{550}$-BSA-$ssDNA_{68.9}$) that is not released by the first stimulus and thus decreasing the possibility of re-hybridization of the released conjugate. Alternatively, a change in the melting transition of the DNA strands in the dual protein system versus single protein system may account for the differences observed.[284]

A recent study has inferred about the stability of proteins released from a NIR-activated Au nanoshell but definitive evidence about its stability was not provided.[122] To investigate whether the photothermal effect observed in AuNRs could reduce the activity of the attached protein, we immobilized a model enzyme, β-galactosidase (β-Gal), in the AuNRs and quantified its activity before and after light activation. The conjugation of β-Gal with $ssDNA_{51.7}$ was not deleterious for the enzymatic activity of β-Gal (**Figure 2.3 a.4**). Each of the NR formulation has a final amount of approximately 5 β-Gal molecules per AuNR due to the large molecular weight of the protein (464 KDa). Enzymatic activity was observed in the released enzyme (88% activity in the supernatant and 6% in the NR suspension after 2 min at 2 $Wcm^{-2}$, relatively to the initial enzymatic activity), which indicates that the photothermal effect in AuNRs had a minimal impact in the enzyme activity (**Figure 2.4 d**).

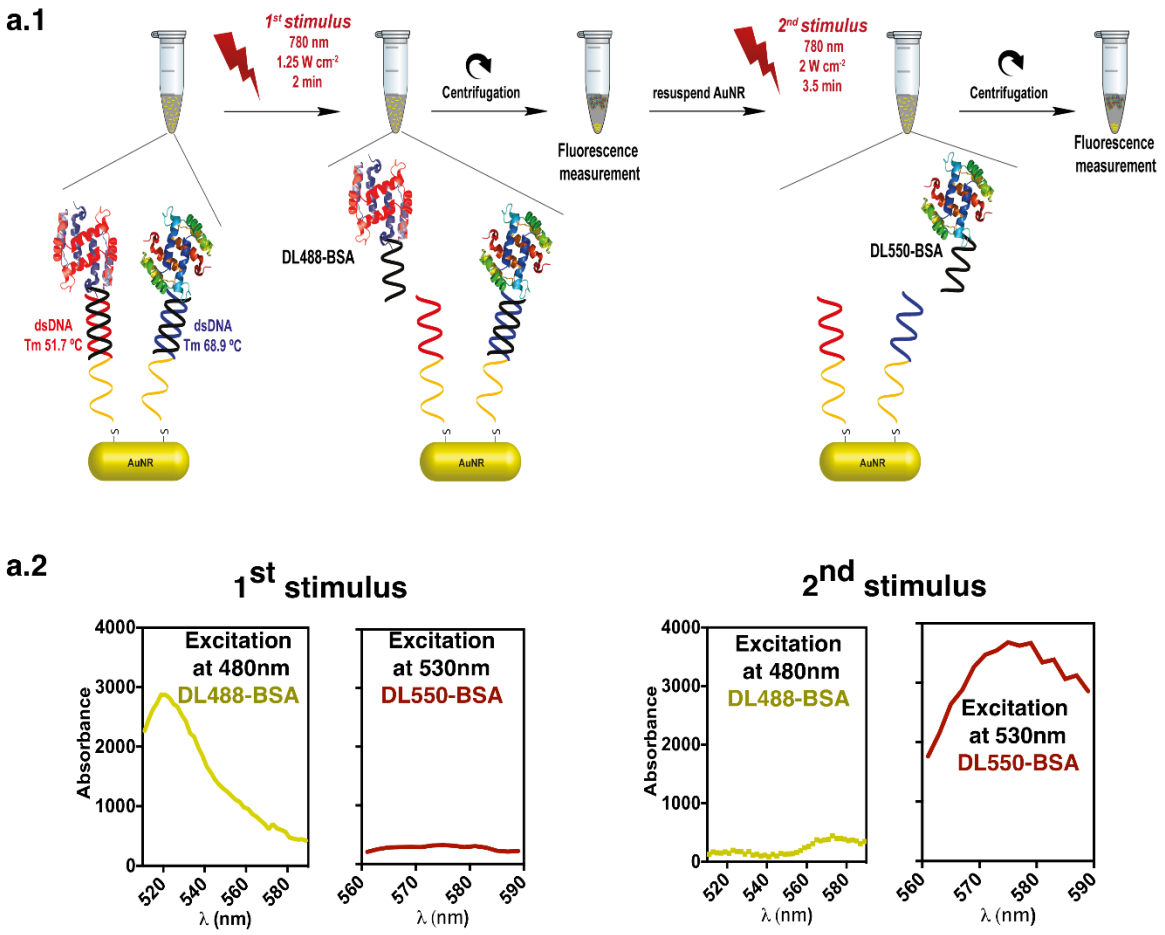


**Figure 2.5 - Sequential release of $DL_{488}$-BSA-$ssDNA_{51.7}$ and $DL_{550}$-BSA-$ssDNA_{68.9}$ from AuNRs after light activation**. (a.1) Scheme illustrating dual release experiment. A suspension of $DL_{488}$-BSAdsDNA$_{51.7}$-AuNR-$DL_{550}$-BSA-dsDNA$_{68.9}$ was first irradiated for 2 min at 1.25 $Wcm^{-2}$ and then centrifuged in order to collect the supernatant. The NR were resuspended and irradiated again at 2 $Wcm^{-2}$ for 3.5 min and then centrifuged. AuNRs used in this experiment were conjugated with 32 molecules of $DL_{488}$-BSA-$ssDNA_{51.7}$ and 34 molecules of $DL_{550}$-BSA-$ssDNA_{68.9}$. (a.2) The fluorescence of both supernatants was measured in a fluorimeter using an excitation wavelength at 480 nm for $DL_{488}$-BSA or 530 nm for $DL_{550}$-BSA. The first stimulus caused the release of 86% of $DL_{488}$-BSA and 7% of $DL_{550}$-BSA. The second stimulus released 14% of $DL_{488}$-BSA and 93% of $DL_{550}$-BSA.

## 2.2.3 - Uptake and cytotoxicity of AuNRs

Next, we evaluated the interaction of AuNRs with cells. We have selected fibroblasts as a cell model since many of reprogramming protocols used fibroblasts as a starting point.[117] Initially, we evaluated potential cytotoxic effects of AuNRs (we have used BSA-dsDNA$_{51.7}$-AuNR as a model) and light in cells. AuNRs (up to 50 μg $mL^{-1}$, with or without light activation) and light (up to 2 $Wcm^{-2}$) alone had a low cytotoxic effect (below 20%) (**Figure 2.6**). Then, we quantified cellular uptake of AuNRs using inductively coupled mass

spectrometry (ICP-MS) (**Figure 2.6 b.1**). Cells were incubated with AuNRs (50 μg $mL^{-1}$) for different times in DMEM (with 10% FBS), washed and finally characterized by ICP-MS. Each single cell internalized approximately 3.9 pg of AuNRs during the first 4 h (**Figure 2.6 b.1**). Cell uptake of NRs was not substantially improved for exposure times above 4 h. In addition, the intracellular accumulation of AuNRs depends on cell proliferation. If cell proliferation was inhibited with mitomycin C, 75% of the initial content of AuNRs remained in the cytoplasm after 24 h of cell culture (**Figure 2.6 b.2**).

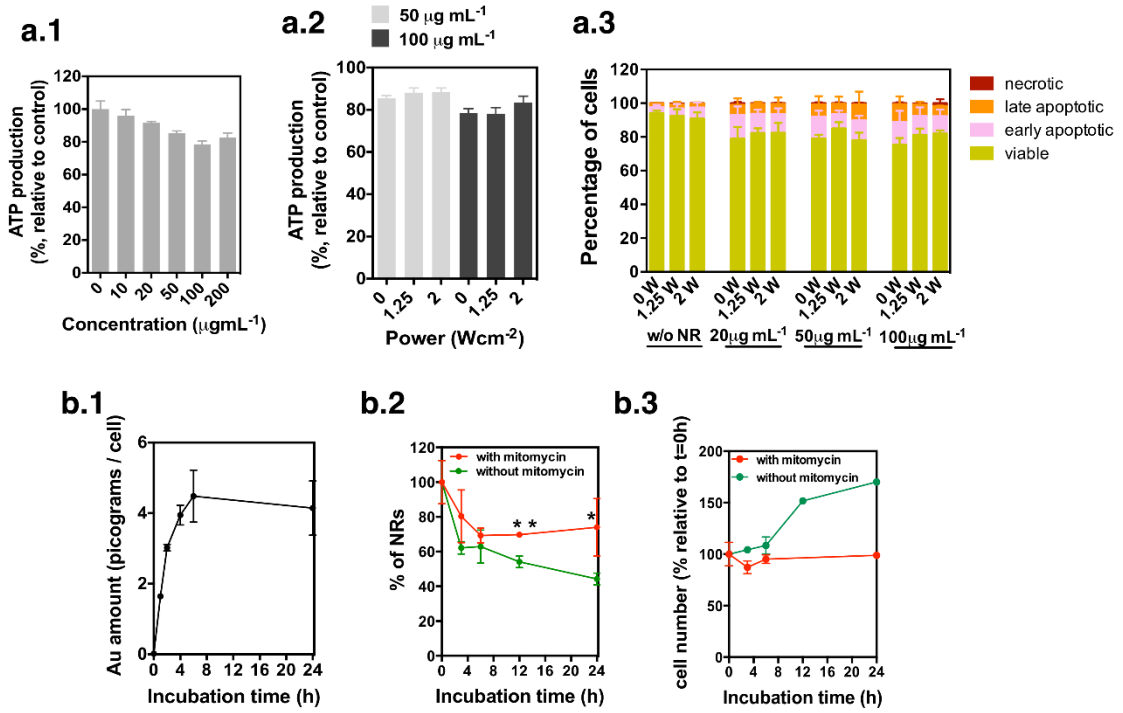


**Figure 2.6 - Cytotoxicity and uptake of protein-conjugated AuNRs**. Fibroblasts were incubated with different concentrations of BSA-dsDNA$_{51.7}$-AuNR for 4 h, washed, incubated in cell culture media for 20 h, after which cell metabolism (a and b) or cell viability (c) was evaluated by an ATP (a and b) or annexin V/PI (c) assays. Control are cells cultured without AuNRs. (a and b) Cytotoxicity of non-irradiated BSA-dsDNA$_{51.7}$-AuNR (a) and irradiated BSA-dsDNA$_{51.7}$-AuNR (780 nm laser for 2 min; laser powers: 1.25 and 2 $Wcm^{-2}$) (b) as evaluated by an ATP assay. (c) Cytotoxicity of non-irradiated and irradiated BSA-dsDNA$_{51.7}$-AuNR as measured by an annexin V/PI assay. b.1) Amount of Au in cells incubated with β-Gal-dsDNA$_{51.7}$-AuNR (50 μg mL-1) for different times. At each incubation time, cells were washed to remove non-internalized AuNRs and then trypsinized, counted and freeze-dried for ICP-MS analysis. (b) Amount of internalized Au during fibroblast proliferation. Cells were incubated with β-Gal-dsDNA$_{51.7}$-AuNR (50 μg $mL^{-1}$) for 4 h, washed to remove the non-internalized AuNR, and cultured for additional 0, 3, 6, 12 and 24 h in cell culture media. In a set of experiments, cells were treated with mitomycin for 150 min after the 4 h uptake period. To determine the Au amount in the cells treated or not with mitomycin, cells were trypsinized, counted and freeze-dried for ICP-MS analysis. (b.1) Intracellular content of Au as quantified by ICP-MS. (b.3) Cell number relative to time 0 h (end of the incubation with NR). Results are Average ± SD, n=3. In b.2, unpaired t-test was used to compare both groups. * and ** mean $p<0.05$ and $p<0.01$.

### 2.2.4 - Intracellular release of a single protein from AuNR-protein conjugates after NIR laser activation

To demonstrate the release of proteins within the cell after light activation, fibroblasts were incubated with $DL_{488}$-BSA-$ssDNA_{68.9}$-AuNRs-TRITC (TRITC was attached to the Au core of the NR by a polyethylene glycol linker) for 4 h, washed to remove non-internalized AuNRs and finally activated by a NIR laser with variable power (1.25 or 2 $Wcm^{-2}$) for 2 min (**Figure 2.7 a**). Irradiated fibroblasts showed higher fluorescence (in the green and red channel) as compared to non-irradiated cells (**Figure 2.7 b.1**). This result confirms the laser-induced release of the protein, which results in less proximity between $DL_{488}$-BSA-$ssDNA_{68.9}$ and AuNRs and a decrease in the quenching effect.[285] Our results further show that an increase in laser power correlates with an increase in fluorescence (i.e. "corrected total cell fluorescence") (**Figure 2.7 b.2**), supporting the thesis that more protein is released for higher laser powers. To gain further insights about the release of the protein, the coefficient of variation (CV) of protein signal (**Figure 2.7 b.3**) and Manders' colocalization coefficient (**Figure 2.7 b.4**) between AuNR-TRITC and $DL_{488}$-BSA-$ssDNA_{68.9}$ were determined. Both Manders' colocalization coefficient and CV of the total cell fluorescence decreased for higher laser powers, which is an indication of protein diffusion in the cells. However, in the non-irradiated cells, the Manders' colocalization coefficient between AuNR and BSA is not 100% probably due to the proximity between TRITC and the AuNR surface, which may result in a quenching of TRITC fluorescence.[285, 286] Therefore, part of the AuNR-TRITC fluorescence is not detected under confocal microscope, decreasing the colocalization coefficient between DyLight and TRITC.

To understand the fluorescence overlap we used the Forster Resonance Energy Transfer (FRET) acceptor photobleaching method (**Figure 2.8**). This technique measures the donor fluorescence ($DL_{488}$-BSA-$ssDNA_{68.9}$) before and after photobleaching the acceptor (AuNR-TRITC). The efficiency of FRET is mainly based on the donor-acceptor separation distance [287]. If the molecules are close enough (2-10 nm), a resultant increased fluorescence will occur on the donor ($DL_{488}$-BSA-$ssDNA_{68.9}$). Confocal images in fibroblasts show an increase in $DL_{488}$-BSA-$ssDNA_{68.9}$ fluorescence after photobleaching the acceptor (AuNR-TRITC) (Fig. 4b). The FRET efficiency in non-irradiated cells is higher than in irradiated cells indicating that the distance between AuNR-TRITC and $DL_{488}$-BSA in non-irradiated cells is shorter than in irradiated cells. These results suggest that, although the protein and the AuNR core co-localize within cells, the protein is not bound to the AuNR in the irradiated cells.

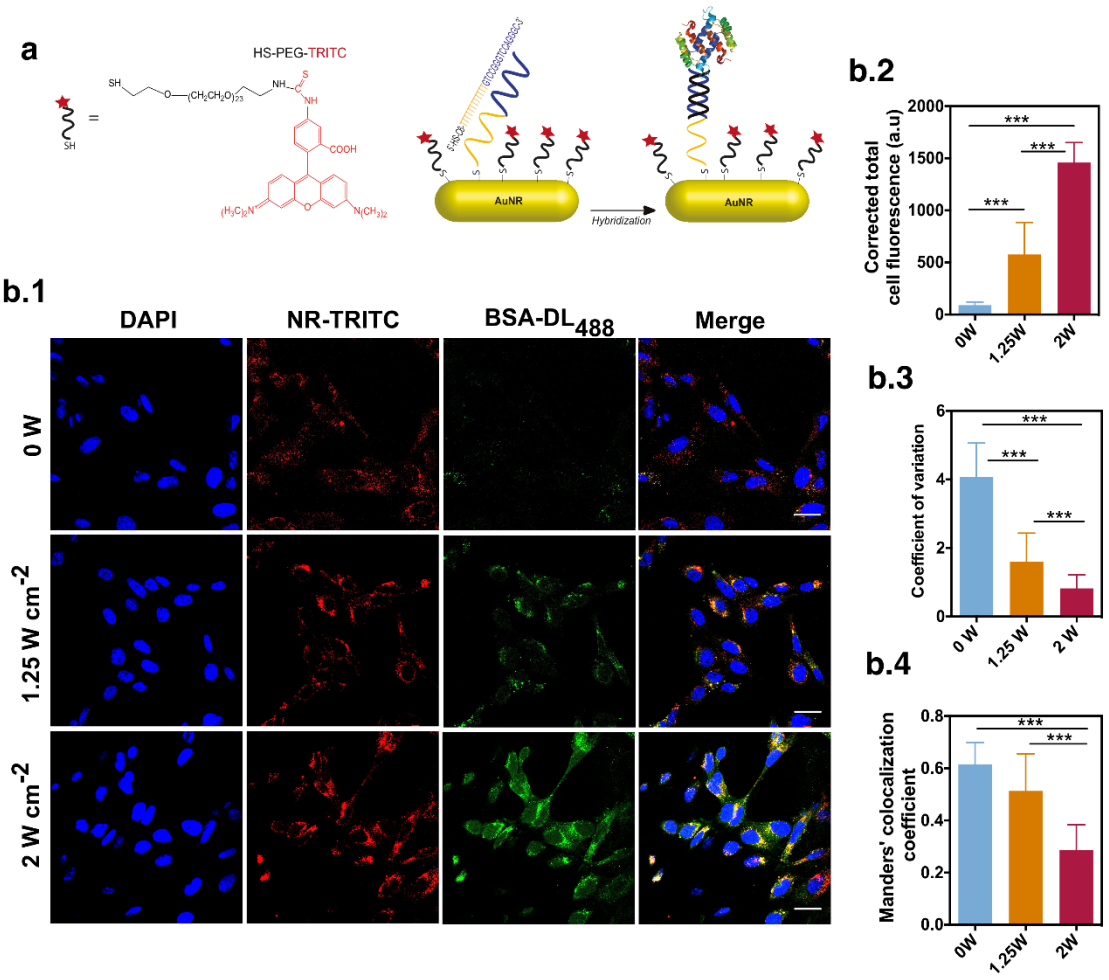


**Figure 2.7 - Intracellular release of proteins**. Fibroblasts were incubated with $DL_{488}$-BSA-$dsDNA_{68.9}$-AuNR-TRITC for 4 h, washed, new cell culture media added and finally irradiated with a laser at 780 nm (laser power: 1.25 or 2 $Wcm^{-2}$) for 2 min. (a) Schematic representation for the preparation of $DL_{488}$-BSA-$dsDNA_{68.9}$-AuNR-TRITC. The stoichiometry between ssDNA and TRITC is 1:4.5. (b.1) Representative confocal images of fibroblasts after incubation with $DL_{488}$-BSA-$dsDNA_{68.9}$-AuNR with and without laser irradiation. Scale bar is 30 µm. (b.2 and b.3) Intensity and coefficient of variation of the signal of $DL_{488}$-BSA-$ssDNA_{68.9}$. (b.4) Colocalization between AuNR-TRITC and $DL_{488}$-BSA-$ssDNA_{68.9}$ expressed as Manders' overlap coefficient assessed by ImageJ analysis. In b.2-b.4, the results are expressed as Average ± SD (n=3). *** denotes statistical significance ($p<0.001$) assessed by one-way ANOVA followed by Tukey's post-hoc test.

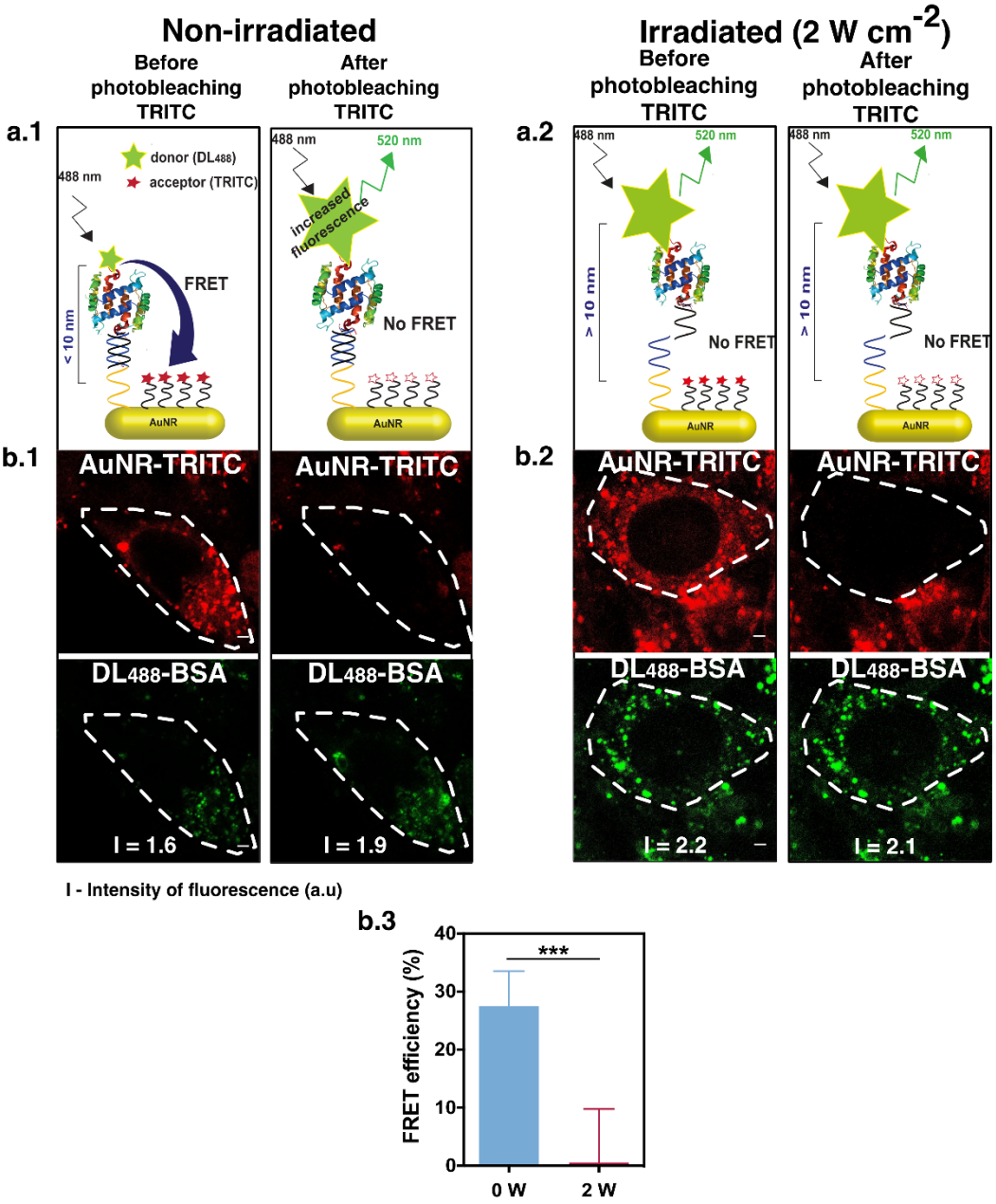


**Figure 2.8 - FRET analysis to evaluate the proximity of the protein to the AuNR-TRITC**. (a.1 and a.2) Schematic representation of the acceptor photobleaching FRET method. $DL_{488}$ works as donor, transferring energy to the acceptor (TRITC). If the distance between the pair is less than 10 nm, when the acceptor is photobleached, the fluorescence of the donor increases. (b) Fibroblasts were incubated with $DL_{488}$-BSA-$dsDNA_{68.9}$-AuNR-TRITC (50 μg $mL^{-1}$) for 4 h, washed, feeded with new cell culture media, and either irradiated or not with a 780 nm laser for 2 min (2 $Wcm^{-2}$). (b.1 and b.2) Confocal images of AuNR-TRITC and $DL_{488}$-BSA-$ssDNA_{68.9}$ before and after photobleaching TRITC within a region of interest (ROI, each ROI corresponds to one cell) with confocal 561 nm laser (80% of intensity). Scale bar is 6 μm. (b.3) Quantification of FRET efficiency. FRET efficiency (FRETeff) was calculated as FRETeff = ([Dafter]-[Dbefore])/[Dafter])x100, where Dafter is the fluorescence intensity of the donor ($DL_{488}$) after photobleaching the acceptor (TRITC), and Dbefore is the fluorescence intensity of the donor before photobleaching the acceptor. Results are Average ± SD (n=10 cells, ***$p < 0.001$).

Next, we studied whether the protein cargo after light activation was entrapped in the endolysosomal compartment or released in the cytoplasm. Fibroblasts were incubated with BSA-dsDNA$_{51.7}$-AuNRs for 4 h, washed, activated or not by a NIR laser (1.25 Wcm$^{-2}$) for 2 min and then fixed. The intracellular trafficking of NRs was then studied by transmission electron microscopy (TEM) (**Figure 2.9 a**). In the absence of laser irradiation, BSA-dsDNA$_{51.7}$-AuNRs accumulated in vesicles (almost 90%) specifically in endosomes (67.0% ± 1.0%) and lysosomes (21.2% ± 1.0%). After laser irradiation (2 Wcm$^{-2}$), most BSA-dsDNA$_{51.7}$-AuNRs accumulated in the cytoplasm (57.8% ± 3.4%) while the remaining AuNRs were entrapped in endosomes (35.7% ± 3.0%) and lysosomes (6.5% ± 0.8%) (**Figure 2.9 b**). In a separate experiment, using the previous incubation protocol, we monitored the intracellular trafficking of BSA-dsDNA$_{51.7}$-AuNR-TRITC using an endolysosomal dye, Lysotracker (**Figure 2.10**). In the absence of light, the number of AuNRs in the cytoplasm was 34.8 ± 5.5% (more than observed by TEM; however, this dye might not take into account the AuNRs accumulated in early endosomes [288]) while after laser irradiation, the number of AuNRs in the cytoplasm was 62.4 ± 6.4%.

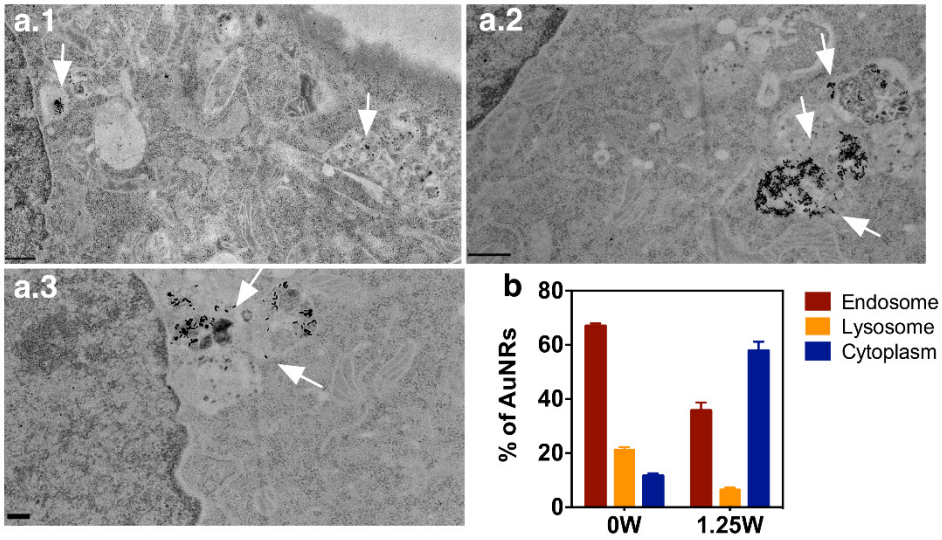


**Figure 2.9 - Laser induced endosomal escape**. (a) TEM images of fibroblasts incubated with BSA-dsDNA$_{51.7}$-AuNR for 4 h before (a.1) and after (a.2 and (a.3) laser irradiation (2 min at 1.25 Wcm$^{-2}$). In a.1, white arrows indicate the presence of AuNR accumulated in vesicles. Figures a.2 and a.3 are representative TEM images of endosomal damage induced by laser irradiation with rupture of the endosomal membrane and consequent escape of the AuNR to the cytoplasm. In a.1, a.2 and a.3, N means cell nuclei. Scale bar is 500 nm in a.1 and a.2 and 200 nm in a.3. (b) Quantification of the amount of AuNR present in the cytoplasm and vesicles (endosomes and lysosomes). The percentage of AuNRs in each cell compartment was calculated after counting all the AuNRs accumulated within the cell. Results are Average ± SD (n = 30 images of amplification between 20000X and 80000X for 0 W and n = 20 images of amplification between 20000X and 80000X for 1.25 W) (c.1 and c.2) Intracellular delivery of two proteins.

To further demonstrate that NIR irradiation triggers AuNR endolysosomal escape, fibroblasts were incubated with BSA-dsDNA$_{51.7}$-AuNR in the presence of calcein, a membrane-impermeable fluorophore[289], followed by the incubation with Lysotracker (**Figure 2.11**). Cells treated with AuNRs and calcein, but without NIR laser activation, showed a punctuate distribution of fluorescence indicative of endolysosomal retention of the dye. In contrast, cells exposed to AuNRs and calcein and activated with NIR laser showed a diffuse signal (confirmed by the fluorescence profile plots) of the calcein in the cell cytoplasm and a decrease in Manders' colocalization coefficient between calcein and endolysosomal compartment. Both results indicate that calcein escaped the endolysosomal compartment. It is possible that endosomal membrane damage by radical species generated by AuNRs after NIR laser activation[142, 243, 290] favours the escape of calcein from endolysosomal compartment.

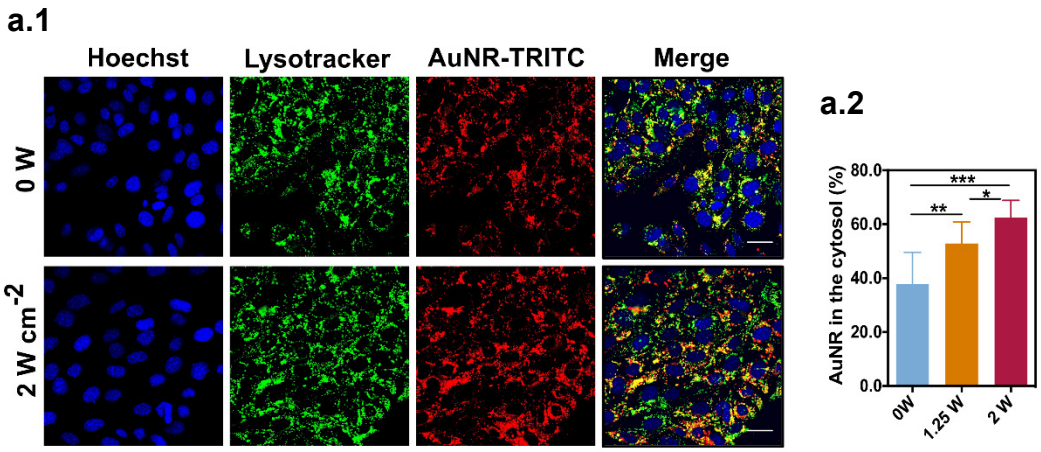


**Figure 2.10** - **Intracellular trafficking of BSA-dsDNA$_{51.7}$-AuNR-TRITC**. (a.1) Confocal images of cells stained with lysotracker green after 4 h of incubation with BSA-dsDNA$_{51.7}$-AuNR-TRITC (50 µg mL$^{-1}$) and laser irradiation (2 Wcm$^{-2}$, 2 min). Scale bar corresponds to 30 µm. (a.2) Percentage of AuNR-TRITC outside the endolysosomal compartment, determined by calculating the overlap coefficient between TRITC and lysotracker green in ImageJ. Results are Average ± SD, n=9 (3 samples, 3 microscope fields per sample). *,**, *** denote statistical significance ($p<0.01$; $p<0.001$) assessed by one-way ANOVA followed by a Tukey's post-hoc test.

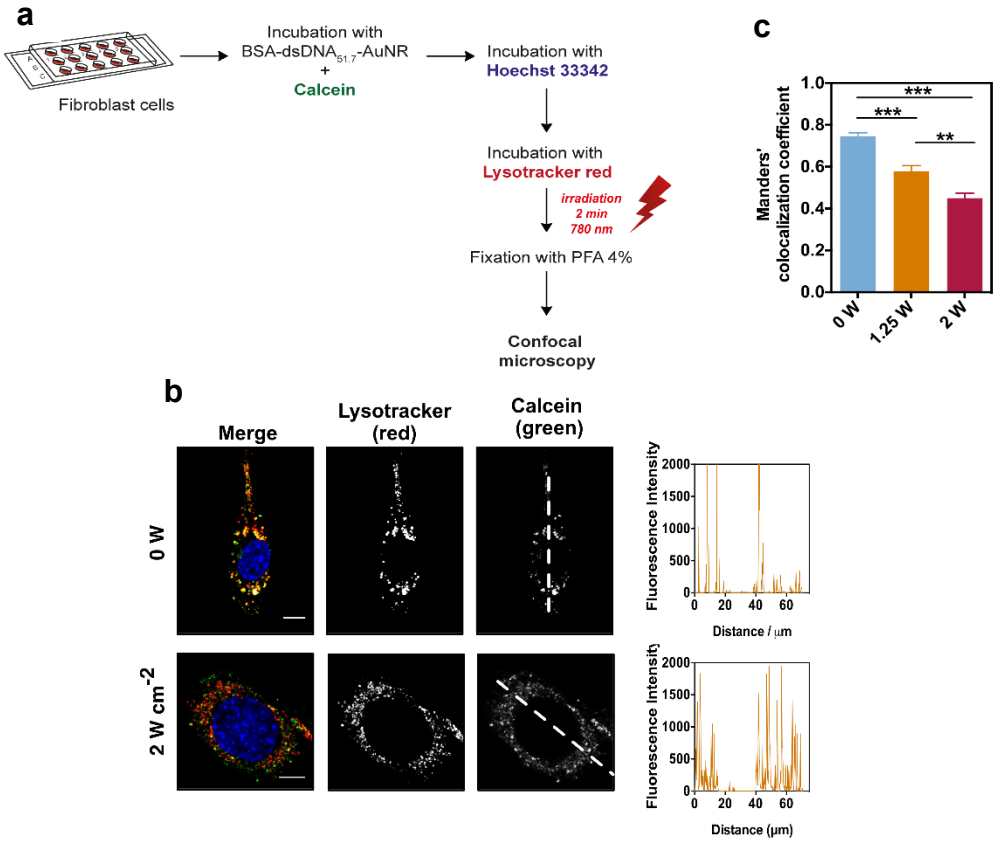


**Figure 2.11 - Effect of the NIR irradiation in the endolysomal escape of AuNRs**. Cells were incubated with BSA-dsDNA$_{51.7}$-AuNR (50 µg mL-1) and calcein (25 mM) for 4 h. After replacing the medium, cells were incubated with lysotracker red (100 nM) for 15 min and then irradiated for 2 min with a laser at 780 nm (power: 1.25 or 2 Wcm$^{-2}$). Cells were then observed in a confocal microscope. (b) Co-localization between calcein and lysotracker red in cells incubated with BSA-dsDNA$_{51.7}$-AuNR. Scale bar 10 µm. Fluorescence intensity plots were obtained from cell regions labeled with a dash. (c) Co-localization between calcein and lysotracker red expressed as Manders' overlap coefficient (calculated using ImageJ). The results are expressed as Average ± SD, n=3 (3 samples, 4 microscope fields per sample). **, *** denote statistical significance ($p<0.01$; $p<0.001$) assessed by one-way ANOVA followed by Tukey's post-hoc test.

## 2.2.5 - Intracellular release of two proteins from AuNR-protein conjugates after NIR laser activation: functional activity and temporal control of release

To investigate the intracellular delivery of two proteins within cells with temporal control, we have immobilized both DL$_{650}$-BSA-ssDNA$_{51.7}$ and DL$_{488}$-BSA-ssDNA$_{68.9}$ in AuNRs conjugated with TRITC followed by their incubation with cells for 4 h. Cells were then washed, activated with a NIR laser and fluorescence (co-localization of AuNR-TRITC with each fluorescent protein; see experimental section) monitored by a confocal microscope (**Figure 2.12 b**). The first stimulus (1.25 Wcm$^{-2}$, 2 min) induced primarily the release of DL$_{650}$-BSA-ssDNA$_{51.7}$ while the second stimulus (2 Wcm$^{-2}$, 2 min) induced primarily the release of

$DL_{488}$-BSA-$ssDNA_{68.9}$ (**Figure 2.12 c**). After the 2 stimuli the total of each protein released was lower than 50% likely due to the spatial confinement in the endolysosomal compartment and potential re-hybridization.

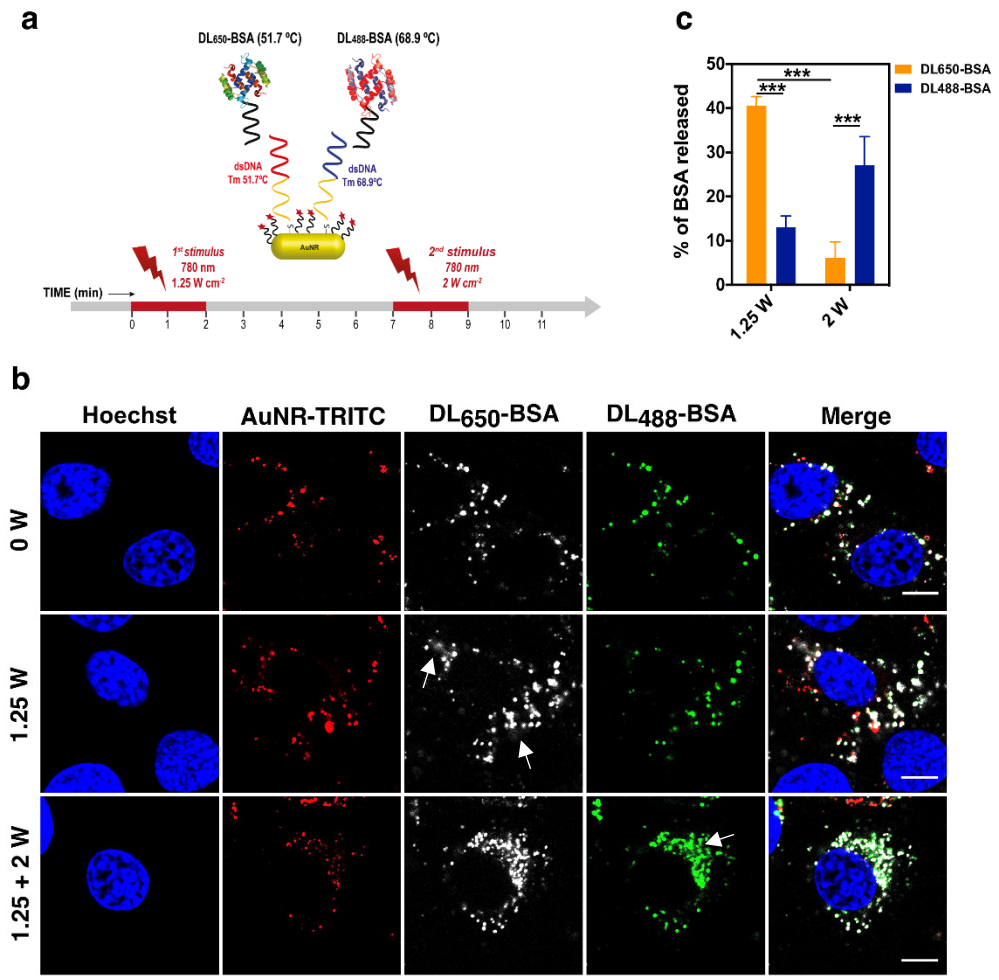


**Figure 2.12 - Sequential release of two proteins from AuNRs in cells**. a) Schematic representation of the experiment. Fibroblasts were incubated with AuNR-TRITC conjugated with $DL_{650}$-BSA-$dsDNA_{51.7}$ and $DL_{488}$-BSA-$dsDNA_{68.9}$ for 4 h. Cells were then washed with cell culture media and irradiated for 2 min at 1.25 $Wcm^{-2}$. A subset of samples was fixed with 4% PFA after irradiation and the other group was incubated for additional 5 min before being irradiated for 2 min at 2 $Wcm^{-2}$ and fixed afterwards. b) High magnification confocal images of fibroblasts subjected to different laser stimuli. White arrows indicate areas where the signal is more diffuse and does not colocalize with AuNR-TRITC c) The amount of protein released was calculated as %BSAR= 100 x (MCbefore - MCafter)/MCbefore, where MCbefore is the Manders' colocalization coefficient before irradiation and MCafter is the Manders' colocalization coefficient after irradiation. Results are Average ± SEM, n=3 (3 samples, 5 microscope fields per sample). Images for colocalization analysis were obtained with 40x objective. Unpaired t-test was used to compare each condition (p value ≤ 0.0001).

To show the capacity of AuNRs to deliver a functional protein to cells, we used β-Gal as a model enzyme. Fibroblasts were incubated with β-Gal-dsDNA$_{51.7}$-AuNR for 4 h, washed, and then activated by a NIR laser with variable power. The activity of β-Gal was immediately measured by confocal microscopy using a fluorescent substrate[291] (**Figure 2.13 a.1**). Irradiated cells showed a higher fluorescence and thus a higher intracellular enzyme activity (**Figure 2.13 a.2**). We attributed the increase of enzyme activity to a change in the intracellular localization of the enzyme. With laser irradiation, it is expected that most of enzyme and AuNR escape the endolysosomal compartment (see before) to the cytosol. The pH conditions (pH ≈ 7.2[292]) in the cytosol favours an increase in enzyme activity as compared to the pH conditions in the endolysomal compartment (pH between 6.3 and 5.5 [292]) (**Figure 2.13 b**). The possible effect of laser irradiation on alteration of cell fluorescence was tested with AuNRs modified with denatured β-Gal (**Figure 2.13 a.4**). Moreover, irradiated cells showed a lower co-localization between the enzyme and the AuNR by immunofluorescence (**Figure 2.14**) suggesting the release of the enzyme from the AuNR. Next, we evaluated the possibility of controlling the release of the protein from AuNRs accumulated within the cell for at least one day. Therefore, cells were incubated with β-Gal-dsDNA$_{51.7}$-AuNR for 4 h, cultured for additional 24 h and finally activated by a NIR laser (1.25 Wcm$^{-2}$, 2 min). Irradiated cells showed a higher fluorescence, and thus a higher intracellular enzyme activity, than non-irradiated cells (**Figure 2.13 a.3**). This indicates that protein carriers may accumulate within cells for at least 1 day without decreasing significantly the enzyme activity. It is likely that β-Gal benefits from a protective environment against proteolytic degradation while immobilized on the AuNRs.

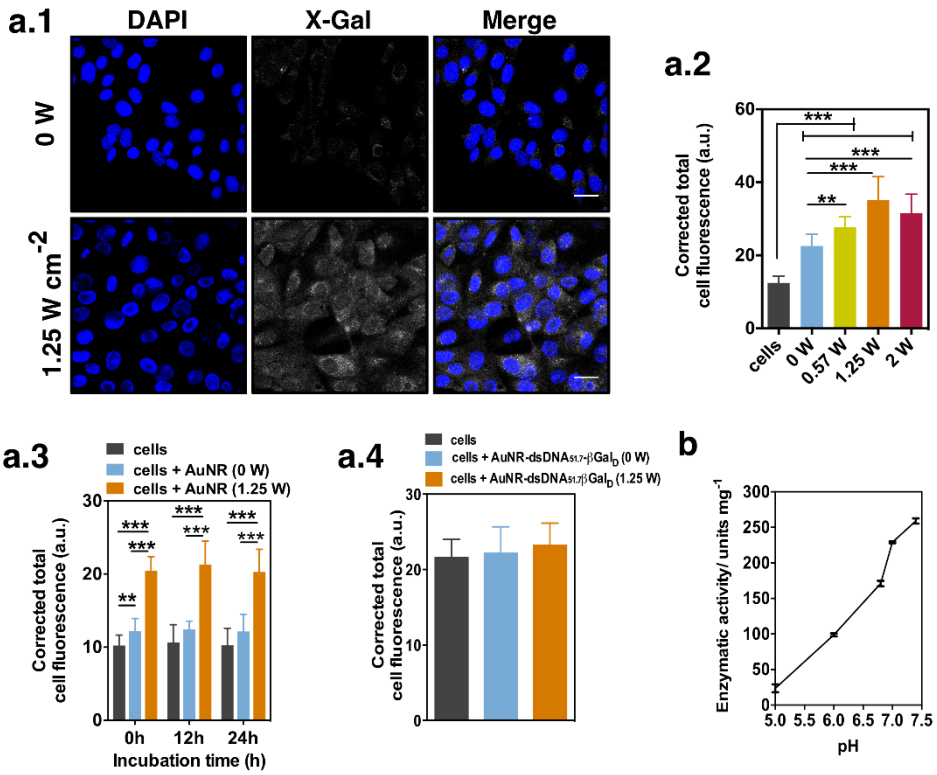


**Figure 2.13 - Intracellular activity of a protein released from AuNR-dsDNA$_{51.7}$-βGal**. Fibroblasts were incubated with AuNR-dsDNA$_{51.7}$-βGal (50 μg mL$^{-1}$) for 4 h, after which were washed, new culture media was added, and then were irradiated for 2 min (wavelength: 780 nm; laser powers: 0.57, 1.25 and 2 Wcm$^{-2}$). Then, cells were immediately fixed and exposed to a β-Gal substrate (X-Gal) followed by confocal microscopy evaluation. (a.1) Representative confocal microscopy images. Scale bar is 30 μm. (a.2) Quantification of β-Gal activity. Cell fluorescence was corrected to the corresponding background fluorescence and thus named as corrected total cell fluorescence. The group "cells" means cells without AuNRs. (a.3) Quantification β-Gal activity. After 4 h incubation, medium was replaced and cells were irradiated immediately (0 h), 12 h or 24 h after. a.4) Enzymatic activity quantified after 4 h of incubation with AuNRs conjugated with denatured β-Gal (AuNR-dsDNA$_{51.7}$-βGalD) (50 μg mL$^{-1}$) followed by irradiation for 2 min at 1.25 Wcm$^{-2}$. (b) Enzymatic activity of β-Gal at different pHs. β-Gal (50 μL, 0.4 μg mL$^{-1}$) prepared in 0.1 M phosphate buffer (pH 5.0, 6.0, 6.8, 7.0 and 7.4) was added to ONPG (100 μL, 13 mg mL-1) also prepared in 0.1 M phosphate buffer (pH 5.0, 6.0, 6.8, 7.0 and 7.4). The absorbance at 420 nm was measured for 30 min at 37 ºC in a 96 well plate using a Synergy HT microplate reader. One unit corresponds to the hydrolysis of 1 μmol of substrate (ONPG) per minute per mg of enzyme powder. In a.2 and a.3, results are expressed as Average ± SD, n=3 (3 samples, 5 microscope fields per sample). **, *** denote statistical significance ($p<0.01$; $p<0.001$) assessed by one-way ANOVA followed by a Tukey's post-hoc test.

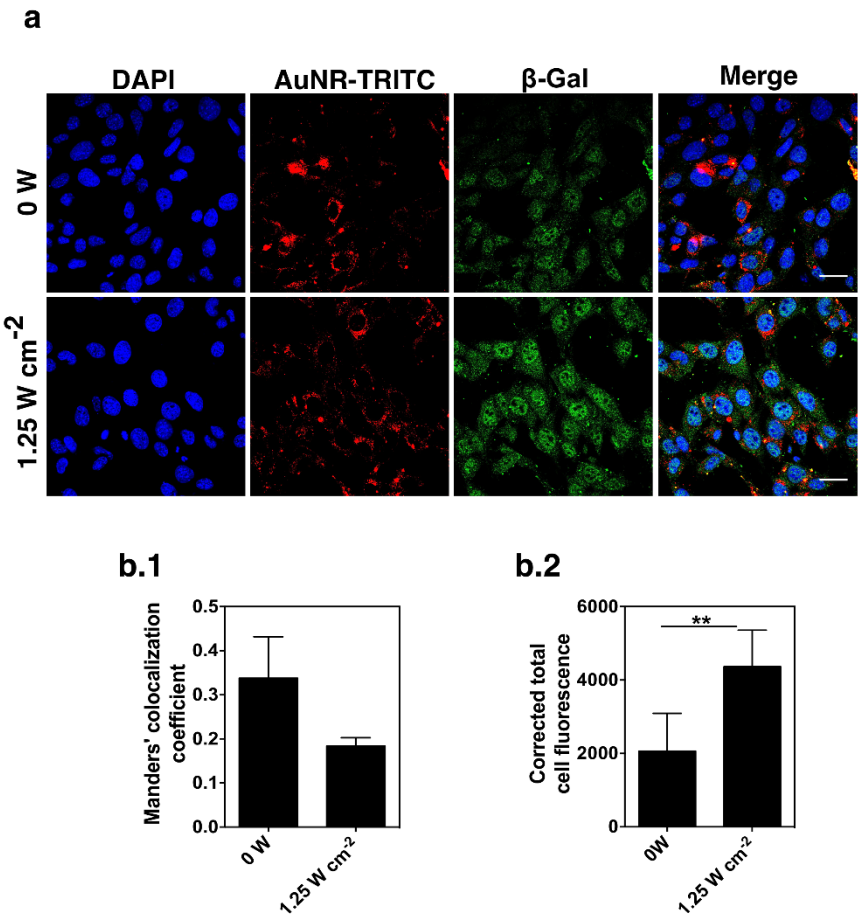


**Figure 2.14**. **Intracellular levels of β-Gal assessed by immunocytochemistry**. (a) Confocal images of fibroblasts incubated with βGal-dsDNA$_{51.7}$-AuNR-TRITC. Cells were incubated for 4 h with βGaldsDNA$_{51.7}$-AuNR-TRITC (50 μg mL$^{-1}$), washed to remove the non-internalized AuNRs and irradiated for 2 min with a 780 nm laser (power: 1.25 Wcm$^{-2}$). Cells were fixed immediately after laser treatment (0 min) using a β-Gal antibody. Scale bar is 30 μm. (b.1) The co-localization between AuNR-TRITC and β-Gal was determined using ImageJ and is expressed as Manders' co-localization coefficient. After irradiation, and immediate (time 0 min) evaluation of the co-localization between β-Gal and AuNR-TRITC, our results show a decrease in the co-localization of both entities, which indicates the release of the protein from the AuNR. (b.2) Cell fluorescence in each experimental condition was corrected to the corresponding background fluorescence and thus designed as corrected total cell fluorescence. Results are Average ± SD, n=9 (3 samples, 3 microscope fields per sample). ** denotes statistical significance ($p<0.01$) assessed by an unpaired t-test.

## 2.3 - Discussion

The current work reports a NIR light-activatable nanomaterial for the intracellular release of more than one protein, with independent release profiles. The novelty of the present work relies in the (i) development of an approach for the intracellular delivery of more than one active protein using NIR as a trigger, (ii) the demonstration that NIR light activates the release of the protein from the plasmonic carrier and the endolysosomal escape of both carrier and protein, and (iii) the demonstration of protein release from a carrier that has been accumulated within the cell between 4 h and at least 1 day (temporal control). The system documented here is based on the hybridization of a protein-modified with a single strand DNA (with a specific melting temperature) to a complementary single strand DNA immobilized on the surface of the AuNR. Upon NIR illumination at 780 nm, a photothermal effect occurs, leading to the melting of the double strand DNA and consequent release of the protein. We have demonstrated this principle for the controlled release of two proteins from the same carrier using a single NIR laser wavelength. Previous studies have demonstrated the release of siRNA and small oligonucleotides from AuNRs[91, 103, 139]; however, it was unclear whether the same principle could be extended to proteins that are very sensitive to temperature. Our results show that the selection of specific single strand DNAs (and thus melting temperature range) as well as spacer lengths between the oligonucleotide and the thiol group for AuNR, leads to the development of a system that is responsive to NIR light and has minimal[122] impact in the activity of the protein after release.

Although the release of proteins from light-triggerable nanoformulations [122, 125] has been documented, this is the first reported demonstrating the sequential release of more than one protein. In one study[122], the authors have conjugated a model protein (green fluorescent protein) with a histidine tag to a linker containing in one terminal a nickel chelator and in the other terminal a thiol group for the conjugation to a hollow gold nanoshell. The release of the protein was demonstrated after exposure to a NIR pulsed laser that melted the gold-thiol bonds. The authors have demonstrated the intracellular release of the protein but not its intracellular activity. Moreover, the formulation reported was not permissive to the release of more than one protein with an independent release profile. Another study described the intracellular delivery of a functional enzyme using upconversion nanoparticles (UNPs) conjugated with a spiropyran (SP), a photoisomerizable compound[125]. After immobilization, SP was irradiated with UV light to convert it into merocyanine (MC) form, which is positively charged at neutral pH and could be used to immobilize β-Gal through electrostatic interactions. NIR irradiation leads to the emission of visible light by UNPs, converting MC form to SP and decreasing the electrostatic interaction with the protein, releasing β-Gal in its active form. Although the authors have demonstrated the intracellular

delivery of proteins, the formulations reported were not permissive to the release of more than one protein with an independent release profile in any of the cases.

In conclusion, we have developed a new approach for the intracellular delivery of multiple proteins. The intracellular delivery of proteins has been demonstrated by microscopy localization studies, FRET acceptor photobleaching studies and enzyme intracellular activity measurements. Our results show that the NIR laser triggers the release of the protein from the AuNR and the escape of both AuNRs and protein from the endolysosomal compartment. Overall, the current work opens new possibilities for the design of materials to control the release of proteins, which may have implications in the areas of cellular reprogramming, cell modulation and gene editing.

## 2.4 - Materials and Methods

**Materials.** β-Galactosidase (β-Gal) from *Escherichia coli*, thiolated oligonucleotide strands, hexadecyltrimethylammonium bromide (CTAB), sodium borohydride ($NaBH_4$), silver nitrate ($AgNO_3$), hexanethiol and mercaptohexanoic acid, and other chemicals were all purchased from Sigma-Aldrich and used as received without further purification. Sodium dodecyl sulfate (SDS) was purchased from VWR. Bovine Serum Albumin (BSA), DyLight-NHS ester, N-[γ-maleimidobutyryloxy] sulfosuccinimide ester (sulfo-GMBS), LysoTracker® Green DND-26, LysoTracker® Red DND-99, fetal bovine serum (FBS) and trypsin-EDTA solution were purchased from Thermo Fisher Scientific. Dulbecco's Modified Essential Medium (DMEM) is a commercial product of Merck Millipore. Purified water with resistivity above 18.2 $M\Omega.cm^{-1}$ was obtained by reverse osmosis (MilliQ, Millipore). Other reagents were analytical grade.

**AuNR synthesis**. AuNRs were prepared using the seed mediated method.[155] For the preparation of the seed solution, gold(III) chloride hydrate ($HAuCl_4$, 0.1 M, 12.5 µL) was added to a hexadecyltrimethylammonium bromide (CTAB) solution (0.1 M, 5 mL) and stirred vigorously for 5 min, after which an ice-cold sodium borohydride solution ($NaBH_4$, 10 mM, 0.3 mL) was added. After stirring for 2 min the solution was kept at 25 ºC. For the preparation of growth solution, silver nitrate ($AgNO_3$, 5 mM, 3.2 mL) was added to CTAB solution (0.1 M, 200 mL) and mixed gently, after which $HAuCl_4$ (50 mM, 2 mL) was added. After mixing, ascorbic acid (0.1 M; 1.5 mL) was added. The solution changed from dark yellow to colourless. Finally, 1.5 mL of the seed solution (aged for 8 min at 25 ºC) was added to the growth solution. The solution was kept at 28 ºC for 2 h. The NRs were washed by centrifugation at 9000 g and resuspended in water.

The CTAB on the AuNR surface was replaced using a method already reported with some modifications.[191] Hexanethiol (1.5 mL) was added to the NR-CTAB suspension (2.5 nM; 1 mL). Then, acetone (3 mL) was added and the mixture was swirled for a few seconds. The aqueous phase became clear indicating ligand exchange and the organic phase containing the AuNRs was extracted. Then, a mixture of toluene (2 mL) and methanol (5 mL) was added to the organic phase. The solution was centrifuged at 5000 g, 10 min, and the pellet was resuspended in 0.5 mL of toluene by brief sonication. The organic to aqueous phase was performed as follows. AuNR-hexanethiol (1 mL) in toluene was added to 9 mL of mercaptohexanoic acid (MHA, 5 mM, 9 mL) in toluene at 95 ºC. The reaction proceeded under reflux with magnetic stirring for 15 min. The precipitation of AuNRs indicated successful coating by MHA. After cooling to room temperature, the aggregates were washed twice with toluene by decantation. Finally, the NRs were washed with isopropanol to

deprotonate the carboxylic groups and then the aggregates were redispersed in 1× TBE. The ligand exchange was confirmed by zeta potential measurements.

**Functionalization of NR-MHA with single strand DNA (ssDNA)**. Thiolated ssDNA (sequence A 5'-HS-C6-TTTTTTTTTTTTTTTATAACTTCGTATA-3' or sequence B 5'- HS-C6-TTTTTTTTTTTGTCCGGGTCCAGGGC-3', purchased from Sigma-Aldrich) were reduced for 1 h with 100-fold excess of Tris(2-carboxyethyl)phosphine (TCEP) over ssDNA. The NR suspension (0.5 nM; 0.5 mL) was incubated with the thiolated ssDNA for 3 h in a molar ratio of 1:400 in 10 mM phosphate buffer pH 7.4 containing 0.3% (w/v) of sodium dodecyl sulfate (SDS). Afterwards, a NaCl solution (22.5 µL; 0.45 M) was added every 60 min to the AuNR suspension. This operation was repeated four times and the suspension shaked overnight to improve the reaction yield. In the following day, the NR suspension was centrifuged at 9000 g, the supernatant was collected and the pellet was resuspended in 10 mM phosphate buffer with 30 mM NaCl. The amount of oligonucleotides was determined by measuring absorbance at 260 nm in the supernatant. The ssDNA-AuNRs obtained were stored at 4 ºC before use (not more than one week).

**Table 2.1 – DNA sequences used for AuNR modification and conjugation with proteins**

| | Tm / ºC | sequence |
|---|---|---|
| **AuNR conjugation** | 51.7 | 5'-HS-C6-TTTTTTTTTTTTTTTATAACTTCGTATA-3' |
| | 68.9 | 5'-HS-C6-TTTTTTTTTTTTGTCCGGGTCCAGGGC-3' |
| **DNA-protein conjugates** | 51.7 | 5'-HS-C6-TATACGAAGTTATAAAAAAAAAA-3' |
| | 68.9 | 5'-HS-C6-TGCCCTGGACCCGGAC-3' |

**Labelling of BSA with a fluorescent dye**. BSA was labelled with DyLight-NHS ester (Thermo Fisher Scientific). For this purpose, a solution of BSA (2 mg $mL^{-1}$, 4.8 nmol, in PBS) was mixed with DyLight 488 NHS ester (50 µg, 49.4 nmol) or DyLight 550 NHS ester (50 µg, 48.07 nmol) or DyLight 650 NHS ester (50 µg, 46.9 nmol) and kept under orbital shaking for 2 h. After reaction, the solution was dialyzed against PBS in a dialysis cassette (MWCO 10 kDa) for 48 h at 4 ºC. The final protein concentration and degree of labelling were determined by measuring the absorbance in Nanodrop at 280 nm (A280) and at the DyLight absorbance maximum (Amax; Amax = 493 nm for DyLight 488; 562 nm for DyLight 550 and 652 nm for DyLight 650). The protein concentration was calculated according to the following equation: $protein\ concentration\ (M) = (A280 - (Amax \times CF))/\varepsilon$, where CF is the correction factor (0.147 for DyLight488, 0.0806 for DyLight550 and 0.0371 for DyLight 650) and ε is the molar

extinction coefficient of BSA. The number of fluorophores per BSA was calculated from $Amax/(\varepsilon' \times protein\ concentration)$ where ε' is the molar extinction coefficient of the dye (70000 $M^{-1}$ $cm^{-1}$ for DyLight 488; 150000 $M^{-1}$ $cm^{-1}$ for DyLight 550 and 250000 $M^{-1}$ $cm^{-1}$ for DyLight 650). After purification each protein had in average 5 fluorophores.

**Preparation of protein conjugated with ssDNA**. Protein-ssDNA conjugates were prepared using N-[γ-maleimidobutyryloxy]sulfosuccinimide ester (sulfo-GMBS, Thermo Scientific) as linker. Briefly, a solution of protein (BSA-DyLight at 7.5 μM or β-Gal at 3.5 μM in PBS pH 7.4) was reacted with sulfo-GMBS in a 20-fold molar ratio for 30 min at room temperature. The excess of linker was removed by ultrafiltration with Nanosep 30 kDa (Pall Corporation) and the purified protein (7.5 μM; 1.12 nmol in PBS) was reacted with thiolated DNA (22.5 μM; 3.36 nmol in PBS) in a final volume of 150 μL of PBS for 2 h at room temperature. DNA strands were complementary to the strands immobilized on the NR surface (complementary sequence A: 5'-HS-C6-TATACGAAGTTATAAAAAAAAAA; complementary sequence B: 5'-HS-C6-TGCCCTGGACCCGGAC). BSA-ssDNA and β-Gal conjugates were purified by size exclusion HPLC using a Shimadzu-LC-20AD system. β-Gal-ssDNA was purified with a superdex 200 5/150GL column (GE Healthcare) and BSA-ssDNA was purified with a BIOBASIC SEC-300 300 x 7.8mm, 5 μm particle size (Thermo Scientific). PBS was used as eluent at a flow rate of 0.3 mL $min^{-1}$.

**Characterization of protein conjugated with ssDNA by non-denaturing PAGE.** The reaction mixture obtained after reacting the proteins with ssDNA and the fractions obtained after HPLC purification of the reaction mixture were analysed by gel electrophoresis. Reaction mixture (15 μL) and reaction mixture fractions obtained after HPLC purification (15 μL) were mixed with glycerol (5 μL; glycerol in 50% v/v of $H_2O$), loaded in a polyacrylamide gel (12%, w/v) and run for 45 min in 0.5 x TBE at 140 V. The gel was stained with SyBr Gold (1:5000 in 1 x TBE) for 10 min and imaged in a UV transilluminator (Molecular Imager Gel DOC, Biorad).

**Labelling of NR-ssDNA with TRITC.** Thiol-PEG-amine 1 kDa (Creative PEGworks, 20 nmol) was reacted with TRITC (20 nmol) in 1 mL of 10 mM carbonate buffer at pH 9.0 for 2 h at room temperature. Then 500 μL of NR-ssDNA (0.5 nM) were incubated overnight with thiol-PEG-TRITC in a molar ratio of 1:1000. The excess of fluorophore was removed in two steps of centrifugation at 9000 g. The supernatants were then quantified for the presence of TRITC by fluorescence spectroscopy. According to our calculations, we have 540 PEG-TRITC chains immobilized per AuNR. Therefore, the stoichiometry between ssDNA and TRITC in the AuNRs is 1:4.5.

**Immobilization of protein-ssDNA conjugates in AuNRs**. For the hybridization of complementary oligonucleotide strands conjugated with a protein, a suspension of AuNR-ssDNA (0.5 nM) was incubated with DNA-protein conjugates (150 nM) for 1 h at 37 ºC and then the temperature was slowly decreased to 25 ºC. The excess of DNA-protein conjugate was removed by centrifugation. The amount of DyLight-BSA (DL-BSA) immobilized on the AuNRs was determined indirectly by measuring the fluorescence in the supernatant. The amount of β-Gal immobilized was determined by measuring the enzymatic activity in the supernatant. Briefly, 50 µL of supernatant or NR suspension were added to 100 µL of o-nitrophenyl β-d-galactopyranoside (ONPG, 13 mg $mL^{-1}$ in 0.1 M phosphate buffer pH 7.0) and incubated at 37 ºC for 30 min in a Synergy HT microplate reader. The absorbance at 420 nm was measured every 3 min.

**Light-induced release proteins from AuNRs**. A suspension of DL-BSA-dsDNA-AuNR (20 µg $mL^{-1}$ in 10 mM phosphate buffer supplemented with 30 mM of NaCl, pH 7.4) was placed in a 96 well plate and irradiated with a fibercoupled Roithner laser (continuous wave at 780 nm) with different laser powers (0.8, 1.25 or 2 $Wcm^{-2}$) placed at 10 cm from the sample. The power of the laser beam in the sample was measured using a thermal power sensor from Thorlabs. After irradiation, the suspension was immediately centrifuged at 9000 g. The fluorescence of the supernatant was measured in order to determine the amount of protein released.

To test the multiple release system, AuNRs conjugated with $DL_{488}$-BSA and $DL_{550}$-BSA were first irradiated for 2 min at 1.25 $Wcm^{-2}$. The supernatant was collected and after resuspending the pellet, the suspension was irradiated for further 3.5 min at 2 $Wcm^{-2}$.

The light induced release of β-galactosidase conjugated to AuNRs (20 µg $mL^{-1}$ in 10 mM phosphate buffer supplemented with 30 mM of NaCl, pH 7.4) was also studied. For that purpose, after 2 min of irradiation at 0.57, 1.25 or 2 $Wcm^{-2}$, the supernatant was collected, the pellet was resuspended and the enzymatic activity of the supernatant and the suspension was measured using ONPG as substrate. For that purpose, 50 µL of supernatant or β-Gal-dsDNA-AuNR suspension were added to 100 µL of o-nitrophenyl β-d-galactopyranoside (ONPG, 13 mg $mL^{-1}$ in 0.1 M phosphate buffer pH 7.0) and incubated at 37 ºC for 30 min in a Synergy HT microplate reader. The absorbance at 420 nm was measured every 3 min. The reaction rate was calculated in the linear region of the curve (less than 10% of substrate conversion).

**Cell culture.** SC-1 mouse fibroblasts were kindly offered by Dr. Carol Stocking. Cells were cultured in 60 mm culture dishes at 37 ºC in a humidified atmosphere of 5% $CO_2$ in DMEM cell culture media containing 10% fetal bovine serum (FBS) and 0.5% penicillin-

streptomycin. Passages 5-25 were used for the experiments; cells were typically grown to 80-90% confluency before splitting and re-seeding 24 h before the experiment.

**Uptake kinetics of βGal-dsDNA-AuNR.** SC-1 cells were plated in a 24 well plate at a density of $5x10^4$ cells/well and left to adhere overnight. The cells were incubated with βGal-dsDNA-AuNR (50 μg $mL^{-1}$) for 1, 2, 4, 6 and 24 h. After incubation, in order to remove non-internalized nanorods, the cells were washed three times with PBS, dissociated with trypsin and counted. Finally, the samples were freeze-dried and the amount of gold was determined by inductive coupled plasma mass spectrometry (ICP-MS). In order to evaluate the levels of internalized AuNRs along the time, cells were incubated with βGal-dsDNA-AuNR for 4 h and after washing three times with PBS, cells were left in the incubator for 3, 6, 12 or 24 h. In a subset of samples, after incubation with βGal-dsDNA-AuNR, cells were treated with Mitomycin C (8 μg $mL^{-1}$, Sigma) for 2h30, to inhibit cell proliferation.

**Cytotoxicity of BSA-dsDNA-AuNR**. To assess the cytotoxicity of AuNRs, SC-1 fibroblasts were seeded on a 96 well plate (4 x $10^3$ cells/well), left to adhere for 24 h and then incubated with BSA-dsDNA$_{51.7}$-AuNR (concentrations between 10 and 200 μg $mL^{-1}$) for 4 h. After incubation, cells were washed with medium to remove non-internalized AuNRs. In some conditions, after incubation with BSA-dsDNA-AuNR, cells were washed and irradiated with a fibercoupled Roithner laser (780 nm). Each well was placed below the end of the fibre and irradiated with a power density of 1.25 or 2 $Wcm^{-2}$ for 2 min. Then cells were left in the incubator for 24 h and the ATP production was measured by a Celltiter-Glo Luminescent Cell Viability Assay (Promega).

In a separate experiment, the cytotoxicity of AuNRs was evaluated by an Annexin/PI assay. Cells were seeded in a 48 well plate (20000 cells/well), left to adhere for 24 h and incubated with BSA-dsDNA$_{51.7}$-AuNR at 20, 50 and 100 μg $mL^{-1}$, for 4 h. After washing to remove non-internalized AuNRs, cells were irradiated at 1.25 or 2 $Wcm^{-2}$ for 2 min. After 24 h incubation at 37 ºC, the medium containing detached cells was collected and the adherent cells were rinsed with PBS and trypsinized. After centrifuging, the pellet was resuspended in 100 μL of binding buffer containing 2.5 μL of Annexin V-FITC conjugate (Invitrogen). After 15 min incubation, 100 μL of propidium iodide (2 μg $mL^{-1}$) were added to each tube and then the cells were kept on ice until analysis by flow cytometry.

**Confocal microscopy.** Images were acquired on a Zeiss LSM 710 confocal microscope (Carl Zeiss, Jena, Germany) using a 40x objective/ 1.4 numerical aperture oil PlanApochromat immersion lens. $DL_{488}$ and Lysotraker Green fluorescence was detected using the 488 nm laser line of an Ar laser (25 mW nominal output) and an LP 505 filter.

TRITC and Lysotracker Red fluorescence was detected using a 561 nm HeNe laser (1 mW) and an LP 560 filter. $DL_{650}$ and XGal fluorescence was detected using a 633 nm HeNe laser. The pinhole aperture was set to 1 Airy unit. Live cells were imaged at 37 °C and 5% $CO_2$. Image acquisition and analyses were performed using the Zen Black 2012 software.

Fluorescence resonance energy transfer (FRET) was measured by the acceptor photobleaching method [293]. Images were acquired before and after photobleaching TRITC. TRITC was photobleached using the 561 nm laser line with 80% intensity. FRET efficiency was calculated as $FRET_{eff} = [(_{Dafter})-D_{before})]/D_{after}$ x 100 where $D_{after}$ is the fluorescence intensity of the donor ($DL_{488}$) after acceptor photobleaching, and $D_{before}$ the fuorescence intensity of the donor before acceptor photobleaching. Corrected total cell fluorescence was determined by the subtracting the background fluorescence to the cell fluorescence. The coefficient of variation (CV) of the fluorescence signal was calculated as CV = σ/μ where σ is the standard deviation and μ is the mean. Manders' colocalization coefficient is a measure of pixel overlap, independent of pixel intensities. The value of the coefficient is 1 if all the pixels with fluorescence in the channel (ex. red) overlap with pixels in the other channel (ex. green). A value of zero means that the signal in both channels is mutually exclusive. [294]

**Light-induced release of fluorescent BSA in cells**. SC-1 cells were seeded in an IBIDI 15 well slide (5000 cells/well), left to adhere for 24 h and then incubated with 50 μg $mL^{-1}$ of AuNR-TRITC conjugated with one fluorescent protein ($DL_{488}$-BSA Tm 68.9 ºC) or two fluorescent proteins ($DL_{650}$-BSA Tm 51 ºC; $DL_{488}$-BSA Tm 68.9 ºC). After 4 h incubation, the medium was replaced and cells were irradiated with a fibercoupled laser (780 nm) at 1.25 or 2 $Wcm^{-2}$ for 2 min. Then, the cells were fixed for 15 min with 4% (v/v) paraformaldehyde and washed three times with PBS. The nucleus was stained with DAPI (1μg $mL^{-1}$) for 5 min. The release of proteins was studied using the Manders' colocalization coefficient between the fluorescent protein and the AuNR-TRITC.

For the dual release experiment, cells were exposed for 4 h to the nanomaterials, washed and then irradiated at 1.25 $Wcm^{-2}$ for 2 min. A group of samples was immediately fixed and the other group was incubated for 5 min at 37 ºC until second irradiation at 2 $Wcm^{-2}$ for 2 min. Then, the cells were fixed for 15 min with paraformaldehyde 4% (v/v) and washed three times with PBS. The nucleus was stained with DAPI (1μg $mL^{-1}$) for 5 min. The percentage of release of each protein after each stimulus (1.25 $Wcm^{-2}$ or 2 $Wcm^{-2}$) was inferred from the colocalization between each fluorescent protein and AuNR-TRITC using the following equation: % release = 100 x (MCbefore – MCafter)/MCbefore, where MCbefore is the Manders' colocalization coefficient before each laser stimulus (1.25 $Wcm^{-2}$ or 2 $Wcm^{-2}$) and MCafter is the Manders' colocalization coefficient after the stimulus.

**Light-induced release of β-galactosidase in cells. Enzymatic assay.** For the transfection studies with βGal-dsDNA$_{51.7}$-AuNR, cells were grown in a 15 well IBIDI slide at an initial density of 5000 cells/well for 24 h. After 4 h incubation with βGal-dsDNA$_{51.7}$-AuNR (50 μg mL$^{-1}$), medium was replaced and the cells were irradiated with different laser power densities (0.57, 1.25 and 2 Wcm$^{-2}$) for 2 min. After irradiation cells were fixed and the activity of β-Gal was determined with a Senescence Detection Kit (Abcam) following the manufacturer's protocol. After overnight incubation with XGal substrate, cells were observed under confocal microscope. To test the intracellular stability of the released enzyme after laser activation (1.25 Wcm$^{-2}$ for 2 min), cells were incubated up to 60 min at 37 ºC until β-Gal activity measurement. To test the stability of internalized AuNRs, after 4 h incubation with βGal-dsDNA$_{51.7}$-AuNR, cells were rinsed with PBS and incubated for 12 h or 24 h before laser irradiation (1.25 Wcm$^{-2}$ for 2 min). Immediately after irradiation, cells were fixed and the enzymatic activity was determined as described before.

**Immunocytochemistry**. Cells were seeded in gelatin coated coverslips and left to adhere for 24 h. After 4 h incubation with βGal-dsDNA-AuNR (50 μg mL$^{-1}$), cells were irradiated with 780 nm laser at 1.25 Wcm$^{-2}$. The samples were immediately fixed after irradiation with paraformaldehyde 4% (v/v) for 15 min at room temperature followed by the washing (3 times) with PBS. After blocking (PBS solution with 1% BSA), cells were incubated with a rabbit anti-β-galactosidase antibody (Invitrogen) for 60 min, washed three times with blocking buffer and incubated with alexa-fluor488 conjugated goat anti-rabbit IgG (dilution 1:1000) for 60 min. The excess of antibody was removed by washing with PBS before staining with DAPI (1 μg mL$^{-1}$) for 5 min. Coverslips were analysed in a confocal microscope (LSM 710, Carl Zeiss). The corrected total cell fluorescence was quantified with ImageJ and corrected for background fluorescence. Manders' colocalization coefficient was calculated using Image J and JACoP plugin.

**Intracellular localization of AuNR-TRITC.** Cells were seeded in an IBIDI 15 well slide (5000 cells/well), left to adhere for 24 h and then incubated with BSA-dsDNA-AuNR-TRITC (50 μg mL$^{-1}$) for 4 h. After incubation, cells were washed with medium to remove non-internalized AuNRs. Then, the cells were incubated with LysoTracker® Green (100 nM) for 30 min to stain the endosomes and with Hoechst 33342 (1μg mL$^{-1}$) to stain the nuclei. Cells were observed under confocal microscope, immediately after laser irradiation at 780 nm (1.25 and 2 Wcm$^{-2}$). The images were analysed in ImageJ and the colocalization was determined by calculating the Manders' colocalization coefficient between AuNR-TRITC and Lysotracker green.

**Light-induced endosomal escape.** To study endosomal escape, cells were incubated with BSA-dsDNA-AuNR in the presence of a membrane impermeable molecule, calcein. Briefly, 5000 cells/well in a IBIDI slide were incubated with 50 μg $mL^{-1}$ of BSA-dsDNA-AuNR and 0.25 mM calcein for 4 h. After removing AuNRs, cells were incubated with lysotracker red (100 nM) for 30 min. Then, medium was replaced and cells were irradiated with 780 nm laser for 2 min (1.25 and 2 $Wcm^{-2}$) and analysed under confocal microscope.

**Transmission electron microscopy (TEM).** TEM was used to evaluate endosomal escape of AuNRs. Cells were seeded in a petri dish (60 mm of diameter), left to adhere for 24 h to 90% of confluency and then incubated with $DL_{488}$-BSA-$dsDNA_{68.9}$-AuNR (50 μg $mL^{-1}$). After 4 h incubation, the medium was replaced and cells were irradiated with a fibercoupled Roithner laser (780 nm) at 2 $Wcm^{-2}$ for 2 min. The culture medium was then removed without allowing the cells to dry. The cells were washed with PBS and 3 mL of fixative (2.5% (v/v) glutaraldehyde in 0.1 M phosphate buffer pH 7.4) was added at room temperature for 45 min by gently shaking. Then the fixative was changed for 0.8 mL of fresh fixative at 4 ºC, the cells were scraped and the suspension was transferred to an Eppendorf. The suspension was centrifuged at 3000 rpm for 4 min at 4 ºC in order to obtain a pellet and 500 μL of fixative were added and left to rest for 15 min at 4 ºC. The fixative was changed by 0.1 M phosphate buffer and the pellet was resuspended. Afterwards the cells were centrifuged at 3000 rpm for 4 min at 4 ºC. The last two steeps were repeated three times in order to completely eliminate the fixative. The samples were then post-fixed with 1% OsO4 0.8% $C_6N_6FeK_4$ in 0.1 M PBS for 2 h at room temperature, washed with PBS 0.1 M, and finally dehydrated (in a graded concentration of acetone). The dehydrated samples were then embedded in resin and sliced in blocs for visualization. TEM images were recorded with a Tecnai Spirit microscope (EM) (FEI, Eindhoven, The Netherlands) equipped with a LaB6 cathode. Images were acquired at 120 kV and room temperature with a 1376 x 1024 pixel CCD camera (FEI, Eindhoven, The Netherlands). Images were acquired with a magnification between 20000X and 80000X. In each image, the number of AuNRs in cell compartments (endosomes, lysosomes and cytosol) was counted and divided by the total number of AuNRs per image to obtain percentage of AuNRs per compartment.

**Statistical analysis.** An unpaired t-test or one-way ANOVA analysis of variance with Tukey´s post-test was performed for statistical tests using GraphPad Prism software (San Diego, CA, USA, http://www.graphpad.com/). Results were considered significant when $P<0.05$.

# Chapter 3

# Modulation of angiogenic activity by light-activatable nanocarriers carrying miRNAs

# Modulation of angiogenic activity by light-activatable nanocarriers carrying miRNAs

Miguel M. Lino, Susana Simões, Andreia Vilaça and Lino Ferreira*

CNC, Center for Neurosciences and Cell Biology and Faculty of Medicine, Polo III - Health Sciences Campus University of Coimbra, Rua Larga, 3004-517, Coimbra, Portugal

## Abstract

The combinatorial delivery of miRNAs holds great promise to modulate cell activity in the context of angiogenesis. Yet, the delivery of multiple miRNAs with spatio-temporal control remains elusive. Here, we developed a plasmonic nanocarrier to control the release of two microRNAs. The nanocarrier is formed by gold nanorods (AuNRs) modified with single stranded DNA (ssDNA) for hybridization of complementary DNA-conjugated microRNAs. DNA strands with distinct melting temperatures allow independent release of each microRNA with a near infrared (NIR) laser using the same wavelength but with different powers. Tests in human outgrowth endothelial cells indicate that this system can be used to silence different targets sequentially and to modulate cell activity with spatio-temporal resolution.

.

**Keywords**. nanoparticles, microRNA, light-triggerable materials, modulation of cell activity

# 3.1- Introduction

Ischemic diseases are a leading cause of morbidity and mortality in the contemporary world. Several pre-clinical and clinical trials are exploring the therapeutic effect of cell-based therapies, including endothelial progenitor cells in ischemic diseases.[295-297] Outgrowth endothelial cells (OECs), a sub-population of endothelial progenitor cells[298], are of particular interest in the treatment of ischemic diseases[299, 300] and in tissue engineering applications[301], contributing to the vascularization of tissue constructs. It is now established that the rates of survival and vascular engraftment of transplanted cells are very poor, thus forcing transplanted cells to work mainly *via* time-limited paracrine actions. Therefore, the development of strategies to modulate the activity of these cells (e.g. proliferation, survival, etc.) is highly desirable to enhance their therapeutic effect. In this setting, the transplantation of cells transfected with modulators that are activated at specific times during cell homing and engraftment can be seen as a promising strategy.

MicroRNAs (miRNAs) are non-coding single-stranded RNAs that function as endogenous pos-transcription regulators of gene expression and have the ability to affect several biological processes, including differentiation, cell proliferation and survival.[2] Previous studies have demonstrated that miRNAs are powerful modulators of angiogenesis[302], that may act cooperatively to regulate angiogenic factors such as VEGF.[303] The hypothesis of this work is that the intracellular delivery of two miRNAs (miR-302a-3p and miR-155-5p) may regulate either cell proliferation or cell survival depending in their temporal delivery. MiR-302a-3p regulates cell cycle[304] while miR-155-5p regulates cell survival by targeting hypoxia inducible factor 1 alpha.[305] To control the intracellular delivery of miRNAs we have developed a nanocarrier that is triggerable by near infrared light (NIR). Previous studies have demonstrated the use of these nanocarriers for the spatio-temporal delivery of single miRNAs[306] and siRNAs[91, 95, 168, 175] to modulate cell activity. In this case, the RNA molecules were encapsulated in nanocarriers[306] or immobilized in the surface of the nanocarrier by electrostatic[95, 103] or hybridization[168, 175] with complementary oligonucleotides. The release was induced by the photodisassembly of the NP[306], thermal de-hybridization of the RNA molecules[175], thermal dissociation from a polycationic linker[91], or the cleavage of the linker containing the RNA from the nanoparticle surface.[95] However, so far, no light-responsive formulation has shown the precise control over the release of more than one miRNA.

In this study we developed a platform for the intracellular delivery of more than one miRNA that combines high nanocarrier uptake, efficient endolysomal escape and rapid delivery of each miRNA varying the power of a single pulse laser. The plasmonic gold nanocarrier (AuNRs) was modified with different single stranded DNA (ssDNA) that act as

linkers to immobilize miRNAs on the gold surface through hybridization of complementary strands. Upon excitation at 780 nm, a photothermal effect induces dehybridization of complementary strands.[103] The chemistry and the density of the ssDNA linkers were optimized to have sequences with specific melting temperatures and distinct release profiles after activation by a unique NIR laser source. To enhance the uptake of the nanocarriers and destabilize the endolysomal membranes during the intracellular uptake of nanocarriers we have used a peptide with membrane-perturbing abilities[222, 229], cecropin mellitin (CM). We have demonstrated initially the activity of the released of both miRNAs in a reporter cell line sensitive to miR-155-5p and miR-302a-3p. Finally we demonstrated the biological activity of the sequential release of both miRNAs in outgrowth endothelial cells (OECs) derived from human cord blood $CD34^+$ cells.

# 3.2 Results and Discussion

## 3.2.1 - Preparation of AuNR-miR conjugates

The AuNRs used in this work had an average length of 46.7 ± 4.1 nm and width of 13.8 ± 1.9 nm and showed a plasmon resonance band at 780 nm (**Figure 3.2**). The AuNRs were coated with ssDNA containing a thiol terminal group at the 5′ end to facilitate the covalent attachment to the AuNR surface (**Figure 3.1**). The two ssDNA tested in this work had a poly-thymine spacer (12 or 15 thymines) followed by an oligonucleotide sequence of 15 or 13 bases, respectively (**Table 3.1**, Materials and Methods). The poly-thymine spacer was used to keep the oligonucleotide hybridization sequence distant from the AuNR surface.[204] The number of ssDNA per AuNR was on average 475.5 ± 20, with a coupling efficiency of ssDNA to AuNR of nearly 60%.

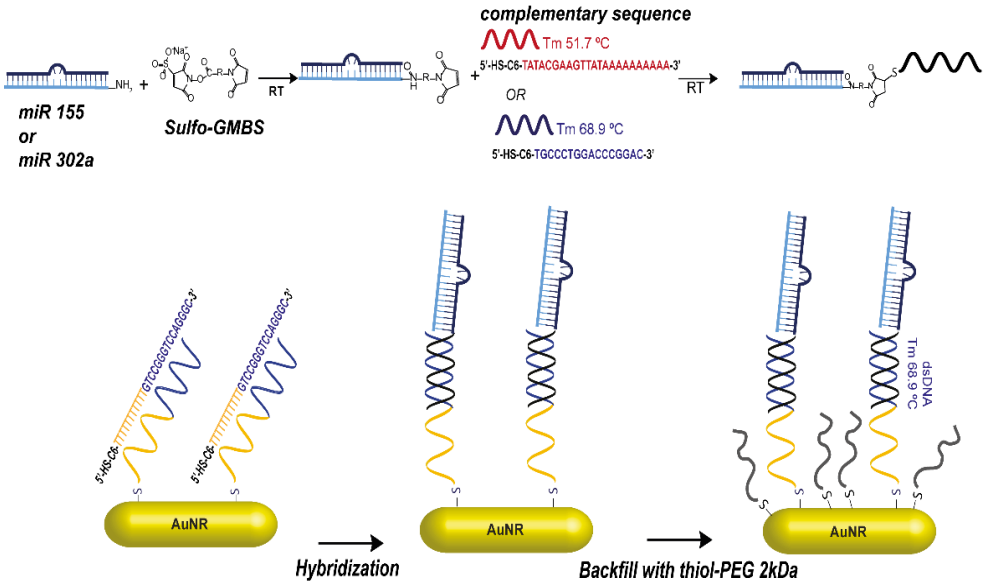


**Figure 3.1- Preparation of miR-dsDNA-AuNR conjugates.** (a) Preparation of miR-ssDNA conjugates. miR-155-5p or miR302a were initially reacted with a heterofunctional linker (Sulfo-GMBS) by its terminal succinimide ester. The miR conjugate was then reacted with a ssDNA modified with a terminal thiol group (HS-ssDNA). After reaction, the miR-ssDNA conjugates (miR155-ssDNA$_{51.7}$ or miR302a-ssDNA$_{68.9}$) were purified by HPLC. (b) Preparation of AuNRssDNA. AuNRs were reacted with HS-ssDNA complementary to the strands of miR155-ssDNA or miR302a-ssDNA conjugates. ssDNA-miR conjugates were then bound to the ssDNA-AuNR by hybridization. The surface of AuNR was then filled with 2 KDa thiol-PEG. Upon NIR irradiation, there is an increase in the temperature at the AuNR leading to the DNA dehybridization and the release of miRs with different kinetics. The release kinetic depends on the heat generated (which depends on the power of NIR laser used) and the melting temperature of the ssDNA.

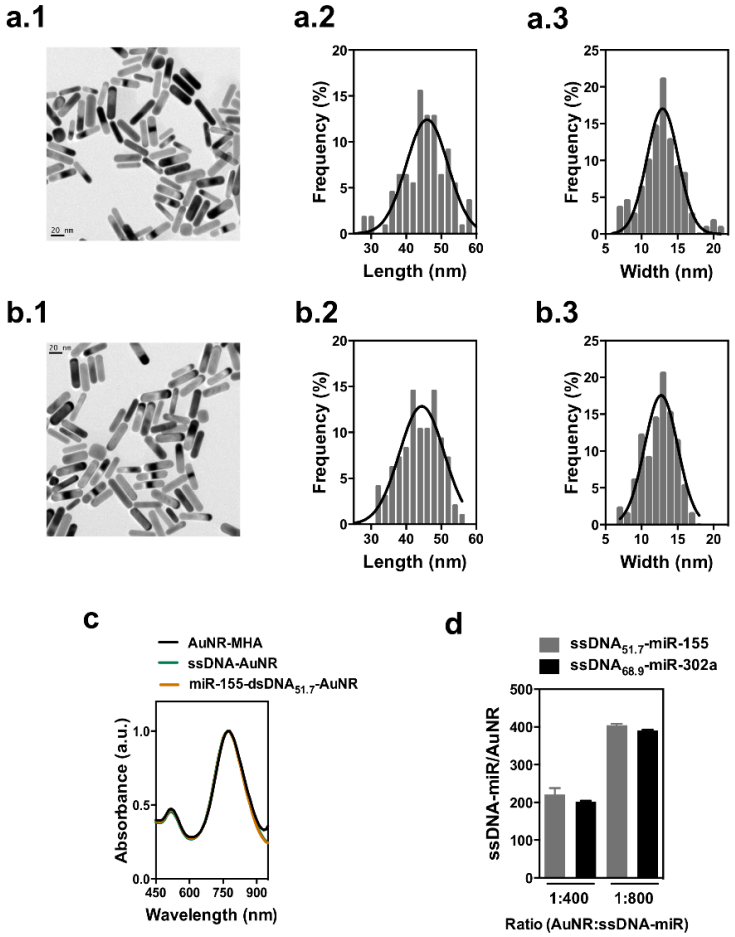


**Figure 3.2 - Characterization of AuNRs.** (a.1 and b.1) Representative TEM image of AuNRs (a.1) and AuNRs-dsDNA$_{51.7}$-miR-155 (b.1). NR length (a.2 and b.2) and width (a.3 and b.3) distribution obtained from TEM images. The AuNRs showed an average length of 46.7 ± 4.1 nm, n=100 AuNRs and an average width of 13.8 ± 1.9 nm, n=100 AuNRs. (c) Absorbance spectra of AuNRs after conjugation with mercaptohexanoic acid (AuNR-MHA); after conjugation with ssDNA$_{51.7}$ (AuNRssDNA$_{51.7}$) and after hybridization with miR-155 (AuNR-dsDNA$_{51.7}$-miR-155). Surface plasmon resonance band does not change significantly during surface modification. d) Number of miR-155-ssDNA51.7 and miR-302a-ssDNA68.9 conjugates hybridized on AuNRs modified with an average of 475 ssDNAs per AuNR (ssDNA$_{51.7}$ or ssDNA$_{68.9}$). The number of miR-ssDNAs hybridized on AuNRs was determined indirectly in the supernatant using SyBr Gold fluorescent dye. Results in b.1 and b.2 are Average ± SD, n=3.

To immobilize miRNAs on AuNRs, initially miR-155-5p and miR-302a-3p modified with a terminal amine group were reacted with the succinimidyl ester of sulfo-GMBS and then with ssDNA containing a terminal thiol group (**Figure 3.1 a**). To prevent miRNA loss of activity due to conjugation with a ssDNA, each miRNA was conjugated with ssDNA through the sense strand, guaranteeing the structural integrity of the antisense strand, in particular the 5' terminus, which is important for initiating RNA interference mechanism.[307] The conjugation efficiency, i.e., the percentage of miRNA conjugated with thiolated ssDNA, was 39% for miR-155-5p and 22% for miR-302a (**Figure 3.3**).

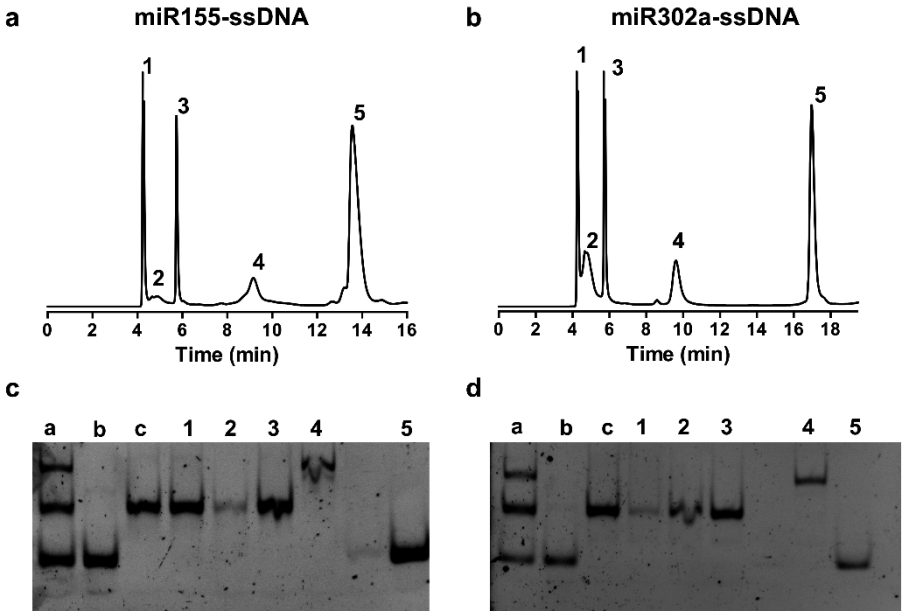


**Figure 3.3- Characterization of miR-ssDNA conjugates.** Chromatograms of the HPLC purification of (a) miR-155-ssDNA$_{51.7}$ and (b) miR-302a-ssDNA$_{68.9}$. Integration of peaks indicate that 39% and 22% of the miR-155 and miR-302a were conjugated with ssDNA, respectively. (c) and (d) Characterization of HPLC fractions by electrophoresis. Lines a, b and c are relative to the reaction mixture, control miRNA and control ssDNA, respectively. Lines 1-5 are relative to the HPLC fractions represented in each chromatogram. Fraction 4 corresponds to miR-ssDNA conjugates.

The activity of each miRNA was monitored before and after conjugation with ssDNA, using lipofectamine RNAimax as transfection agent in a reporter cell line (HEK-293T). In the concentration range tested (0.05 to 5 nM), the fluorescence of the reporter cell line decreases according to the concentration of miRNA used (**Figure 3.4**). Both miRNAs are active after conjugation with ssDNA, although miR-302a-ssDNA conjugate is slightly less active than miR-302a at the lowest concentrations tested (0.05-0.5 nM) (**Figure 3.4**).

To hybridize miR-ssDNA conjugates to ssDNA-AuNRs, the conjugates were incubated in large excess with ssDNA-AuNRs (400 or 800-molar fold ratio) at 37 ºC leading to the immobilization of 202 (400-molar fold ratio) and 390 (800-molar fold ratio) ssDNA-miR-155 conjugates per AuNR or 226 and 404 ssDNA-miR-302a per AuNR (**Figure 3.2**). Therefore the hybridization efficiency of ssDNA-miR conjugates to ssDNA-AuNRs was between 48.75 and 56.5%. For subsequent experiments we have used AuNRs with ca. 400 miR-ssDNA conjugates because this number was large enough for biological output (see below). Our results show that hybridization of the miRNA-ssDNA conjugate does not cause significant changes in the absorbance spectrum of the AuNRs (**Figure 3.2 c**). In addition, the size of

the nanocarrier was not substantially different from the non-conjugated one (**Figure 3.2 a and 3.2 b**).

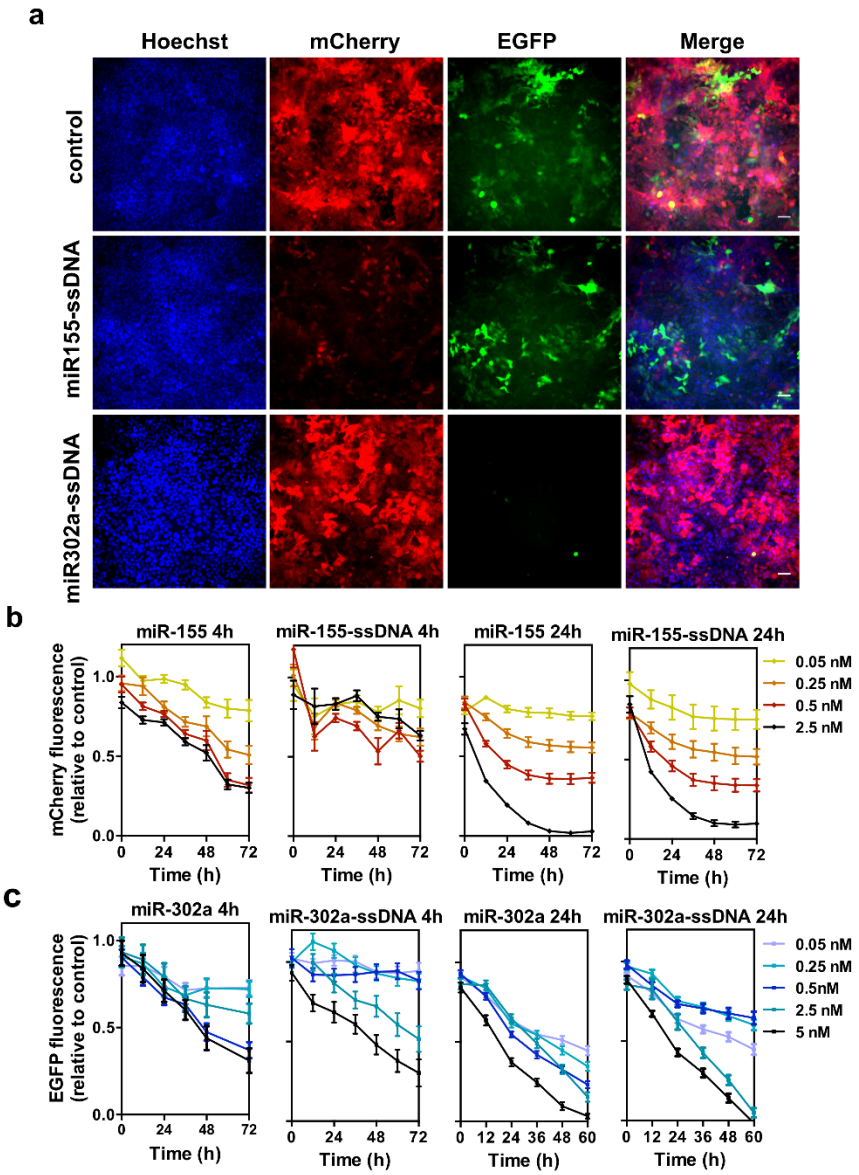


**Figure 3.4 - Transfection of miRNAs and ssDNA-miR conjugates with lipofectamine.** (a) Fluorescence microscopy images of HEK-293T cells transfected with different miR-ssDNA conjugates. Images correspond to 24 h transfection with 2.5 nM miR-ssDNA conjugates (60 h after transfection). Scale bar corresponds to 50 μm. (b and c) HEK-293T cells were transfected with lipofectamine RNAimax complexed with miR-155-ssDNA$_{51.7}$ or miR-302a-ssDNA$_{68.9}$. Cells were exposed to the conjugates for 4 h or 24 h and their fluorescence was monitored afterwards in a high content fluorescence microscope. EGFP and mCherry fluorescence were normalized to the control (cells transfected with scramble miRNA).

### 3.2.2 - Release profiles of ssDNA-miR conjugates from miR-dsDNA-AuNR

Collectively, in the current work we have used ssDNA with different melting temperatures as linkers for miRNA immobilization. The distinct melting temperatures allow us differential release profiles for each miRNA with the possibility of delivering sequentially two miRNAs. The use of ssDNA has been reported for the immobilization of siRNAs on plasmonic nanocarriers; however, the ssDNA did not confer a specific release profile to the biomolecule, since the release was obtained through the cleavage of thiol-gold bonds.[168] The controllable aspect ratio of gold nanorods allows the differential release of different biomolecules, such as DNA oligonucleotides, from carriers of different sizes, although it requires lasers with different wavelengths.[169] In the present work, the differential release is modulated by varying the linkers that attach the miRNA to the gold surface and not by changing the size of the nanocarrier, allowing the use of a single wavelength. Therefore, different stimuli can be applied by tuning the time and power of the laser.

To study the release profiles of miRNAs, we have used AuNRs hybridized with: (i) miR-155-5p conjugated with ssDNA with a melting temperature of 51.7 ºC (miR-155-ssDNA$_{51.7}$) and (ii) miR-302a conjugated with ssDNA with a melting temperature of 68.9 ºC (miR-302a-ssDNA$_{68.9}$) (**Figure 3.5**). Each suspension of miR-dsDNA-AuNR was irradiated for 2 or 5 min and immediately centrifuged. Our results show that miR-155 is released at 1.25 Wcm$^{-2}$ (miR-155: 76% and 99% for 2 and 5 min; miR-302a: 9.6% and 18% for 2 and 5 min) while miR-302a is largely released at 2 Wcm$^{-2}$ (2 min: 54.9%; 5 min: 87.4%) (**Figure 3.5 b**). The supernatants of each formulation were then complexed for 20 min with lipofectamine RNAimax and added to HEK-293T cells for 4 h (**Figure 3.5 a**). The concentration of miR-155-ssDNA$_{51.7}$ released with a laser stimulus of 1.25 Wcm$^{-2}$ for 2 min is able to induce 80% decrease in mCherry fluorescence (**Figure 3.5 d**). Increasing the time or the power of the laser does not decrease significantly mCherry fluorescence when compared to 2 min laser stimulus at 1.25 Wcm$^{-2}$. In contrast, the concentration of miR-302a released with a laser stimulus for 2 or 5 min at 1.25 Wcm$^{-2}$ does not induce a significant decrease in EGFP fluorescence 48 h after transfection (**Figure 3.5 f**). Yet, the increase of laser power from 1.25 Wcm$^{-2}$ to 2 Wcm$^{-2}$ for 2 min leads to almost 40% decrease in EGFP fluorescence signal. NIR laser-induced release of miR-ssDNA conjugates correlates with the power of the laser and the melting temperature of the DNA strands, i. e. miR conjugated with higher melting temperature ssDNA (68.9 ºC) requires a higher laser power to be released from the AuNR surface. In each case, the fluorescence of the protein that is not targeted by each miRNA remains constant (EGFP for miR-155-dsDNA-AuNR and mCherry for miR-302a-dsDNA-AuNR), meaning that cell fluorescence did not change significantly as a consequence of the transfection procedure.

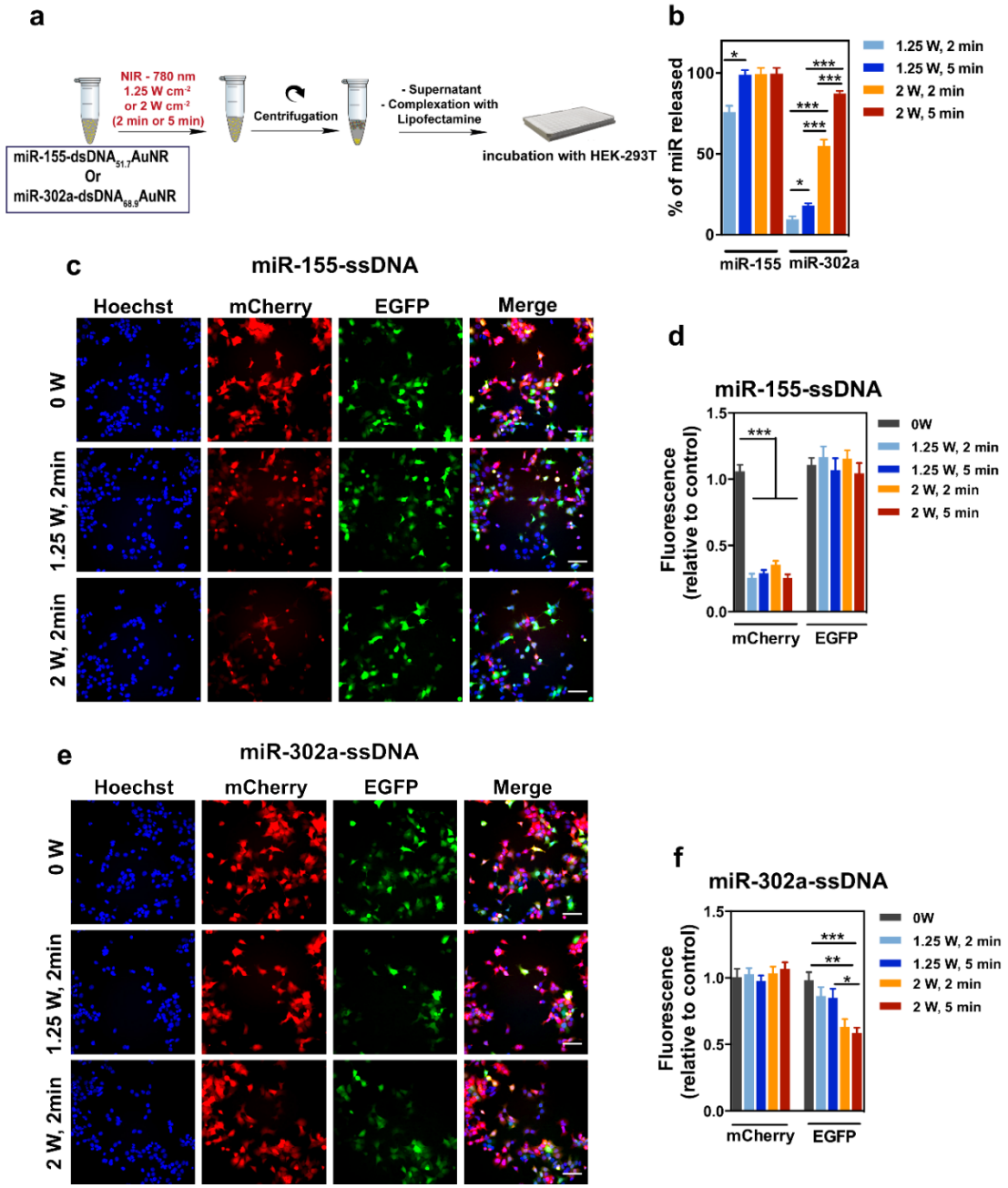


**Figure 3.5 - EGFP and mCherry knockdown in HEK-293T after laser induced release of miRssDNA conjugates**. (a) schematic representation of the experimental protocol. Suspensions of miR-155-dsDNA$_{51.7}$-AuNR or miR-302a-sDNA$_{68.9}$-AuNR were exposed to different laser stimuli at 1.25 Wcm$^{-2}$ (2 and 5 min) and at 2 Wcm$^{-2}$ (2 and 5 min). Immediately after irradiation, suspensions were centrifuged and the supernatants were complexed with Lipofectamine RNAimax and incubated in HEK-293T. (b) Percentage of miR-ssDNA released from AuNR surface. The amount of miR-ssDNA was determined using SyBr Gold fluorescent dye. (c and e) Fluorescence microscopy images of HEK-293T exposed to ssDNA-miR-155/RNAimax or ssDNA-miR-302a/RNAimax complexes for 4 h. 48 h after incubation, mCherry and EGFP fluorescence were monitored by a high content fluorescence microscope. (d and f) mCherry and EGFP fluorescence normalized to the control (supernatant of non-irradiated miR-dsDNA-AuNRs). Results are expressed as average ± SEM (n=3, with 6 microscope fields per sample)

### 3.2.3 - Uptake and endosomal escape of miR-dsDNA-AuNR

Intracellular delivery of miRNAs presents some challenges, since these biomolecules must reach the cytoplasm in order to initiate RNA interference mechanism.[2] To enhance cell uptake and endosomal escape of miR155-dsDNA$_{51.7}$-AuNRs we have used CM, a cell penetrating peptide. CM is a cationic amphiphilic peptide with membrane-perturbing capacity[230], leading to endosomal escape of membrane-impermeable molecules.[212] The effect of CM in the uptake and intracellular localization of miR155-dsDNA$_{51.7}$-AuNRs labelled with TRITC was studied using confocal microscopy and transmission electron microscopy (**Figure 3.6**). Cells were incubated with miR155-dsDNA$_{51.7}$-AuNR-TRITC (50 μg mL$^{-1}$) for 4 h in DMEM (without FBS), washed and finally characterized by confocal microscopy and inductive coupled plasma mass spectrometry (ICP-MS). Our results show that increasing intracellular levels of miR155-dsDNA$_{51.7}$-AuNR-TRITC were observed for increasing CM concentrations by confocal microscopy (**Figure 3.6 b**) and ICP-MS analyses (**Figure 3.6 d**). The colocalization of miR155-dsDNA$_{51.7}$-AuNR-TRITC with Lysotracker is lower in the presence of CM than in the absence of the peptide showing that the peptide contributes for the endolysosomal escape of the nanocarrier (**Figure 3.6 d**). However, increasing the concentration of the peptide from 5 μM to 10 μM does not decrease the coefficient of colocalization (**Figure 3.6 c**). Our results also suggest a cumulative effect of CM and laser irradiation in the endosomal escape of the miR155-dsDNA$_{51.7}$-AuNR-TRITC. The peptide destabilizes the endosomal membrane allowing the escape of part of the nanocarriers. As confirmed by TEM (**Figures 3.6 f and 3.6 g**), the NIR laser also promotes the escape of AuNRs that are still inside the endosomes, probably via a photochemical process through generation of radical species.[243] The endosomal escape promoted by CM, rather than the escape promoted by laser irradiation may be a way of expanding the time window for laser activation of AuNRs, since we reduce the chance of degradation of the cargo, assuring the integrity of the miR-dsDNA-AuNR conjugates until laser activation.

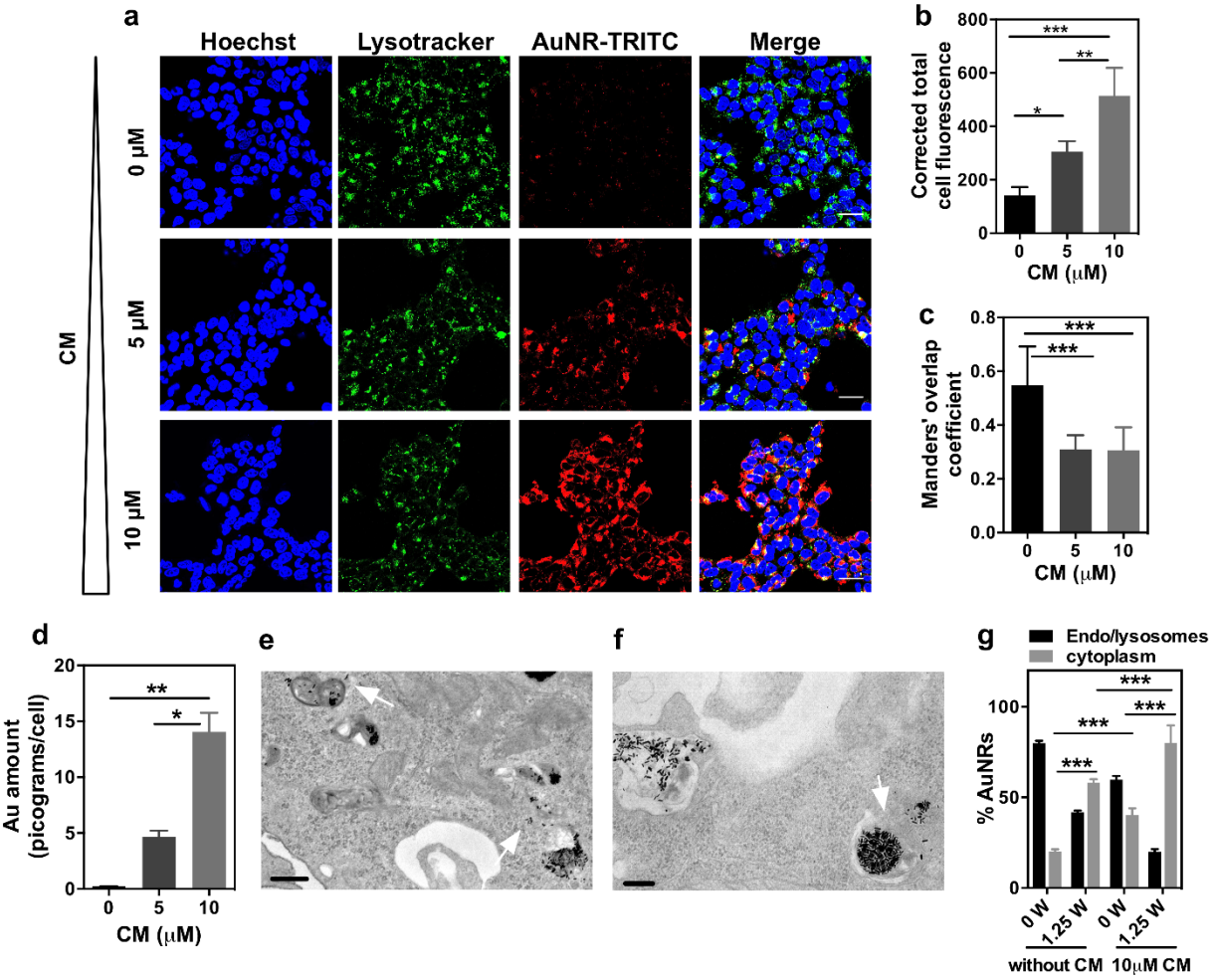


**Figure 3.6 - Uptake and intracellular localization of miR-dsDNA-AuNRs.** (a) Representative microscopy confocal images of cells stained with lysotracker green after 4 h incubation with miR-155-dsDNA$_{51.7}$-AuNR-TRITC (50 µg mL$^{-1}$) and cecropin-melittin (concentration is given in each lane). Scale bar is 30 µm. (b) Intensity of the signal of AuNR-TRITC per cell. (c) Colocalization between AuNR-TRITC and lysotracker green expressed as Manders' overlap coefficient assessed by ImageJ analysis. (d) Amount of Au per cell quantified by ICP-MS. (e) TEM image of HEK-293T incubated with miR-155-dsDNA$_{51.7}$-AuNR (50 µg mL$^{-1}$) and CM (10 µM). White arrows indicate the presence of AuNRs in the cytoplasm. Scale bar corresponds to 500 nm. (f) TEM image of HEK-293T incubated with miR-155-dsDNA-AuNR (50 µg mL$^{-1}$) and cecropin-melittin (10 µM) after 2 min irradiation at 1.25 Wcm$^{-2}$. White arrow indicates the site of rupture of the endosomal membrane. Scale bar corresponds to 200 nm. (g) Percentage of AuNRs present in the cytoplasm and vesicles (endosomes and lysosomes). Quantification results from the analysis of 30 images/condition. In b, c, d and g, results are expressed as Average ± SD (n=3). *,** and *** denote statistical significance ($p<0.05$, $p< 0.01$and $p<0.001$) assessed by one-way ANOVA followed by Tukey's post-hoc test.

### 3.2.4 - Cytotoxicity of miR-dsDNA-AuNR

To evaluate the cytotoxicity of miR-dsDNA-AuNR (we have used miR155-dsDNA$_{51.7}$-AuNR as a model), co-incubated with CM, and NIR laser radiation (up to 2 Wcm$^{-2}$), HEK-293T cells were exposed for 4 h to the nanocarrier, washed followed by their activation or not with a NIR laser for 2 min, and finally incubated for 24 h. Cell viability was measured by

a cell viability assay (Celltiter-Glo Luminescent). At 10 μM, CM causes only 8% decrease in ATP production. Moreover, in all the concentrations tested, there is no significant effect of the irradiation in cell viability (**Figure 3.7 a**). The toxicity of AuNRs and CM was also evaluated in OECs (**Figure 3.7 b**). In contrast to the results observed for HEK-293T cells, CM is cytotoxic at 10 μM, causing a significant decrease in ATP production. Likewise, it has already been described a higher cytotoxicity of this peptide and nanoparticles in endothelial cells in relation to other cell types [308], Therefore, for subsequent assays with OECs, a concentration of 5 μM of peptide was used. In agreement with what was observed in HEK-293T cells, irradiation does not have a cytotoxic effect.

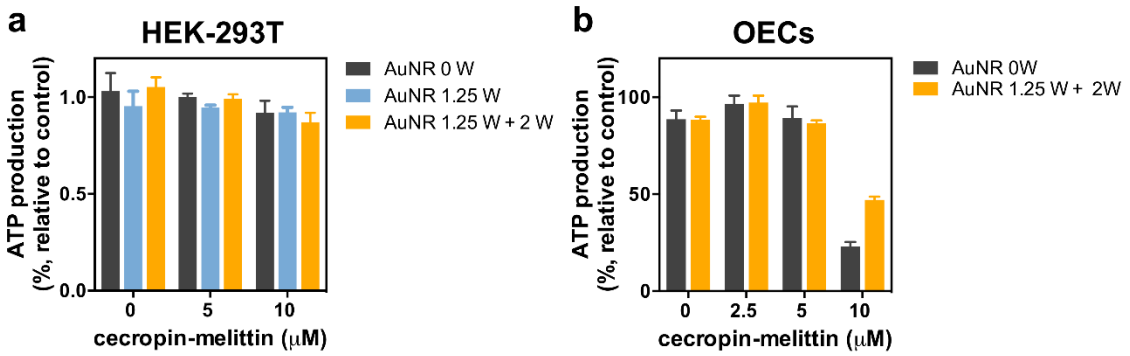


**Figure 3.7 - Cytotoxicity of AuNR-dsDNA$_{51.7}$-miR155.** (a) HEK-293T cells were incubated with DNA$_{51.7}$-AuNR (50 μg mL$^{-1}$) with or without cecropin-melittin (5 and 10 μM) for 4 h. Cells were then washed and new medium was added (DMEM with 10% FBS). Subsequently, cells were irradiated for 2 min at 1.25 Wcm$^{-2}$ and left in the incubator. After 2 h, cells were irradiated for 2 min at 2 Wcm$^{-2}$ and then incubated for additional 24 h at 37º C. (b) OECs were incubated with AuNR-dsDNA$_{51.7}$ (50 μg mL$^{-1}$) without or with CM (2.5, 5 and 10 μM) for 4 h. Then cells were washed and new medium was added (EGM-2). Subsequently, cells were irradiated for 2 min at 2 Wcm$^{-2}$ and left in the incubator for 24 h. Cell metabolism was evaluated by an ATP assay (Promega). Results are expressed as average ± SD (n=4).

### 3.2.5 – Light-induced release of miRNAs in a dual reporter cell line

To test the laser-induced release of miR-ssDNA conjugates in cells, HEK-293T cells were incubated for 4 h with miR155-dsDNA$_{51.7}$-AuNR or miR302a-dsDNA$_{68.9}$-AuNR (50 μg mL$^{-1}$). Cells were then irradiated for 2 min with different laser powers (1.25 or 2 Wcm$^{-2}$). Although 5 min of irradiation was able to release higher amount of miR-302a (Figure 3.5b), it induced more toxicity. Cells incubated with miR155-dsDNA$_{51.7}$-AuNR and activated with a laser stimuli of 1.25 Wcm$^{-2}$ or 2 Wcm$^{-2}$ showed a reduction in mCherry fluorescence around 50% after 48 h (**Figure 3.8c**). On the other hand, cells incubated with miR302a-dsDNA$_{68.9}$-AuNR and activated with a laser stimuli of 2 Wcm$^{-2}$ showed a higher reduction in EGFP fluorescence than cells irradiated at 1.25 Wcm$^{-2}$ (**Figure 3.8 d**).

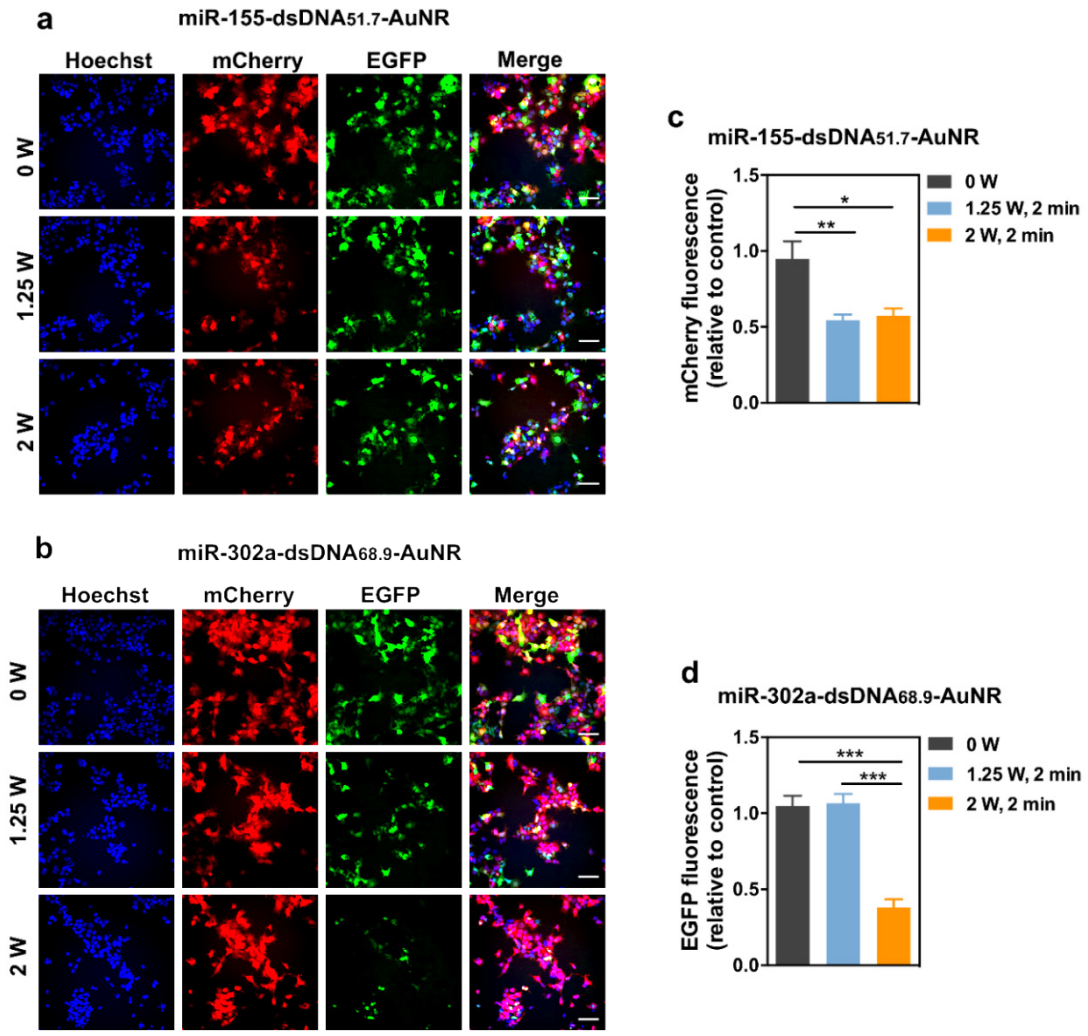


**Figure 3.8- mCherry and EGFP knockdown after laser induced release of miR-ssDNA conjugates in HEK-293T.** Fluorescence microscopy images of HEK-293T cells incubated with miR-155-dsDNA$_{51.7}$-AuNR (a) or with miR-302a-dsDNA$_{68.9}$-AuNR (b). HEK-293T were incubated with miR-155-dsDNA$_{51.7}$-AuNR or miR-302a-dsDNA$_{68.9}$-AuNR (50 μg mL$^{-1}$) and CM (10 μM) for 4 h and then irradiated at 1.25 or 2 Wcm$^{-2}$ for 2 min. 48 h after irradiation, cell fluorescence was monitored in a high-content fluorescence microscope. Scale bar corresponds to 100 μm. c) Normalization of mCherry fluorescence in cells incubated with miR-155-dsDNA$_{51.7}$-AuNR. d) Normalization of EGFP fluorescence in cells incubated with miR-302adsDNA$_{68.9}$-AuNR. Results are expressed as average ± SEM (n=3, with 4 microscope fields per replica)

For the sequential release of miR-155 and miR-302a, cells were incubated with miR155-dsDNA$_{51.7}$-AuNR (25 μg mL$^{-1}$) and miR302a-dsDNA$_{68.9}$-AuNR (25 μg mL$^{-1}$) for 4 h. After incubation, cells were irradiated for 2 min at 1.25 Wcm$^{-2}$. A second stimulus (2 min, 2 Wcm$^{-2}$) was applied 2 h after the first stimulus (**Figure 3.9 a**). MiR-155-5p, which is conjugated to the oligonucleotide with lower melting temperature (Tm 51.7 ºC), was preferentially released with the first stimulus. This release of miR-155 correlates with a 42% decrease in mCherry fluorescence 48 h after the stimulus (**Figure 3.9 c**). On the other hand,

miR-302a which is conjugated to the oligonucleotide with higher melting temperature (Tm 68.9 ºC), is not released with irradiation at 1.25 $Wcm^{-2}$, thus, no significant decrease in EGFP was observed. Knockdown of EGFP (41% decrease in EGFP at t=48 h after irradiation) was only detected when a higher energy stimulus (2 min, 2 $Wcm^{-2}$) was applied (**Figure 3 c**).

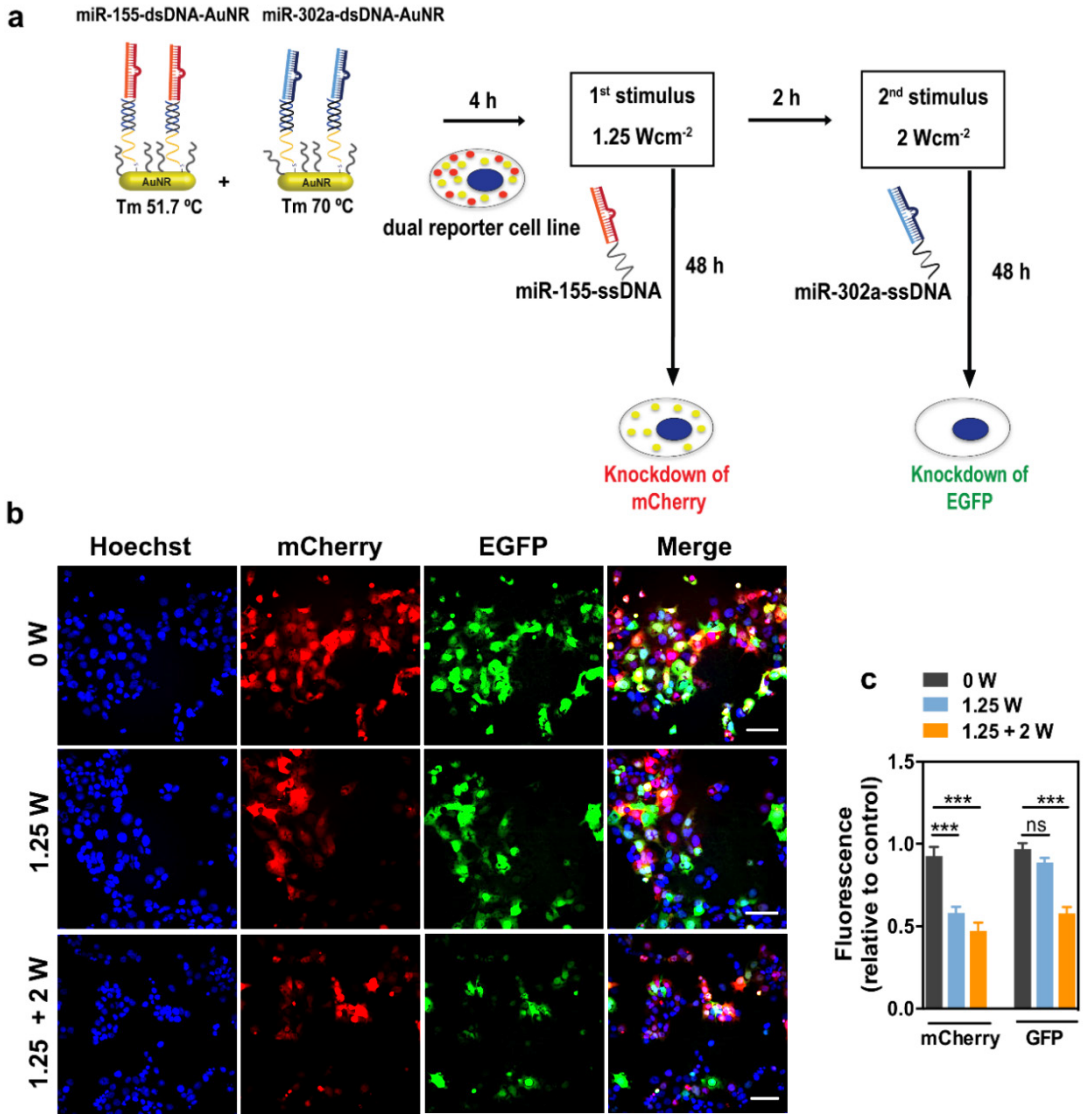


**Figure 3.9 - Sequential delivery of miRNAs in HEK-293T.** (a) Schematic representation of the protocol used. HEK-293T were incubated with a mixture of miR155-dsDNA$_{51.7}$-AuNR (25 μg $mL^{-1}$) and miR302a-dsDNA$_{68.9}$-AuNR (25 μg $mL^{-1}$) for 4 h. After incubation cells were exposed to one laser stimulus (2 min at 1.25 $Wcm^{-2}$) or two laser stimuli (2 min 1.25 $Wcm^{-2}$ and 2 min at 2 $Wcm^{-2}$) with an interval of 2 h between each stimulus. (b) Fluorescence microscopy images of cells incubated with miR-155-dsDNA-AuNR and miR-302a-dsDNA-AuNR for 4 h in the presence of CM (10 μM). (c) Quantification of cell fluorescence 48 h after laser irradiation. Results are expressed as average ± SEM (n=3, with 6 microscope fields per replica). * and *** denote statistical significance ($p<0.05$ and $p<0.001$) assessed by one-way ANOVA followed by Tukey's post-hoc test

### 3.2.6 – Light-induced release of miRNAs in OECs

To test the potential of this delivery system in the modulation of cell activity, we incubated OECs with miR-dsDNA-AuNR (50 μg $mL^{-1}$). Cell response to each miRNA was evaluated in terms of proliferation (by cell nuclei counting) and survival (by cell nuclei counting) in hypoxia (**Figures 3.10 a and 3.10 b**). The impact of each miRNA was first evaluated in transfection assays with lipofectamine. MiR-155 does not promote proliferation, but is able to increase survival, whereas miR-302-a promotes cell proliferation but does not have a positive impact in survival. The combined effect of both miRNAs induces proliferation and increases survival (**Figure 3.11**) to a level that is equivalent to the effect of vascular endothelial growth factor (VEGF). In endothelial cells, miR-155 has already been reported as being cytoprotective under stress conditions[309]. Relatively to the assay with miR-dsDNA-AuNR, there is a significant increase (6.7 fold) in survival with the first stimulus (2 min at 1.25 $Wcm^{-2}$) (**Figure 3.10 c**), which is indicative of light-induced release of miR-155. Regarding proliferation (**Figure 3.10 b**), there is a slight increase with the first stimulus, increasing more with the second stimulus (2 min at 1.25 $Wcm^{-2}$). This might be indicative of a slight release of miR-302a with the first stimulus, which is less than 10% according to the laser-induced release profile (**Figure 3.5 b**), although in HEK-293T the effect of this release in the knockdown of EGFP was not significant (**Figure 3.9 c**).

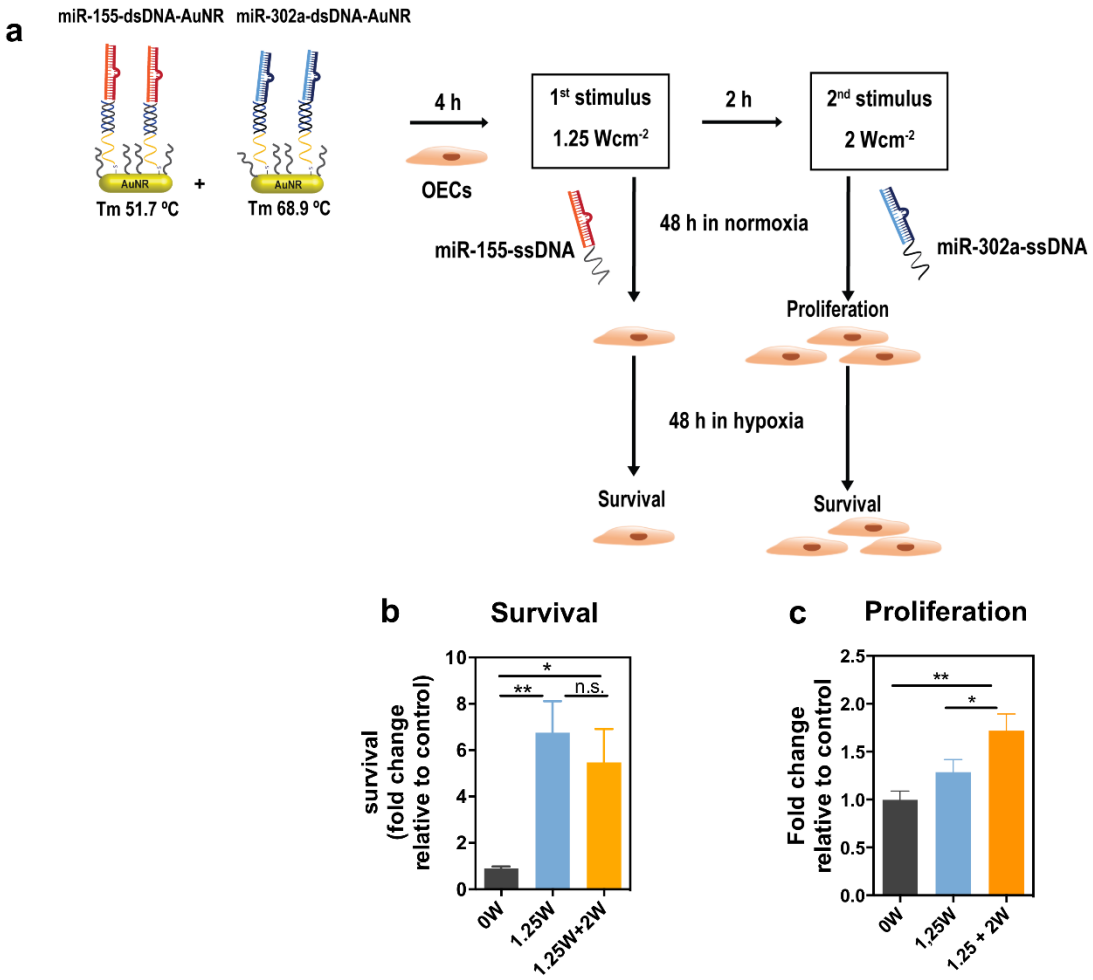


**Figure 3.10- Sequential delivery of miRNAs in OECs.** (a) Schematic representation of the experiment. OECs were incubated for 4 h with a mixture of miR155-dsDNA$_{51.7}$-AuNR (25 µg mL$^{-1}$) and miR302a-dsDNA$_{68.9}$-AuNR (25 µg mL$_{-1}$) for 4 h. After incubation, cells were exposed to one laser stimulus (2 min at 1.25 Wcm$^{-2}$) or two laser stimuli (2 min 1.25 Wcm$^{-2}$ and 2 min at 2 Wcm$^{-2}$) with an interval of 2 h between each stimulus. (b) Cell proliferation. After irradiation, cells were kept in the incubator for 48 h, after which proliferation was assessed in terms of cell nuclei (DAPI staining). Then cells were incubated under hypoxic conditions for 48 h. (c) Survival was determined as the ratio between the final (after hypoxia) and the initial number (after hypoxia) of cells. Cells incubated with AuNR without miRNAs were used as control. Results are expressed as average ± SEM (n=5). * and ** denote statistical significance ($p<0.05$ and $p<0.01$) assessed by one-way ANOVA followed by Tukey's post-hoc test.

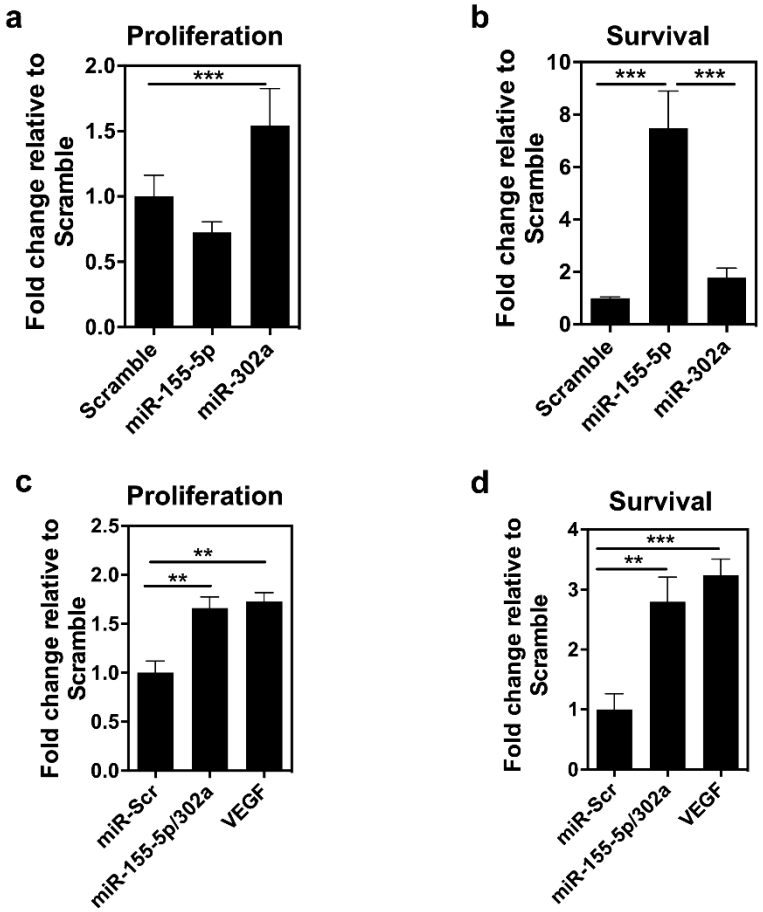


**Figure 3.11 - Impact of miR-155 and miR-302a on proliferation and survival of OECs**. OECs were incubated for 48 h with miR-155 and miR-302a complexed with Lipofectamine RNAimax. (a) After incubation proliferation was assessed in terms of number of cells. Then cells were incubated under hypoxic conditions for additional 48 h. (b) Survival was determined as the ratio between the final (after hypoxia) and the initial number (before hypoxia) of cells. c) Combined effect of 4 h incubation with miR-155 and miR-302a complexed with Lipofectamine on cell proliferation. Proliferation was assessed 48 h after incubation with miRNAs. Then cells were incubated under hypoxia for 48 h, after which (d) cell survival was determined. Cells incubated with scramble miR and lipofectamine were used as control. Results are expressed as average ± SEM (n=5).

## 3.3- Conclusions

Combinatorial RNAi therapies are being explored for the treatment of different diseases, which has also encouraged the development of new nanocarriers for multiple RNAi therapeutic delivery with controlled stoichiometry.[310-313] Additionally, light-sensitive systems have received increasing attention due to the possibility of controlling spatially and temporally intracellular delivery of drugs, increasing their therapeutic potential[64, 65, 314] However, there is still a lack of systems for controlled release of each therapeutic independently. Controllable silencing of multiple genes, either simultaneous or sequentially, can mimic the spatio-temporal patterns of natural biological processes and may be a promising strategy for therapeutic purposes and also for fundamental research, for example in the study of genetic interactions or in the development of phenotypic assays that require spatio-temporal regulation.[315, 316] Angiogenesis is particularly dependent on the ordered expression of multiple miRNAs that control proliferation, cell survival, migration and mobilisation of cells[317]. Although some formulations have been developed for delivery of miRNAs to modulate the behaviour of endothelial cells and promote angiogenesis[268, 270], the synergistic effect of multiple miRNA delivery has not been explored yet. In this work, we have developed a light-responsive system that, by the addition of an antimicrobial peptide, can be internalized in higher amounts and escape the endosomes to deliver more than one miRNA, working as an optical switch of biological circuits involved in cell proliferation and survival with spatial and temporal control. In conclusion, the important modulatory nature of miRNAs combined with the spatio-temporal precision in their delivery, leverages the potential of this technology for several biomedical applications.

## 3.4- Materials and Methods

**Materials.** hsa-miR-155-5p and hsa-miR-302a-3p with a terminal amine group in the passenger strand were purchased from Dharmacon (GE Healthcare), thiolated oligonucleotide strands, hexadecyltrimethylammonium bromide (CTAB), sodium borohydride ($NaBH_4$), silver nitrate ($AgNO_3$), hexanethiol and mercaptohexanoic acid, and other chemicals were all purchased from Sigma-Aldrich and used as received without further purification. Sodium dodecyl sulfate (SDS) was purchased from VWR. Bovine Serum Albumin (BSA), DyLight-NHS ester, N-[γ-maleimidobutyryloxy] sulfosuccinimide ester (sulfo-GMBS), LysoTracker® Green DND-26, LysoTracker® Red DND-99, fetal bovine serum (FBS) and trypsin-EDTA solution were purchased from Thermo Fisher Scientific. Dulbecco's Modified Essential Medium (DMEM) is a commercial product of Merck Millipore. Purified water with resistivity above 18.2 $M\Omega.cm^{-1}$ was obtained by reverse osmosis (MilliQ, Millipore). Other reagents were analytical grade.

**AuNR synthesis**. AuNRs were prepared using the seed mediated method.[155] For the preparation of the seed solution, gold(III) chloride hydrate ($HAuCl_4$, 0.1 M, 12.5 µL) was added to a hexadecyltrimethylammonium bromide (CTAB) solution (0.1 M, 5 mL) and stirred vigorously for 5 min, after which an ice-cold sodium borohydride solution ($NaBH_4$, 10 mM, 0.3 mL) was added. After stirring for 2 min the solution was kept at 25 ºC. For the preparation of growth solution, silver nitrate ($AgNO_3$, 5 mM, 3.2 mL) was added to CTAB solution (0.1 M, 200 mL) and mixed gently, after which $HAuCl_4$ (50 mM, 2 mL) was added. After mixing, ascorbic acid (0.1 M; 1.5 mL) was added. The solution changed from dark yellow to colourless. Finally, 1.5 mL of the seed solution (aged for 8 min at 25 ºC) was added to the growth solution. The solution was kept at 28 ºC for 2 h. The NRs were washed by centrifugation at 9000 g and resuspended in water.

The CTAB on the AuNR surface was replaced using a method already reported with some modifications.[191] Hexanethiol (1.5 mL) was added to the NR-CTAB suspension (2.5 nM; 1 mL). Then, acetone (3 mL) was added and the mixture was swirled for a few seconds. The aqueous phase became clear indicating ligand exchange and the organic phase containing the AuNRs was extracted. Then, a mixture of toluene (2 mL) and methanol (5 mL) was added to the organic phase. The solution was centrifuged at 5.000 g, 10 min, and the pellet was resuspended in 0.5 mL of toluene by brief sonication. The organic to aqueous phase was performed as follows. AuNR-hexanethiol (1 mL) in toluene was added to 9 mL of mercaptohexanoic acid (MHA, 5 mM, 9 mL) in toluene at 95 ºC. The reaction proceeded under reflux with magnetic stirring for 15 min. The precipitation of AuNRs indicated successful coating by MHA. After cooling to room temperature, the aggregates were washed

twice with toluene by decantation. Finally, the NRs were washed with isopropanol to deprotonate the carboxylic groups and then the aggregates were redispersed in 1× TBE. The ligand exchange was confirmed by zeta potential measurements.

**Functionalization of NR-MHA with single strand DNA (ssDNA)**. Thiolated ssDNA (sequence A 5'-HS-C6-TTTTTTTTTTTTTTTATAACTTCGTATA-3' or sequence B 5'- HS-C6-TTTTTTTTTTTGTCCGGGTCCAGGGC-3', purchased from Sigma-Aldrich) were reduced for 1 h with 100-fold excess of Tris(2-carboxyethyl)phosphine (TCEP) over ssDNA. The NR suspension (0.5 nM; 0.5 mL) was incubated with the thiolated ssDNA for 3 h in a molar ratio of 1:800 in 10 mM phosphate buffer pH 7.4 containing 0.3% (w/v) of sodium dodecyl sulfate (SDS). Afterwards, a NaCl solution (22.5 µL; 0.45 M) was added every 60 min to the AuNR suspension. This operation was repeated four times and the suspension shaked overnight to improve the reaction yield. In the following day, the NR suspension was centrifuged at 9000 g, the supernatant was collected and the pellet was resuspended in 10 mM phosphate buffer with 30 mM NaCl. The amount of oligonucleotides was determined by measuring absorbance at 260 nm in the supernatant. The ssDNA-AuNRs obtained were stored at 4 ºC before use (not more than one week).

**Preparation of micro-RNAs conjugated with ssDNA**. miR-ssDNA conjugates were prepared using N-[γ-maleimidobutyryloxy]sulfosuccinimide ester (sulfo-GMBS, Thermo Scientific) as linker. miR-155 or miR-302 (60 µL at 100 µM in PBS pH 8.0) were reacted with sulfo-GMBS in a 100-fold molar ratio for 30 min at room temperature. The excess of linker was removed by ultrafiltration with Nanosep 30 kDa (Pall Corporation). The buffer was exchanged by PBS pH 7.0 and the purified miR (60 µL; 100 µM in PBS pH 7.0) was reacted with thiolated DNA (60 µL; 200 µM in PBS pH 7.0) in a final volume of 200 µL of PBS for 2 h at room temperature. Before conjugation DNA strands were reduced with 100-fold excess of TCEP for 1h at 37 ºC. DNA strands were complementary to the strands immobilized on the NR surface (complementary sequence A: 5'-HS-C6-TATACGAAGTTATAAAAAAAAAA; complementary sequence B: 5'-HS-C6-TGCCCTGGACCCGGAC). miR-155 was conjugated with ssDNA complementary sequence A (Tm 51.7 ºC) and miR-302a was conjugated with ssDNA complementary sequence B (Tm 68.9 ºC).

**Table 3.1 – ssDNA sequences used for modification of AuNRs and conjugation with miRNAs**

| | Tm / ºC | sequence |
|---|---|---|
| **AuNR conjugation** | 51.7 | 5'-HS-C6-TTTTTTTTTTTTTTTATAACTTCGTATA-3' |
| | 68.9 | 5'-HS-C6-TTTTTTTTTTTTGTCCGGGTCCAGGGC-3' |
| **miR-ssDNA conjugates** | 51.7 | 5'-HS-C6-TATACGAAGTTATAAAAAAAAAA-3' |
| | 68.9 | 5'-HS-C6-TGCCCTGGACCCGGAC-3' |

**Purification of miR-ssDNA conjugates by reverse-phase ion-pair liquid chromatography.** The products of miR and ssDNA conjugation were separated in a Shimadzu-LC-20AD system using a 4.6 x 250 mm XBridge C18 column packed with 3.5 µm particles, average pore diameter 130 Å (Waters). The mobile phases were as follows: 0.1 M TEAA pH 7.0 (A) and acetonitrile (B). The gradient started in 14% of B to 19% of B in 23 min. The flow rate was 0.55 mL $min^{-1}$. The acetonitrile present in the fraction containing the miR-ssDNA conjugate was removed in a rotary evaporator. The final volume was aliquoted and stored at -20 ºC.

**Characterization of miR conjugated with ssDNA by non-denaturing PAGE.** The reaction mixture obtained after reacting miR-155 or miR-302 with ssDNA and the fractions obtained after HPLC purification of the reaction mixture were analysed by gel electrophoresis. Reaction mixture (15 µL) and reaction mixture fractions obtained after HPLC purification (15 µL) were mixed with glycerol (5 µL; glycerol in 50% v/v of $H_2O$), loaded in a polyacrylamide gel (12%, w/v) and run for 45 min in 0.5 x TBE at 140 V. The gel was stained with SyBr Gold (1:5000 in 1 x TBE) for 10 min and imaged in a UV transilluminator (Molecular Imager Gel DOC, Biorad).

**Labelling of NR-ssDNA with TRITC.** Thiol-PEG-amine 1 kDa (Creative PEGworks, 20 nmol) was reacted with TRITC (20 nmol) in 1 mL of 10 mM carbonate buffer at pH 9.0 for 2 h at room temperature. Then 500 µL of NR-ssDNA (0.5 nM) were incubated overnight with thiol-PEG-TRITC in a molar ratio of 1:1000. The excess of fluorophore was removed in two steps of centrifugation at 9000 g. The supernatants were then quantified for the presence of TRITC by fluorescence spectroscopy.

**Immobilization of miR-ssDNA conjugates in AuNRs**. For the hybridization of complementary oligonucleotide strands conjugated with miR, a suspension of AuNR-ssDNA (0.5 nM) was incubated with DNA-miR conjugates (400 nM) for 1 h at 37 ºC and then the temperature was slowly decreased to 25 ºC. The excess of DNA-protein conjugate was

removed by centrifugation. The amount of miR-ssDNA immobilized on the AuNRs was determined indirectly by measuring the concentration in the supernatant. For that, the supernatant was collected and incubated with SyBr Gold (diluted 1:10000). The fluorescence was measured in a Synergy HT microplate reader (excitation 495 nm, emission 537 nm) and the concentration was extrapolated from a calibration curve.

**Backfill with thiol-PEG.** After conjugation with miR-ssDNA conjugates, the surface of AuNRs was backfilled with thiolated PEG (2 kDa). Briefly, a suspension of AuNR-DNA-miR (500 µL, 0.5 nM) was incubated with thiol-PEG at 25 µM corresponding to a ratio of 1:50000 between AuNR and thiol-PEG. The reaction proceeded for 5 h at room temperature under orbital agitation. Then, the suspension was centrifuged (9000 g, 30 min) and resuspended in 10 mM phosphate pH 7.4 with 30 mM NaCl. The suspension was stored at 4º C.

**Cell culture.** HEK-293T transfected with a reporter vector were kindly offered by Dr. Ricardo Neves and Ana Lima. The reporter vector encodes EGFP conjugated to the targets of miR-302a-3p, and mCherry conjugated to the target of miR-155-5p. Cells were cultured in T-75 culture flasks at 37 ºC in a humidified atmosphere of 5% $CO_2$ in DMEM cell culture media containing 10% fetal bovine serum (FBS) and 0.5% penicillin-streptomycin. Cells were grown to 80-90% confluency before splitting and re-seeding 24 h each experiment.
OECs cells were differentiated from CD34+ cells isolated from mononuclear cells of umbilical cord blood samples as previously described [318].

**Cytotoxicity of miR-dsDNA-AuNR and cecropin-melittin**. To assess the cytotoxicity of AuNRs, HEK-293T cells were seeded on a 96 well plate ($12 \times 10^3$ cells/well), left to adhere for 24 h and then incubated with $dsDNA_{51.7}$-AuNR (50 µg $mL^{-1}$) without or with cecropin-melttin (5 µM and 10 µM) for 4 h in serum free medium. After incubation, cells were washed with PBS to remove non-internalized AuNRs. In some conditions, after incubation with AuNRs, cells were washed and irradiated with a 780 nm laser at 1.25 $Wcm^{-2}$ for 2 min. After 2 h in the incubator at 37 ºC, a subset of samples received a second laser stimulus for 2 min at 2 $Wcm^{-2}$.Then, cells were left in the incubator for 24 h and the ATP production was measured by a Celltiter-Glo Luminescent Cell Viability Assay (Promega) according to the manufacturer's instructions.

**Transfection of HEK293-T with miRNAs and DNA-miR conjugates and lipofectamine RNAimax.** The ability of miR-155 and miR-302a to induce the knockdown of mCherry and EGFP respectively, was evaluated via transfection with lipofectamine RNAimax. HEK-293-

T cells were seeded in a collagen coated 96 well plate (6500 cells/well) in DMEM (10% FBS, without antibiotics) 24 h before transfection. miR-155, miR-302a, ssDNA-miR-155 and ssDNA-miR-302a (35 µL, concentrations ranging from 0.05 to 5 nM) were complexed for 20 min with lipofectamine RNAimax diluted in DMEM (0.7µL of RNAimax in 35µL of DMEM). Then, each of the complexes was added to cells (20 µL/well) and incubated for 4 h or 24 h. Finally, cells were washed, new culture medium was added and cell fluorescence was monitored in a high-content fluorescence microscope (IN Cell 2200, GE Healthcare) each 12 h during 3 days.

**Activity of DNA-miR conjugates released from AuNRs.** The activity of miR-155 and miR-302a released from AuNR surface after irradiation was evaluated in HEK-293T cells seeded in a 96 well plate (6500 cells/well). In order to study the laser induced release and activity of miR-DNA conjugates, we used AuNRs hybridized with: I) miR-155 conjugated with ssDNA with a melting temperature of 51.7 ºC and II) miR-302a conjugated with ssDNA with a melting temperature of 68.9 ºC. Each suspension of miR-dsDNA-AuNR was irradiated and immediately centrifuged. Then the supernatant was complexed for 20 min with lipofectamine RNAimax (35 µL of supernatant complexed with 35 µL of RNAimax diluted 1:50 in DMEM) and 20 µL of this mixture was added to each well containing 100 µL of DMEM with 10 % FBS. After incubation, cells were kept in DMEM (10% FBS, 0.3 µg $mL^{-1}$ of Hoechst) and their fluorescence was monitored in a high-content fluorescence microscope (IN Cell 2200, GE Healthcare) each 12 h during 3 days.

**Confocal microscopy.** Images were acquired on a Zeiss LSM 710 confocal microscope (Carl Zeiss, Jena, Germany) using a 40x objective/ 1.4 numerical aperture oil PlanApochromat immersion lens. $DL_{488}$ and Lysotraker Green was detected using the 488 nm laser line of an Ar laser (25 mW nominal output) and an LP 505 filter. TRITC was detected using a 561 nm HeNe laser (1 mW) and an LP 560 filter. The pinhole aperture was set to 1 Airy unit. Live cells were imaged at 37 °C and 5% $CO_2$. Image acquisition and analyses were performed using the Zen Black 2012 software.

**Intracellular localization of miR-dsDNA-AuNR-TRITC.** Cells were seeded in an IBIDI 15 well slide (80 % confluency), left to adhere for 24 h and then incubated with miR-dsDNA-AuNR-TRITC (50 µg $mL^{-1}$) for 4 h without or with cecropin-melittin (5 or 10 µM) in DMEM (0.5% penstrep, without FBS). After incubation, cells were washed with medium to remove non-internalized AuNRs. Then, cells were incubated with LysoTracker® Green (100 nM) for 30 min to stain the endosomes and with Hoechst 33342 (0.3 µg $mL^{-1}$) to stain the nuclei. Cells were then observed under confocal microscope. Images were analysed in ImageJ and

the colocalization was determined by calculating the Manders' colocalization coefficient between AuNR-TRITC and Lysotracker green.

**Light-induced release of DNA-miR conjugates in HEK-293T**. HEK-293T cells were seeded in a 96 well plate (6500 cells/well), left to adhere for 24 h and then incubated with 50 μg $mL^{-1}$ of AuNR conjugated with miR-155-ssDNA or miR-302a-ssDNA. First, AuNRs modified with miR-155 or miR-302a were tested separately. A suspension of miR-dsDNA-AuNR was prepared in serum free DMEM. Before adding to cells, the suspension was mixed with cecropin-melittin peptide (final concentration of 5 or 10 μM). After 4 h incubation, the medium was replaced and cells were irradiated with a fibercoupled laser (780 nm) at 0.8, 1.25 or 2 $Wcm^{-2}$ for 2 min. Then, cells were incubated in DMEM (10% FBS, 0.5% penstrep and 0.3 μg $mL^{-1}$ of Hoechst 34580) and cell fluorescence was monitored in a high-content fluorescence microscope (IN Cell 2200, GE Healthcare).

**Light-induced release of DNA-miR conjugates in OECs**. OECs were seeded in a 96 well plate (10000 cells/well), left to adhere for 24 h and then incubated with 50 μg $mL^{-1}$ of AuNR conjugated with miR-155-ssDNA or miR-302a-ssDNA. A suspension of miR-dsDNA-AuNR was prepared in FBS free EGM-2. Before adding to cells, the suspension was mixed with cecropin-melittin peptide (final concentration of 5 μM). After 4 h incubation, the medium was replaced for EGM-2 and cells were irradiated with a fibercoupled laser (780 nm) at 1.25 for 2 min and 2 h later cells were subjected to a second stimulus of 2$Wcm^{-2}$ for 2 min.

**Transfection of OECs with miRNAs and lipofectamine RNAimax.** OECs were seeded in a 96 well plate (10000 cells/well), left to adhere for 24 h and then transfected with 50 nM of miR-155 and/or miR-302a or scramble using lipofectamine for 48 h. The complex was prepared in 10 μl of EMB-2 and added to cells on 90 μl of Gentamycin free EGM-2.

**Proliferation and Survival assays.** For the proliferation studies, 48 h after the AuNR incubation, cells were incubated with 1μg $mL^{-1}$ of Hoechst 34580 and nuclei were counted in a high-content fluorescence microscope (IN Cell 2200, GE Healthcare).
For the survival studies, following the proliferation analysis 48 h after the AuNR incubation, medium was replaced for EBM-2 and plates were covered with Breathe-Easy® sealing membranes (Sigma). Cells were kept in hypoxia (0,1% $O_2$) for 48 h, after which cells were incubated with 1μg $mL^{-1}$ of Hoechst 34580 and nuclei counts were performed in a high-content fluorescence microscope (IN Cell 2200, GE Healthcare). Cells treated with 50 ng $mL^{-1}$ of VEGF were used as positive control of the experiment.

**Transmission electron microscopy (TEM).** TEM was used to evaluate endosomal escape of AuNRs. Cells were seeded in a 24 well plate, left to adhere for 24 h to 90% of confluency and then incubated with miR-155-dsDNA-AuNR (50 μg $mL^{-1}$) with 10 μM cecropin-melittin or without cecropin-melittin. After 4 h incubation, the medium was replaced and cells were irradiated with a fibercoupled Roithner laser (780 nm) at 1.25 $Wcm^{-2}$ for 2 min. The culture medium was then removed without allowing the cells to dry. Cells were washed with PBS and then fixed with a fixative solution (2.5% gluteraldehyde and 2.0% paraformaldehyde in 0.1 mol $L^{-1}$ sodium cacodylate buffer with: 0.1 mol $L^{-1}$ sucrose, 50 mM KCl and 2.5 mM MgCl 1.25 mM CaC1, pH 7.4 for 1 h. Cells were postfixed for 1 h in a 2% osmium tetroxide solution containing 0.8% potassium ferrocyanide in 0.1M sodium cacodylate buffer. Samples were washed with distilled water and soaked overnight in aqueous 1% uranyl acetate at 4 ºC and then dehydrated in graded ethanols. Finally samples were embedded in a resin and observed in a Jeol JEM 1400 electron microscope. Images were acquired with a magnification between 20000X and 100000X. At least 30 images in each condition were analysed. In each image, the number of AuNRs in cell compartments (endosomes, lysosomes and cytosol) was counted and divided by the total number of AuNRs per image to obtain percentage of AuNRs per compartment.

# Chapter 4

## Conclusions

## 4.1 - General Conclusions

During the last years, drug delivery has experienced a transformative phase and has shifted to new paradigms. Combinatorial therapies have proven to be more efficacious in the treatment of several diseases and also in regenerative medicine, by exploiting synergistic effects between drugs[5]. Additionally, recent advances in the cellular biology area have opened the way to a new collection of therapeutic agents comprised by macromolecules, such as proteins and non-coding RNAs, namely siRNAs and microRNAs. Therapies based on the delivery of these biomolecules have great potential, since they are the main components and effectors involved in the regulation of cellular processes.

The multidrug delivery paradigm has been followed by the design of new delivery systems that can combine multiple drugs, normalizing pharmacokinetics and biodistribution. The potential of these systems for multidrug delivery is highly correlated with the possibility of delivering each drug in a controlled manner. This is a very important aspect, because a differential release of each molecule can mimic the spatio-temporal nature of biological processes. For example, analysis of the miRnome during cell differentiation or cells under external stresses shows that the expression of miRNAs changes overtime [319, 320]. Moreover, not only the precise delivery of small drugs[7] but also the orchestrated delivery of macromolecules, such as transcription factors[321], can have great impact in the final outcome of the therapy. This has driven research towards the development of nanocarriers with controllable drug release profiles. To achieve this, most systems rely on the control of the nanocarrier's degradation rates. More sophisticated systems, based on stimuli-responsive materials to attain a higher control over the release of each drug are still very scarce.

The current thesis focuses on the development of a new light-responsive nanocarrier for the delivery of more than one biomolecule with spatio-temporal control. The nanocarrier is constituted by a AuNR core with plasmon resonance band centered at 780 nm. In chapter II we demonstrated that two fluorescent proteins could be immobilized on the same AuNR and then be released sequentially by the application of different laser stimuli. This is the first work describing intracellular controlled release of two proteins from the same nanocarrier using NIR light. In our delivery system, although the release is achieved by a photothermal effect, a functional enzyme could be released from the AuNR without losing activity, which may be explained by the exponential decay of temperature with the distance from the AuNR surface[101]. Lower colocalization between AuNRs and fluorescent proteins and the diffuse signal in the cytoplasm indicated successful cytosolic delivery of proteins. Although AuNRs tend to be confined in endo/lysosomes, upon irradiation both AuNRs and proteins are able to reach the cytoplasm. It is possible that endosomal escape is mediated by photochemical generation of radicals rather than by photothermal effect[243]. Surprisingly, a laser stimulus with lower energy is able to disrupt the endosome membrane without inducing significant release of the protein bound to DNA with higher

melting temperature. Nonetheless, this fact has been crucial in achieving differential release of each molecule intracellularly.

In chapter III, the same principle was adopted for the intracellular delivery of two microRNAs. NIR light-triggered release of microRNAs or siRNAs has already been described with different systems, such has gold nanoshells [168] and UCNPs[95] . Independent release of two siRNAs was described in one system composed by two AuNRs with different aspect ratios that responded to two distinct wavelengths[140]. However, differences in nanoparticle size may have implications in uptake[21], and consequently in intracellular bioavailability of each siRNA. The development of nanocarriers for intracellular delivery of multiple RNAi therapeutics has been mainly focused on the control of siRNA stoichiometry in the nanocarrier[311, 313] and little has been done to tune the release of each molecule. In chapter III we demonstrate the high uptake and efficient endosomal escape of light-activatable nanocarriers conjugated with miRNAs. The sequential delivery of miR-155 and miR-302a by light activation was easily evaluated using a dual-reporter HEK-293T cell line. Laser irradiation at 1.25 $Wcm^{-2}$ induced the release of miR-155 and not miR-302a, decreasing mCherry fluorescence and not EGFP. An additional stimulus at 2 $Wcm^{-2}$ caused a decrease in EGFP fluorescence by the release of miR-302a. The system was also validated in cells with therapeutic relevance. For that puspose, we used OECs derived from human CD34+ cells isolated from cord blood. We demonstrated that multistep laser activation of AuNRs could be used to induce cell proliferation and survival in hypoxic conditions.

One of the innovative aspects of this work is related to the use of oligonucleotides for biomolecule conjugation and controlled release. Taking advantage of the photothermal effect of AuNRs, we designed ssDNAs with specific sequences and consequently with specific melting temperatures, to immobilize two different proteins or microRNAs and mediate a controlled release of each molecule through DNA dehybridization. Both ssDNAs immobilized directly on the gold surface via thiol-gold bonds have similar binding efficiencies. The sequences were designed with a poly(thymine) spacer to minimize non-specific interaction with the gold surface and allow an efficient hybridization. The length of the sequences might also be important to keep the active biomolecule at a certain distance from the gold surface protecting it from the photothermal effect. Moreover, the four ssDNA sequences used in this work were designed to achieve almost non-overlapping release profiles and highly specific hybridization. Consequently, negligible unspecific hybridization of protein-ssDNA conjugates was detected. This can lead to a higher control of the stoichiometry of the biomolecules immobilized on the AuNR surface.

A second innovative aspect of the present work was the development of a set of techniques/procedures to allow the evaluation of intracellular trafficking of light-triggerable formulations and their activation. For example, procedures for the fluorescent labelling of AuNRs, quantitative imaging, FRET analyses, TEM analyses, high-content imaging, among others. In addition, a dual reporter cell model has been used to monitor intracellularly two different miRNAs.

Previous studies have demonstrated the release of siRNAs from plasmonic NPs using fluorescence microscopy. The intracellular release was evaluated by the dequenching of fluorescent siRNAs[168] which was assessed by fluorescence microscopy or flow cytometry. SiRNA activity assays were mainly based on silencing of one specific gene[32] or knockdown of a single protein reporter, usually GFP [91, 168]. Besides this, assessment of apoptosis and proliferation[32, 143] have been used as functional readouts of siRNA delivery. Nevertheless, most works do not provide information about the amount of nanocarriers that reach the cytoplasm after photo-activation and do not make a correlation between quantification of endosomal escape and the laser power used for light-triggered release.

A third innovative aspect of the current work is the demonstration that light and some peptides may facilitate endolysosomal escape of the nanocarriers and the biomolecules. This aspect is of utmost importance in drug delivery[322] and also affects temporal control. Although previous studies have shown the escape of nanocarriers after laser activation[122, 238], the current study has shown for the first time the effect of power in such escape. In addition, our work demonstrates for the first time the effect of an antimicrobial peptide for the enhanced intracellular accumulation of nanocarriers and endosomal escape. Low uptake levels and also endosomal sequestration of siRNAs or miRNAs may hamper significantly their biological effect, since they need to reach the cytoplasm to start RNAi mechanism. Different approaches have been reported to increase the uptake of siRNAs immobilized into plasmonic gold NPs. The group of Naomi Halas developed a gold nanoshell coated with polylysine to complex siRNA and promote uptake[91]. Other groups have used peptides, such as TAT[168] or RPARPAR peptide[143] to coat nanoshells. These strategies increased endocytosis but not endosomal escape. Endosomal escape was then promoted by irradiation with femtosecond laser pulses[143, 168] or CW irradiation at 2.5Wcm$^{-2}$ [91]. Another study reported a “bomb-like” NP to escape the endosomes and deliver miRNA[306]. The formulation was formed by thermo-responsive Pluronic PF127 and ammonium bicarbonate that could be thermally triggered to release carbon dioxide and ammonia gases leading to rupture of the endosome. In this thesis, we used cecropin-melittin, a cationic amphiphilic antimicrobial peptide. A chimeric conjugate of this peptide has already been used for endosomal escape[212]. In this work it has been applied to increase uptake of AuNRs, as well. Co-incubation of AuNRs with cecropin-melittin caused a significant increase in cell uptake as confirmed by ICP-MS analyses (63-fold higher when compared to AuNRs alone). TEM images confirmed the important role of cecropin-melittin in endosomal escape. Although AuNRs could be observed in endosomes, the percentage of AuNRs in lysosomes was significantly reduced when cecropin-melittin was used. This way, miRNAs carried by AuNRs are not subjected to endosomal acidification and lysosomal degradation. In agreement to what was observed with AuNR conjugated with proteins (Chapter II), laser irradiation also induced endosomal escape of AuNR conjugated with miRNAs. High uptake and efficient endosomal escape allowed cytosolic delivery of higher concentration of microRNAs enough to

induce protein knockdown. The sequential delivery of miR-155 and miR-302a was easily assessed using a dual-reporter HEK-293T cell line. Laser irradiation at 1.25 $Wcm^{-2}$ induced the release of miR-155 and not miR-302a, decreasing mCherry fluorescence and not EGFP. An additional stimulus at 2 $Wcm^{-2}$ caused a decrease in EGFP fluorescence by the release of miR-302a. The system was also validated in cells with therapeutic relevance. For that, we used OECs derived from human CD34+ cells isolated from cord blood. We demonstrated that multistep laser activation of AuNRs could be used to induce cell proliferation and survival in hypoxic conditions.

We envision that the plasmonic nanocarrier developed in the current work might have unprecedented potential for modulation of cell activity, which might be beneficial in many applications. For example, in cell reprogramming it was shown that sequential expression of transcription factors can surpass the simultaneous expression, leading to better results.[323] The sequential delivery of reprogramming factors can also be used to mimic the natural differentiation process, which is characterized by a coordinated and sequential expression of transcription factors[324, 325]. A system for controlled delivery of microRNAs, which are powerful molecules for modulation of cell activity, has great potential to be applied in the treatment of different diseases and in regenerative medicine. The spatial and temporal patterns of miRNA expression play an important role in several physiological and pathological processes, including tumorigenesis[326], cell proliferation[327], cell differentiation[328], angiogenesis[317], etc. In the context of cell reprogramming induced by ectopic expression of transcription factors, a study revealed an ordered and sequential activation of miRNAs, correlating these finding with higher reprogramming efficiency.[329] Likewise, another study reported unique miRNA signatures among reprogramming intermediates, which contributes to the transition from early phase stochastic to later phase deterministic behaviour in cell reprogramming.[330]

## 4.2 - Perspectives and Future work

We predict that low nanoparticle uptake might be one of the major problems when testing our nanoformulation *in vivo*. *In vitro* studies have shown that co-incubation with cecropin-melittin was beneficial for increased uptake and endosomal escape. Nevertheless, the immobilization of this peptide on the nanocarrier, rather than its administration in soluble form, seems to be more suitable for biomedical applications, avoiding potential side effects and toxicity.

Regarding protein delivery, we will use the nanocarrier for the delivery of proteins that could have an impact in cell behaviour, such as transcription factors. Importantly, we believe that the versatility of this nanoformulation could be helpful to overcome some of the issues that may arise in the future. For example, although we have demonstrated that a functional enzyme remained

active after conjugation with ssDNA and further laser-induced release, that might not be true for other proteins. To circumvent this issue, the immobilization of synthetic mRNAs encoding specific proteins on the AuNR should be considered. Chemically modified mRNAs are single stranded nucleic acids that can be immobilized through hybridization with complementary DNA strands bound to the AuNR surface, thus following the same delivery principle demonstrated in this work.

Future experiments are required to evaluate the effect of the sequential delivery of two miRNAs in OECs, by verifying the expression of markers for neo-angiogenesis at gene and protein level. The transplantation of OECs exposed to our nanoformulation should be performed in an *in vivo* model to promote neovascularization. A murine dermal excisional wound model could be used to evaluate different parameters, like survival of transplanted cells, new capillary formation and wound re-epithelization[331]. After internalization of AuNRs, cells will be transplanted into the wound, where a first light stimulus will be applied to promote release of miR-155 and consequently enhance cell survival. Then, a higher energy stimulus will trigger release of miR-302a to increase cell proliferation. The impact of the time between each activation will be one important aspect to study *in vivo*. The rate of wound closure will be assessed by measuring the area of the wound at different time points along a certain period (10-12 days), after which animals will be sacrificed and tissue biopsies will be taken for genetic analysis by RT-PCR and for histological analysis by immunohistochemistry. Expression of cytokines and chemokines will be evaluated by commercially available ELISA or multiplex kits.

While the experimental work for this thesis was in progress, other promising application for our system has emerged. Recently, CRISPR/Cas9 system has shown extraordinary potential in precise genome editing.[332] The CRISPR associated protein Cas9 is an endonuclease that uses a guide sequence within an RNA duplex, tracrRNA:crRNA, to form base pairs with DNA target sequences, enabling Cas9 to introduce a site-specific double-strand break in the DNA. We have already some preliminary data confirming that mRNA encoding Cas9 and tracrRNA can be immobilized via hybridization on AuNRs. Future studies will be performed in different cell models to evaluate the potential of our technology for spatio-temporal controlled gene editing.

# References


1. Leader, B., Baca, Q.J. & Golan, D.E. Protein therapeutics: a summary and pharmacological classification. *Nat Rev Drug Discov* **7**, 21-39 (2008).
2. Bartel, D.P. MicroRNAs: Genomics, Biogenesis, Mechanism, and Function. *Cell* **116**, 281-297 (2004).
3. Grimm, D. & Kay, M.A. Combinatorial RNAi: A Winning Strategy for the Race Against Evolving Targets[quest]. *Mol Ther* **15**, 878-888 (2007).
4. Hu, C.-M.J. & Zhang, L. Nanoparticle-based combination therapy toward overcoming drug resistance in cancer. *Biochemical Pharmacology* **83**, 1104-1111 (2012).
5. Katselou, M.G., Matralis, A.N. & Kourounakis, A.P. Multi-Target Drug Design Approaches for Multifactorial Diseases: From Neurodegenerative to Cardiovascular Applications. *Current Medicinal Chemistry* **21**, 2743-2787 (2014).
6. He, C., Tang, Z., Tian, H. & Chen, X. Co-delivery of chemotherapeutics and proteins for synergistic therapy. *Advanced Drug Delivery Reviews* **98**, 64-76 (2016).
7. Li, L., Sun, W., Zhang, Z. & Huang, Y. Time-staggered delivery of docetaxel and H1-S6A,F8A peptide for sequential dual-strike chemotherapy through tumor priming and nuclear targeting. *Journal of Controlled Release* **232**, 62-74 (2016).
8. Chen, F.-M., Zhang, M. & Wu, Z.-F. Toward delivery of multiple growth factors in tissue engineering. *Biomaterials* **31**, 6279-6308 (2010).
9. Graf, T. & Enver, T. Forcing cells to change lineages. *Nature* **462**, 587-594 (2009).
10. Zhu, S., Nih, L., Carmichael, S.T., Lu, Y. & Segura, T. Enzyme-Responsive Delivery of Multiple Proteins with Spatiotemporal Control. *Advanced Materials* **27**, 3620-3625 (2015).
11. Esteller, M. Non-coding RNAs in human disease. *Nat Rev Genet* **12**, 861-874 (2011).
12. Shibata, M.A., Morimoto, J., Shibata, E. & Otsuki, Y. Combination therapy with short interfering RNA vectors against VEGF-C and VEGF-A suppresses lymph node and lung metastasis in a mouse immunocompetent mammary cancer model. *Cancer Gene Ther* **15**, 776-786 (2008).
13. Tai, W., Qin, B. & Cheng, K. Inhibition of Breast Cancer Cell Growth and Invasiveness by Dual Silencing of HER-2 and VEGF. *Molecular Pharmaceutics* **7**, 543-556 (2010).
14. Liu, Y.P. et al. Combinatorial RNAi Against HIV-1 Using Extended Short Hairpin RNAs. *Mol Ther* **17**, 1712-1723 (2009).

15. Chandra, P.K. et al. Inhibition of Hepatitis C Virus Replication by Intracellular Delivery of Multiple siRNAs by Nanosomes. *Mol Ther* **20**, 1724-1736 (2012).
16. Ma, L., Kohli, M. & Smith, A. Nanoparticles for Combination Drug Therapy. *ACS Nano* **7**, 9518-9525 (2013).
17. Feynman, R. There's Plenty of Room at the Bottom. *Engineering and Science* **23**, 22-36 (1960).
18. Wagner, V., Dullaart, A., Bock, A.-K. & Zweck, A. The emerging nanomedicine landscape. *Nat Biotech* **24**, 1211-1217 (2006).
19. Gregoriadis, G., Leathwood, P.D. & Ryman, B.E. Enzyme entrapment in liposomes. *FEBS Letters* **14**, 95-99 (1971).
20. Bobo, D., Robinson, K.J., Islam, J., Thurecht, K.J. & Corrie, S.R. Nanoparticle-Based Medicines: A Review of FDA-Approved Materials and Clinical Trials to Date. *Pharmaceutical Research* **33**, 2373-2387 (2016).
21. Chithrani, B.D., Ghazani, A.A. & Chan, W.C.W. Determining the Size and Shape Dependence of Gold Nanoparticle Uptake into Mammalian Cells. *Nano Letters* **6**, 662-668 (2006).
22. Florez, L. et al. How Shape Influences Uptake: Interactions of Anisotropic Polymer Nanoparticles and Human Mesenchymal Stem Cells. *Small* **8**, 2222-2230 (2012).
23. Huang, X., Teng, X., Chen, D., Tang, F. & He, J. The effect of the shape of mesoporous silica nanoparticles on cellular uptake and cell function. *Biomaterials* **31**, 438-448 (2010).
24. Huang, X. et al. The Shape Effect of Mesoporous Silica Nanoparticles on Biodistribution, Clearance, and Biocompatibility in Vivo. *ACS Nano* **5**, 5390-5399 (2011).
25. Hoshyar, N., Gray, S., Han, H. & Bao, G. The effect of nanoparticle size on in vivo pharmacokinetics and cellular interaction. *Nanomedicine* **11**, 673-692 (2016).
26. Njoki, P.N. et al. Size Correlation of Optical and Spectroscopic Properties for Gold Nanoparticles. *The Journal of Physical Chemistry C* **111**, 14664-14669 (2007).
27. Boto, C. Doctoral Thesis - Leukemia Cells Modulation By Light-Activatable Nanoparticles. *University of Coimbra* (2014).
28. Sanvicens, N. & Marco, M.P. Multifunctional nanoparticles – properties and prospects for their use in human medicine. *Trends in Biotechnology* **26**, 425-433 (2008).
29. Pacardo, D.B., Ligler, F.S. & Gu, Z. Programmable nanomedicine: synergistic and sequential drug delivery systems. *Nanoscale* **7**, 3381-3391 (2015).
30. Cheng, D., Cao, N., Chen, J., Yu, X. & Shuai, X. Multifunctional nanocarrier mediated co-delivery of doxorubicin and siRNA for synergistic enhancement of glioma apoptosis in rat. *Biomaterials* **33**, 1170-1179 (2012).

31. Chen, W. et al. Co-Delivery of Doxorubicin and siRNA with Reduction and pH Dually Sensitive Nanocarrier for Synergistic Cancer Therapy. *Small* **10**, 2678-2687 (2014).
32. Shen, J. et al. Multifunctional Gold Nanorods for siRNA Gene Silencing and Photothermal Therapy. *Advanced Healthcare Materials* **3**, 1629-1637 (2014).
33. Noh, M.S. et al. Target-specific near-IR induced drug release and photothermal therapy with accumulated Au/Ag hollow nanoshells on pulmonary cancer cell membranes. *Biomaterials* **45**, 81-92 (2015).
34. Ren, F. et al. Gold Nanorods Carrying Paclitaxel for Photothermal-Chemotherapy of Cancer. *Bioconjugate Chemistry* **24**, 376-386 (2013).
35. Jeon, S.Y. et al. Co-delivery of Cbfa-1-targeting siRNA and SOX9 protein using PLGA nanoparticles to induce chondrogenesis of human mesenchymal stem cells. *Biomaterials* **35**, 8236-8248 (2014).
36. Ren, Y. et al. Sequential co-delivery of miR-21 inhibitor followed by burst release doxorubicin using NIR-responsive hollow gold nanoparticle to enhance anticancer efficacy. *Journal of Controlled Release* **228**, 74-86 (2016).
37. Song, J. et al. Sequential Drug Release and Enhanced Photothermal and Photoacoustic Effect of Hybrid Reduced Graphene Oxide-Loaded Ultrasmall Gold Nanorod Vesicles for Cancer Therapy. *ACS Nano* **9**, 9199-9209 (2015).
38. Hu, Y. et al. Sequential delivery of therapeutic agents using a rationally designed disulfide-linked glycolipid-like nanocarrier. (2016).
39. Jiang, T., Mo, R., Bellotti, A., Zhou, J. & Gu, Z. Gel–Liposome-Mediated Co-Delivery of Anticancer Membrane-Associated Proteins and Small-Molecule Drugs for Enhanced Therapeutic Efficacy. *Advanced Functional Materials* **24**, 2295-2304 (2014).
40. Xiao, D. et al. A Dual-Responsive Mesoporous Silica Nanoparticle for Tumor-Triggered Targeting Drug Delivery. *Small* **10**, 591-598 (2014).
41. Zhang, P. et al. Near Infrared-Guided Smart Nanocarriers for MicroRNA-Controlled Release of Doxorubicin/siRNA with Intracellular ATP as Fuel. *ACS Nano* **10**, 3637-3647 (2016).
42. Yoon, H.Y. et al. Glycol chitosan nanoparticles as specialized cancer therapeutic vehicles: Sequential delivery of doxorubicin and Bcl-2 siRNA. *Scientific Reports* **4**, 6878 (2014).
43. Stirland, D.L., Matsumoto, Y., Toh, K., Kataoka, K. & Bae, Y.H. Analyzing spatiotemporal distribution of uniquely fluorescent nanoparticles in xenograft tumors. *Journal of Controlled Release* **227**, 38-44 (2016).
44. Tardi, P. et al. In vivo maintenance of synergistic cytarabine:daunorubicin ratios greatly enhances therapeutic efficacy. *Leukemia Research* **33**, 129-139 (2009).

45. Yonet-Tanyeri, N. et al. The spatiotemporal control of erosion and molecular release from micropatterned poly(ethylene glycol)-based hydrogel. *Biomaterials* **34**, 8416-8423 (2013).
46. Aryal, S., Hu, C.-M.J. & Zhang, L. Combinatorial Drug Conjugation Enables Nanoparticle Dual-Drug Delivery. *Small* **6**, 1442-1448 (2010).
47. Wang, Z. & Ho, P.C. A nanocapsular combinatorial sequential drug delivery system for antiangiogenesis and anticancer activities. *Biomaterials* **31**, 7115-7123 (2010).
48. Sengupta, S. et al. Temporal targeting of tumour cells and neovasculature with a nanoscale delivery system. *Nature* **436**, 568-572 (2005).
49. Li, D. et al. Synergistic Enhancement of Lung Cancer Therapy Through Nanocarrier-Mediated Sequential Delivery of Superantigen and Tyrosin Kinase Inhibitor. *Advanced Functional Materials* **24**, 5482-5492 (2014).
50. Saiyin, W. et al. Sequential Release of Autophagy Inhibitor and Chemotherapeutic Drug with Polymeric Delivery System for Oral Squamous Cell Carcinoma Therapy. *Molecular Pharmaceutics* **11**, 1662-1675 (2014).
51. Fan, L. et al. Multifunctional all-in-one drug delivery systems for tumor targeting and sequential release of three different anti-tumor drugs. *Biomaterials* **76**, 399-407 (2016).
52. Acton, A.L. et al. Janus PEG-Based Dendrimers for Use in Combination Therapy: Controlled Multi-Drug Loading and Sequential Release. *Biomacromolecules* **14**, 564-574 (2013).
53. Liao, L. et al. A Convergent Synthetic Platform for Single-Nanoparticle Combination Cancer Therapy: Ratiometric Loading and Controlled Release of Cisplatin, Doxorubicin, and Camptothecin. *Journal of the American Chemical Society* **136**, 5896-5899 (2014).
54. Carregal-Romero, S. et al. NIR-light triggered delivery of macromolecules into the cytosol. *Journal of Controlled Release* **159**, 120-127 (2012).
55. Azagarsamy, M.A. & Anseth, K.S. Wavelength-Controlled Photocleavage for the Orthogonal and Sequential Release of Multiple Proteins. *Angewandte Chemie International Edition* **52**, 13803-13807 (2013).
56. Timko, B.P., Dvir, T. & Kohane, D.S. Remotely Triggerable Drug Delivery Systems. *Advanced Materials* **22**, 4925-4943 (2010).
57. Mura, S., Nicolas, J. & Couvreur, P. Stimuli-responsive nanocarriers for drug delivery. *Nat Mater* **12**, 991-1003 (2013).
58. Gao, W., Chan, J.M. & Farokhzad, O.C. pH-Responsive Nanoparticles for Drug Delivery. *Molecular Pharmaceutics* **7**, 1913-1920 (2010).
59. Luo, Z. et al. Mesoporous Silica Nanoparticles End-Capped with Collagen: Redox-Responsive Nanoreservoirs for Targeted Drug Delivery. *Angewandte Chemie International Edition* **50**, 640-643 (2011).

60. Wang, Y., Chen, P. & Shen, J. The development and characterization of a glutathione-sensitive cross-linked polyethylenimine gene vector. *Biomaterials* **27**, 5292-5298 (2006).
61. Derfus, A.M. et al. Remotely Triggered Release from Magnetic Nanoparticles. *Advanced Materials* **19**, 3932-3936 (2007).
62. Sirsi, S.R. & Borden, M.A. State-of-the-art materials for ultrasound-triggered drug delivery. *Advanced Drug Delivery Reviews* **72**, 3-14 (2014).
63. Kneidl, B., Peller, M., Winter, G., Lindner, L.H. & Hossann, M. Thermosensitive liposomal drug delivery systems: state of the art review. *International Journal of Nanomedicine* **9**, 4387-4398 (2014).
64. Alvarez-Lorenzo, C., Bromberg, L. & Concheiro, A. Light-sensitive Intelligent Drug Delivery Systems†. *Photochemistry and Photobiology* **85**, 848-860 (2009).
65. Rwei, A.Y., Wang, W. & Kohane, D.S. Photoresponsive nanoparticles for drug delivery. *Nano Today* **10**, 451-467 (2015).
66. Huang, Z. A Review of Progress in Clinical Photodynamic Therapy. *Technology in cancer research & treatment* **4**, 283-293 (2005).
67. Jochum, F.D. & Theato, P. Temperature- and light-responsive smart polymer materials. *Chemical Society Reviews* **42**, 7468-7483 (2013).
68. Huang, Y., Dong, R., Zhu, X. & Yan, D. Photo-responsive polymeric micelles. *Soft Matter* **10**, 6121-6138 (2014).
69. Ramakrishnan, P., Maclean, M., MacGregor, S.J., Anderson, J.G. & Grant, M.H. Cytotoxic responses to 405 nm light exposure in mammalian and bacterial cells: Involvement of reactive oxygen species. *Toxicology in Vitro* **33**, 54-62 (2016).
70. Glickman, R.D. Phototoxicity to the Retina: Mechanisms of Damage. *International Journal of Toxicology* **21**, 473-490 (2002).
71. Henderson, T.A. & Morries, L.D. Near-infrared photonic energy penetration: can infrared phototherapy effectively reach the human brain? *Neuropsychiatric Disease and Treatment* **11**, 2191-2208 (2015).
72. Zhao, H., Sterner, E.S., Coughlin, E.B. & Theato, P. o-Nitrobenzyl Alcohol Derivatives: Opportunities in Polymer and Materials Science. *Macromolecules* **45**, 1723-1736 (2012).
73. Schmidt, R., Geissler, D., Hagen, V. & Bendig, J. Mechanism of Photocleavage of (Coumarin-4-yl)methyl Esters. *The Journal of Physical Chemistry A* **111**, 5768-5774 (2007).
74. Casey, J.P., Blidner, R.A. & Monroe, W.T. Caged siRNAs for Spatiotemporal Control of Gene Silencing. *Molecular Pharmaceutics* **6**, 669-685 (2009).
75. Xie, Z. et al. A Novel Biodegradable and Light-Breakable Diblock Copolymer Micelle for Drug Delivery. *Advanced Engineering Materials* **11**, B7-B11 (2009).

76. Bandara, H.M.D. & Burdette, S.C. Photoisomerization in different classes of azobenzene. *Chemical Society Reviews* **41**, 1809-1825 (2012).

77. Wang, G., Tong, X. & Zhao, Y. Preparation of Azobenzene-Containing Amphiphilic Diblock Copolymers for Light-Responsive Micellar Aggregates. *Macromolecules* **37**, 8911-8917 (2004).

78. Yuan, Q. et al. Photon-Manipulated Drug Release from a Mesoporous Nanocontainer Controlled by Azobenzene-Modified Nucleic Acid. *ACS Nano* **6**, 6337-6344 (2012).

79. Vleggaar, J.J.M. et al. Photoinduced Wolff-Rearrangement of 2-Diazo-1-naphthoquinones: Evidence for the Participation of a Carbene Intermediate. *Journal of the American Chemical Society* **116**, 11754-11763 (1994).

80. Chen, C. et al. Photo-responsive, biocompatible polymeric micelles self-assembled from hyperbranched polyphosphate-based polymers. *Polymer Chemistry* **2**, 1389-1397 (2011).

81. Lee, J., Park, J., Singha, K. & Kim, W.J. Mesoporous silica nanoparticle facilitated drug release through cascade photosensitizer activation and cleavage of singlet oxygen sensitive linker. *Chemical Communications* **49**, 1545-1547 (2013).

82. Yang, G., Sun, X., Liu, J., Feng, L. & Liu, Z. Light-Responsive, Singlet-Oxygen-Triggered On-Demand Drug Release from Photosensitizer-Doped Mesoporous Silica Nanorods for Cancer Combination Therapy. *Advanced Functional Materials* **26**, 4722-4732 (2016).

83. Saravanakumar, G., Lee, J., Kim, J. & Kim, W.J. Visible light-induced singlet oxygen-mediated intracellular disassembly of polymeric micelles co-loaded with a photosensitizer and an anticancer drug for enhanced photodynamic therapy. *Chemical Communications* **51**, 9995-9998 (2015).

84. Fairbanks, B.D., Singh, S.P., Bowman, C.N. & Anseth, K.S. Photodegradable, Photoadaptable Hydrogels via Radical-Mediated Disulfide Fragmentation Reaction. *Macromolecules* **44**, 2444-2450 (2011).

85. Goodwin, A.P., Mynar, J.L., Ma, Y., Fleming, G.R. & Fréchet, J.M.J. Synthetic Micelle Sensitive to IR Light via a Two-Photon Process. *Journal of the American Chemical Society* **127**, 9952-9953 (2005).

86. Gug, S. et al. Photolabile Glutamate Protecting Group with High One- and Two-Photon Uncaging Efficiencies. *ChemBioChem* **9**, 1303-1307 (2008).

87. Bort, G., Gallavardin, T., Ogden, D. & Dalko, P.I. From One-Photon to Two-Photon Probes: "Caged" Compounds, Actuators, and Photoswitches. *Angewandte Chemie International Edition* **52**, 4526-4537 (2013).

88. Furuta, T. et al. Brominated 7-hydroxycoumarin-4-ylmethyls: Photolabile protecting groups with biologically useful cross-sections for two photon photolysis. *Proceedings of the National Academy of Sciences* **96**, 1193-1200 (1999).

89. Babin, J. et al. A New Two-Photon-Sensitive Block Copolymer Nanocarrier. *Angewandte Chemie International Edition* **48**, 3329-3332 (2009).

90. Yan, B., Boyer, J.-C., Branda, N.R. & Zhao, Y. Near-Infrared Light-Triggered Dissociation of Block Copolymer Micelles Using Upconverting Nanoparticles. *Journal of the American Chemical Society* **133**, 19714-19717 (2011).

91. Huschka, R. et al. Gene Silencing by Gold Nanoshell-Mediated Delivery and Laser-Triggered Release of Antisense Oligonucleotide and siRNA. *ACS Nano* **6**, 7681-7691 (2012).

92. Wang, F. & Liu, X. Recent advances in the chemistry of lanthanide-doped upconversion nanocrystals. *Chemical Society Reviews* **38**, 976-989 (2009).

93. Liu, J., Bu, W., Pan, L. & Shi, J. NIR-Triggered Anticancer Drug Delivery by Upconverting Nanoparticles with Integrated Azobenzene-Modified Mesoporous Silica. *Angewandte Chemie International Edition* **52**, 4375-4379 (2013).

94. Viger, M.L., Grossman, M., Fomina, N. & Almutairi, A. Low Power Upconverted Near-IR Light for Efficient Polymeric Nanoparticle Degradation and Cargo Release. *Advanced Materials* **25**, 3733-3738 (2013).

95. Yang, Y., Liu, F., Liu, X. & Xing, B. NIR light controlled photorelease of siRNA and its targeted intracellular delivery based on upconversion nanoparticles. *Nanoscale* **5**, 231-238 (2013).

96. Moon, H.K., Lee, S.H. & Choi, H.C. In Vivo Near-Infrared Mediated Tumor Destruction by Photothermal Effect of Carbon Nanotubes. *ACS Nano* **3**, 3707-3713 (2009).

97. Feng, L., Wu, L. & Qu, X. New Horizons for Diagnostics and Therapeutic Applications of Graphene and Graphene Oxide. *Advanced Materials* **25**, 168-186 (2013).

98. Jain, P.K., Huang, X., El-Sayed, I.H. & El-Sayed, M.A. Noble Metals on the Nanoscale: Optical and Photothermal Properties and Some Applications in Imaging, Sensing, Biology, and Medicine. *Accounts of Chemical Research* **41**, 1578-1586 (2008).

99. Orendorff, C.J. & Murphy, C.J. Quantitation of Metal Content in the Silver-Assisted Growth of Gold Nanorods. *The Journal of Physical Chemistry B* **110**, 3990-3994 (2006).

100. Jain, P.K., Lee, K.S., El-Sayed, I.H. & El-Sayed, M.A. Calculated Absorption and Scattering Properties of Gold Nanoparticles of Different Size, Shape, and Composition: Applications in Biological Imaging and Biomedicine. *The Journal of Physical Chemistry B* **110**, 7238-7248 (2006).

101. Maity, S. et al. Spatial temperature mapping within polymer nanocomposites undergoing ultrafast photothermal heating via gold nanorods. *Nanoscale* **6**, 15236-15247 (2014).

102. Yavuz, M.S. et al. Gold nanocages covered by smart polymers for controlled release with near-infrared light. *Nat Mater* **8**, 935-939 (2009).

103. Huschka, R. et al. Light-Induced Release of DNA from Gold Nanoparticles: Nanoshells and Nanorods. *Journal of the American Chemical Society* **133**, 12247-12255 (2011).

104. Agarwal, A., Mackey, M.A., El-Sayed, M.A. & Bellamkonda, R.V. Remote Triggered Release of Doxorubicin in Tumors by Synergistic Application of Thermosensitive Liposomes and Gold Nanorods. *ACS Nano* **5**, 4919-4926 (2011).

105. Forbes, N., Pallaoro, A., Reich, N.O. & Zasadzinski, J.A. Rapid, Reversible Release from Thermosensitive Liposomes Triggered by Near-Infra-Red Light. *Particle & Particle Systems Characterization* **31**, 1158-1167 (2014).

106. Kawano, T., Niidome, Y., Mori, T., Katayama, Y. & Niidome, T. PNIPAM Gel-Coated Gold Nanorods for Targeted Delivery Responding to a Near-Infrared Laser. *Bioconjugate Chemistry* **20**, 209-212 (2009).

107. Zhang, Z. et al. Near Infrared Laser-Induced Targeted Cancer Therapy Using Thermoresponsive Polymer Encapsulated Gold Nanorods. *Journal of the American Chemical Society* **136**, 7317-7326 (2014).

108. Kurapati, R. & Raichur, A.M. Near-infrared light-responsive graphene oxide composite multilayer capsules: a novel route for remote controlled drug delivery. *Chemical Communications* **49**, 734-736 (2013).

109. Link, S., Burda, C., Mohamed, M.B., Nikoobakht, B. & El-Sayed, M.A. Laser Photothermal Melting and Fragmentation of Gold Nanorods: Energy and Laser Pulse-Width Dependence. *The Journal of Physical Chemistry A* **103**, 1165-1170 (1999).

110. Link, S., Burda, C., Nikoobakht, B. & El-Sayed, M.A. Laser-Induced Shape Changes of Colloidal Gold Nanorods Using Femtosecond and Nanosecond Laser Pulses. *The Journal of Physical Chemistry B* **104**, 6152-6163 (2000).

111. Ryther, R.C.C., Flynt, A.S., Phillips, J.A. & Patton, J.G. siRNA therapeutics: big potential from small RNAs. *Gene Ther* **12**, 5-11 (2004).

112. Krejsa, C., Rogge, M. & Sadee, W. Protein therapeutics: new applications for pharmacogenetics. *Nat Rev Drug Discov* **5**, 507-521 (2006).

113. Rosenbaugh, E.G. et al. The Attenuation of Central Angiotensin II-dependent Pressor Response and Intra-neuronal Signaling by Intracarotid Injection of Nanoformulated Copper/Zinc Superoxide Dismutase. *Biomaterials* **31**, 5218-5226 (2010).

114. Chul Cho, K. et al. Folate receptor-mediated intracellular delivery of recombinant caspase-3 for inducing apoptosis. *Journal of Controlled Release* **108**, 121-131 (2005).

115. Wang, M., Alberti, K., Sun, S., Arellano, C.L. & Xu, Q. Combinatorially Designed Lipid-like Nanoparticles for Intracellular Delivery of Cytotoxic Protein for Cancer Therapy. *Angewandte Chemie* **126**, 2937-2942 (2014).

116. Takahashi, K. & Yamanaka, S. Induction of Pluripotent Stem Cells from Mouse Embryonic and Adult Fibroblast Cultures by Defined Factors. *Cell* **126**, 663-676 (2006).

117. Ieda, M. et al. Direct Reprogramming of Fibroblasts into Functional Cardiomyocytes by Defined Factors. *Cell* **142**, 375-386 (2010).

118. Gu, Z., Biswas, A., Zhao, M. & Tang, Y. Tailoring nanocarriers for intracellular protein delivery. *Chemical Society Reviews* **40**, 3638-3655 (2011).

119. D'Astolfo, Diego S. et al. Efficient Intracellular Delivery of Native Proteins. *Cell* **161**, 674-690 (2015).

120. Erazo-Oliveras, A. et al. Protein delivery into live cells by incubation with an endosomolytic agent. *Nat Methods* **11**, 861-867 (2014).

121. Lu, Y., Sun, W. & Gu, Z. Stimuli-responsive nanomaterials for therapeutic protein delivery. *Journal of Controlled Release* **194**, 1-19 (2014).

122. Morales, D.P. et al. Targeted Intracellular Delivery of Proteins with Spatial and Temporal Control. *Molecular Pharmaceutics* **12**, 600-609 (2015).

123. Azagarsamy, M.A., Alge, D.L., Radhakrishnan, S.J., Tibbitt, M.W. & Anseth, K.S. Photocontrolled Nanoparticles for On-Demand Release of Proteins. *Biomacromolecules* **13**, 2219-2224 (2012).

124. Jin, Q., Cai, T., Wang, Y., Wang, H. & Ji, J. Light-Responsive Polyion Complex Micelles with Switchable Surface Charge for Efficient Protein Delivery. *ACS Macro Letters* **3**, 679-683 (2014).

125. Zhou, L. et al. DNA-mediated Construction of Hollow Upconversion Nanoparticles for Protein Harvesting and Near-Infrared Light Triggered Release. *Advanced Materials* **26**, 2424-2430 (2014).

126. Lam, J.K.W., Chow, M.Y.T., Zhang, Y. & Leung, S.W.S. siRNA Versus miRNA as Therapeutics for Gene Silencing. *Mol Ther Nucleic Acids* **4**, e252 (2015).

127. Slivac, I., Guay, D., Mangion, M., Champeil, J. & Gaillet, B. Non-viral nucleic acid delivery methods. *Expert Opinion on Biological Therapy*, 1-14 (2016).

128. Deleavey, G.F., Watts, J.K. & Damha, M.J. in Current Protocols in Nucleic Acid Chemistry (John Wiley & Sons, Inc., 2001).

129. Jeong, J.H., Mok, H., Oh, Y.-K. & Park, T.G. siRNA Conjugate Delivery Systems. *Bioconjugate Chemistry* **20**, 5-14 (2009).

130. Tan, S.J., Kiatwuthinon, P., Roh, Y.H., Kahn, J.S. & Luo, D. Engineering Nanocarriers for siRNA Delivery. *Small* **7**, 841-856 (2011).

131. Shim, M.S. & Kwon, Y.J. Stimuli-responsive polymers and nanomaterials for gene delivery and imaging applications. *Advanced Drug Delivery Reviews* **64**, 1046-1059 (2012).

132. Liu, Y.-C. et al. Photo-Assisted Gene Delivery Using Light-Responsive Catanionic Vesicles. *Langmuir* **25**, 5713-5724 (2009).

133. Han, G. et al. Light-Regulated Release of DNA and Its Delivery to Nuclei by Means of Photolabile Gold Nanoparticles. *Angewandte Chemie* **118**, 3237-3241 (2006).

134. Foster, A.A., Greco, C.T., Green, M.D., Epps, T.H. & Sullivan, M.O. Light-Mediated Activation of siRNA Release in Diblock Copolymer Assemblies for Controlled Gene Silencing. *Advanced Healthcare Materials* **4**, 760-770 (2015).

135. Kim, M.S., Gruneich, J., Jing, H. & Diamond, S.L. Photo-induced release of active plasmid from crosslinked nanoparticles: o-nitrobenzyl/methacrylate functionalized polyethyleneimine. *Journal of Materials Chemistry* **20**, 3396-3403 (2010).

136. Yin, L. et al. Light-Responsive Helical Polypeptides Capable of Reducing Toxicity and Unpacking DNA: Toward Nonviral Gene Delivery. *Angewandte Chemie International Edition* **52**, 9182-9186 (2013).

137. Yuan, Y., Zhang, C.-J. & Liu, B. A Photoactivatable AIE Polymer for Light-Controlled Gene Delivery: Concurrent Endo/Lysosomal Escape and DNA Unpacking. *Angewandte Chemie International Edition* **54**, 11419-11423 (2015).

138. Chen, C.-C. et al. DNA−Gold Nanorod Conjugates for Remote Control of Localized Gene Expression by near Infrared Irradiation. *Journal of the American Chemical Society* **128**, 3709-3715 (2006).

139. Lee, S.E., Liu, G.L., Kim, F. & Lee, L.P. Remote Optical Switch for Localized and Selective Control of Gene Interference. *Nano Letters* **9**, 562-570 (2009).

140. Lee, S.E. et al. Photonic Gene Circuits by Optically Addressable siRNA-Au Nanoantennas. *ACS Nano* **6**, 7770-7780 (2012).

141. Wang, B.-K. et al. Gold-nanorods-siRNA nanoplex for improved photothermal therapy by gene silencing. *Biomaterials* **78**, 27-39 (2016).

142. Wang, F. et al. Efficient, dual-stimuli responsive cytosolic gene delivery using a RGD modified disulfide-linked polyethylenimine functionalized gold nanorod. *Journal of Controlled Release* **196**, 37-51 (2014).

143. Huang, X. et al. Modular Plasmonic Nanocarriers for Efficient and Targeted Delivery of Cancer-Therapeutic siRNA. *Nano Letters* **14**, 2046-2051 (2014).

144. Huang, X. et al. Light-activated RNA interference in human embryonic stem cells. *Biomaterials* **63**, 70-79 (2015).

145. Sau, T.K. & Murphy, C.J. Room Temperature, High-Yield Synthesis of Multiple Shapes of Gold Nanoparticles in Aqueous Solution. *Journal of the American Chemical Society* **126**, 8648-8649 (2004).

146. Dykman, L. & Khlebtsov, N. Gold nanoparticles in biomedical applications: recent advances and perspectives. *Chemical Society Reviews* **41**, 2256-2282 (2012).

147. Zakaria, H.M. et al. Small Molecule- and Amino Acid-Induced Aggregation of Gold Nanoparticles. *Langmuir* **29**, 7661-7673 (2013).

148. Daniel, M.-C. & Astruc, D. Gold Nanoparticles: Assembly, Supramolecular Chemistry, Quantum-Size-Related Properties, and Applications toward Biology, Catalysis, and Nanotechnology. *Chemical Reviews* **104**, 293-346 (2004).

149. Rosi, N.L. et al. Oligonucleotide-Modified Gold Nanoparticles for Intracellular Gene Regulation. *Science* **312**, 1027-1030 (2006).

150. Tkachenko, A.G. et al. Multifunctional Gold Nanoparticle−Peptide Complexes for Nuclear Targeting. *Journal of the American Chemical Society* **125**, 4700-4701 (2003).

151. Joshi, P.P., Yoon, S.J., Hardin, W.G., Emelianov, S. & Sokolov, K.V. Conjugation of Antibodies to Gold Nanorods through Fc Portion: Synthesis and Molecular Specific Imaging. *Bioconjugate Chemistry* **24**, 878-888 (2013).

152. Ghosh, P., Han, G., De, M., Kim, C.K. & Rotello, V.M. Gold nanoparticles in delivery applications. *Advanced Drug Delivery Reviews* **60**, 1307-1315 (2008).

153. Wang, C. & Irudayaraj, J. Gold Nanorod Probes for the Detection of Multiple Pathogens. *Small* **4**, 2204-2208 (2008).

154. Huang, X., Jain, P.K., El-Sayed, I.H. & El-Sayed, M.A. Gold nanoparticles: interesting optical properties and recent applications in cancer diagnostics and therapy. *Nanomedicine* **2**, 681-693 (2007).

155. Nikoobakht, B. & El-Sayed, M.A. Preparation and Growth Mechanism of Gold Nanorods (NRs) Using Seed-Mediated Growth Method. *Chemistry of Materials* **15**, 1957-1962 (2003).

156. Lee, K.-S. & El-Sayed, M.A. Dependence of the Enhanced Optical Scattering Efficiency Relative to That of Absorption for Gold Metal Nanorods on Aspect Ratio, Size, End-Cap Shape, and Medium Refractive Index. *The Journal of Physical Chemistry B* **109**, 20331-20338 (2005).

157. Jain, P.K., Eustis, S. & El-Sayed, M.A. Plasmon Coupling in Nanorod Assemblies: Optical Absorption, Discrete Dipole Approximation Simulation, and Exciton-Coupling Model. *The Journal of Physical Chemistry B* **110**, 18243-18253 (2006).

158. Huang, X., El-Sayed, I.H., Qian, W. & El-Sayed, M.A. Cancer Cell Imaging and Photothermal Therapy in the Near-Infrared Region by Using Gold Nanorods. *Journal of the American Chemical Society* **128**, 2115-2120 (2006).

159. Mackey, M.A., Ali, M.R.K., Austin, L.A., Near, R.D. & El-Sayed, M.A. The Most Effective Gold Nanorod Size for Plasmonic Photothermal Therapy: Theory and In Vitro Experiments. *The Journal of Physical Chemistry B* **118**, 1319-1326 (2014).

160. Yang, X. et al. Near-Infrared Light-Triggered, Targeted Drug Delivery to Cancer Cells by Aptamer Gated Nanovehicles. *Advanced Materials* **24**, 2890-2895 (2012).

161. Boyer, D., Tamarat, P., Maali, A., Lounis, B. & Orrit, M. Photothermal Imaging of Nanometer-Sized Metal Particles Among Scatterers. *Science* **297**, 1160-1163 (2002).

162. El-Sayed, M.A. Some Interesting Properties of Metals Confined in Time and Nanometer Space of Different Shapes. *Accounts of Chemical Research* **34**, 257-264 (2001).

163. Chen, H. et al. Understanding the Photothermal Conversion Efficiency of Gold Nanocrystals. *Small* **6**, 2272-2280 (2010).

164. Baffou, G., Quidant, R. & García de Abajo, F.J. Nanoscale Control of Optical Heating in Complex Plasmonic Systems. *ACS Nano* **4**, 709-716 (2010).

165. Kyrsting, A., Bendix, P.M., Stamou, D.G. & Oddershede, L.B. Heat Profiling of Three-Dimensionally Optically Trapped Gold Nanoparticles using Vesicle Cargo Release. *Nano Letters* **11**, 888-892 (2011).

166. Govorov, A.O. & Richardson, H.H. Generating heat with metal nanoparticles. *Nano Today* **2**, 30-38 (2007).

167. Webb, J.A. & Bardhan, R. Emerging advances in nanomedicine with engineered gold nanostructures. *Nanoscale* **6**, 2502-2530 (2014).

168. Braun, G.B. et al. Laser-Activated Gene Silencing via Gold Nanoshell−siRNA Conjugates. *ACS Nano* **3**, 2007-2015 (2009).

169. Wijaya, A., Schaffer, S.B., Pallares, I.G. & Hamad-Schifferli, K. Selective Release of Multiple DNA Oligonucleotides from Gold Nanorods. *ACS Nano* **3**, 80-86 (2009).

170. Sershen, S.R., Westcott, S. L., Halas, N. J. and West, J. L. Temperature-sensitive polymer–nanoshell composites for photothermally modulated drug delivery. *J. Biomed. Mater. Res* **51**, 293–298 (2000).

171. Huang, J., Jackson, K.S. & Murphy, C.J. Polyelectrolyte Wrapping Layers Control Rates of Photothermal Molecular Release from Gold Nanorods. *Nano Letters* **12**, 2982-2987 (2012).

172. Kang, H. et al. Near-Infrared Light-Responsive Core–Shell Nanogels for Targeted Drug Delivery. *ACS Nano* **5**, 5094-5099 (2011).

173. Wu, G. et al. Remotely Triggered Liposome Release by Near-Infrared Light Absorption via Hollow Gold Nanoshells. *Journal of the American Chemical Society* **130**, 8175-8177 (2008).

174. Ma, Y. et al. Gold Nanoshell Nanomicelles for Potential Magnetic Resonance Imaging, Light-Triggered Drug Release, and Photothermal Therapy. *Advanced Functional Materials* **23**, 815-822 (2013).

175. Chang, Y.-T. et al. Near-Infrared Light-Responsive Intracellular Drug and siRNA Release Using Au Nanoensembles with Oligonucleotide-Capped Silica Shell. *Advanced Materials* **24**, 3309-3314 (2012).

176. Yang, J. et al. Spatially Confined Fabrication of Core–Shell Gold Nanocages@Mesoporous Silica for Near-Infrared Controlled Photothermal Drug Release. *Chemistry of Materials* **25**, 3030-3037 (2013).

177. Li, H. et al. Near-infrared light-responsive supramolecular nanovalve based on mesoporous silica-coated gold nanorods. *Chemical Science* **5**, 2804-2808 (2014).

178. Li, N. et al. A Near-Infrared Light-Triggered Nanocarrier with Reversible DNA Valves for Intracellular Controlled Release. *Advanced Functional Materials* **23**, 2255-2262 (2013).

179. Liu, J. et al. Gold Nanorods Coated with Mesoporous Silica Shell as Drug Delivery System for Remote Near Infrared Light-Activated Release and Potential Phototherapy. *Small* **11**, 2323-2332 (2015).

180. Jain, P.K., Qian, W. & El-Sayed, M.A. Ultrafast Cooling of Photoexcited Electrons in Gold Nanoparticle−Thiolated DNA Conjugates Involves the Dissociation of the Gold−Thiol Bond. *Journal of the American Chemical Society* **128**, 2426-2433 (2006).

181. Melamed, J.R., Edelstein, R.S. & Day, E.S. Elucidating the Fundamental Mechanisms of Cell Death Triggered by Photothermal Therapy. *ACS Nano* **9**, 6-11 (2015).

182. Yu, Chang, S.-S., Lee, C.-L. & Wang, C.R.C. Gold Nanorods: Electrochemical Synthesis and Optical Properties. *The Journal of Physical Chemistry B* **101**, 6661-6664 (1997).

183. Jana, N.R., Gearheart, L. & Murphy, C.J. Wet Chemical Synthesis of High Aspect Ratio Cylindrical Gold Nanorods. *The Journal of Physical Chemistry B* **105**, 4065-4067 (2001).

184. Jana, N.R., Gearheart, L. & Murphy, C.J. Seed-Mediated Growth Approach for Shape-Controlled Synthesis of Spheroidal and Rod-like Gold Nanoparticles Using a Surfactant Template. *Advanced Materials* **13**, 1389-1393 (2001).

185. Jiang, X.C., Brioude, A. & Pileni, M.P. Gold nanorods: Limitations on their synthesis and optical properties. *Colloids and Surfaces A: Physicochemical and Engineering Aspects* **277**, 201-206 (2006).

186. Betty, C.R.-K. et al. The stabilization and targeting of surfactant-synthesized gold nanorods. *Nanotechnology* **20**, 434005 (2009).

187. Gole, A. & Murphy, C.J. Polyelectrolyte-Coated Gold Nanorods: Synthesis, Characterization and Immobilization. *Chemistry of Materials* **17**, 1325-1330 (2005).

188. Niidome, Y. et al. Surface modification of gold nanorods with synthetic cationic lipids. *Chemical Communications*, 3777-3779 (2007).

189. Vigderman, L., Manna, P. & Zubarev, E.R. Quantitative Replacement of Cetyl Trimethylammonium Bromide by Cationic Thiol Ligands on the Surface of Gold Nanorods and Their Extremely Large Uptake by Cancer Cells. *Angewandte Chemie* **124**, 660-665 (2012).

190. Patino, T. et al. Multifunctional gold nanorods for selective plasmonic photothermal therapy in pancreatic cancer cells using ultra-short pulse near-infrared laser irradiation. *Nanoscale* **7**, 5328-5337 (2015).

191. Wijaya, A. & Hamad-Schifferli, K. Ligand Customization and DNA Functionalization of Gold Nanorods via Round-Trip Phase Transfer Ligand Exchange. *Langmuir* **24**, 9966-9969 (2008).

192. Atcha, K. et al. Biocompatible PEGylated gold nanorods as colored contrast agents for targeted in vivo cancer applications. *Nanotechnology* **21**, 315101 (2010).

193. Liu, K. et al. Biocompatible Gold Nanorods: One-Step Surface Functionalization, Highly Colloidal Stability, and Low Cytotoxicity. *Langmuir* **31**, 4973-4980 (2015).

194. Yu, C., Varghese, L. & Irudayaraj, J. Surface Modification of Cetyltrimethylammonium Bromide-Capped Gold Nanorods to Make Molecular Probes. *Langmuir* **23**, 9114-9119 (2007).

195. Eghtedari, M., Liopo, A.V., Copland, J.A., Oraevsky, A.A. & Motamedi, M. Engineering of Hetero-Functional Gold Nanorods for the in vivo Molecular Targeting of Breast Cancer Cells. *Nano Letters* **9**, 287-291 (2009).

196. Li, Z. et al. RGD-Conjugated Dendrimer-Modified Gold Nanorods for in Vivo Tumor Targeting and Photothermal Therapy. *Molecular Pharmaceutics* **7**, 94-104 (2010).

197. Pan, B. et al. DNA-Templated Ordered Array of Gold Nanorods in One and Two Dimensions. *The Journal of Physical Chemistry C* **111**, 12572-12576 (2007).

198. Hurst, S.J., Lytton-Jean, A.K.R. & Mirkin, C.A. Maximizing DNA Loading on a Range of Gold Nanoparticle Sizes. *Analytical chemistry* **78**, 8313-8318 (2006).

199. Pekcevik, I.C., Poon, L.C.H., Wang, M.C.P. & Gates, B.D. Tunable Loading of Single-Stranded DNA on Gold Nanorods through the Displacement of Polyvinylpyrrolidone. *Analytical Chemistry* **85**, 9960-9967 (2013).

200. Li, J. et al. Simple and Rapid Functionalization of Gold Nanorods with Oligonucleotides Using an mPEG-SH/Tween 20-Assisted Approach. *Langmuir* **31**, 7869-7876 (2015).

201. Sendroiu, I.E., Warner, M.E. & Corn, R.M. Fabrication of Silica-Coated Gold Nanorods Functionalized with DNA for Enhanced Surface Plasmon Resonance Imaging Biosensing Applications. *Langmuir* **25**, 11282-11284 (2009).

202. Shin Ae, K. et al. Surface-enhanced localized surface plasmon resonance biosensing of avian influenza DNA hybridization using subwavelength metallic nanoarrays. *Nanotechnology* **22**, 289501 (2011).

203. Hurst, S.J., Hill, H.D. & Mirkin, C.A. "Three-Dimensional Hybridization" with Polyvalent DNA−Gold Nanoparticle Conjugates. *Journal of the American Chemical Society* **130**, 12192-12200 (2008).

204. Storhoff, J.J., Elghanian, R., Mirkin, C.A. & Letsinger, R.L. Sequence-Dependent Stability of DNA-Modified Gold Nanoparticles. *Langmuir* **18**, 6666-6670 (2002).

205. Alper, J. & Hamad-Schifferli, K. Effect of Ligands on Thermal Dissipation from Gold Nanorods. *Langmuir* **26**, 3786-3789 (2010).

206. Conner, S.D. & Schmid, S.L. Regulated portals of entry into the cell. *Nature* **422**, 37-44 (2003).

207. Cristiana, S.O.P., Ricardo Pires das, N. & Lino, S.F. Nanoparticles for intracellular-targeted drug delivery. *Nanotechnology* **22**, 494002 (2011).

208. Verma, A. & Stellacci, F. Effect of Surface Properties on Nanoparticle–Cell Interactions. *Small* **6**, 12-21 (2010).

209. Chou, L.Y.T., Ming, K. & Chan, W.C.W. Strategies for the intracellular delivery of nanoparticles. *Chemical Society Reviews* **40**, 233-245 (2011).

210. Oliveira, S., van Rooy, I., Kranenburg, O., Storm, G. & Schiffelers, R.M. Fusogenic peptides enhance endosomal escape improving siRNA-induced silencing of oncogenes. *International Journal of Pharmaceutics* **331**, 211-214 (2007).

211. Akinc, A., Thomas, M., Klibanov, A.M. & Langer, R. Exploring polyethylenimine-mediated DNA transfection and the proton sponge hypothesis. *The Journal of Gene Medicine* **7**, 657-663 (2005).

212. Salomone, F. et al. A novel chimeric cell-penetrating peptide with membrane-disruptive properties for efficient endosomal escape. *Journal of Controlled Release* **163**, 293-303 (2012).

213. Selbo, P.K. et al. Photochemical internalization provides time- and space-controlled endolysosomal escape of therapeutic molecules. *Journal of Controlled Release* **148**, 2-12 (2010).

214. Cronican, J.J. et al. Potent Delivery of Functional Proteins into Mammalian Cells in Vitro and in Vivo Using a Supercharged Protein. *ACS Chemical Biology* **5**, 747-752 (2010).

215. Xu, Y. & Szoka, F.C. Mechanism of DNA Release from Cationic Liposome/DNA Complexes Used in Cell Transfection. *Biochemistry* **35**, 5616-5623 (1996).

216. Wagner, E., Plank, C., Zatloukal, K., Cotten, M. & Birnstiel, M.L. Influenza virus hemagglutinin HA-2 N-terminal fusogenic peptides augment gene transfer by transferrin-polylysine-DNA complexes: toward a synthetic virus-like gene-transfer vehicle. *Proceedings of the National Academy of Sciences of the United States of America* **89**, 7934-7938 (1992).

217. Subbarao, N.K., Parente, R.A., Szoka, F.C., Nadasdi, L. & Pongracz, K. The pH-dependent bilayer destabilization by an amphipathic peptide. *Biochemistry* **26**, 2964-2972 (1987).

218. Simões, S. et al. Transfection of human macrophages by lipoplexes via the combined use of transferrin and pH-sensitive peptides. *Journal of Leukocyte Biology* **65**, 270-279 (1999).

219. Futaki, S. et al. Unique features of a pH-sensitive fusogenic peptide that improves the transfection efficiency of cationic liposomes. *The Journal of Gene Medicine* **7**, 1450-1458 (2005).

220. Lee, M.-T., Chen, F.-Y. & Huang, H.W. Energetics of Pore Formation Induced by Membrane Active Peptides. *Biochemistry* **43**, 3590-3599 (2004).

221. Mandal, M. & Lee, K.-D. Listeriolysin O-liposome-mediated cytosolic delivery of macromolecule antigen in vivo: enhancement of antigen-specific cytotoxic T lymphocyte frequency, activity, and tumor protection. *Biochimica et Biophysica Acta (BBA) - Biomembranes* **1563**, 7-17 (2002).

222. Ferrer-Miralles, N., Vázquez, E. & Villaverde, A. Membrane-active peptides for non-viral gene therapy: making the safest easier. *Trends in Biotechnology* **26**, 267-275 (2008).

223. Zasloff, M. Antimicrobial peptides of multicellular organisms. *Nature* **415**, 389-395 (2002).

224. Galdiero, S. et al. Peptide-Lipid Interactions: Experiments and Applications. *International Journal of Molecular Sciences* **14**, 18758 (2013).

225. Li, M. et al. Discovery and Characterization of a Peptide That Enhances Endosomal Escape of Delivered Proteins in Vitro and in Vivo. *Journal of the American Chemical Society* **137**, 14084-14093 (2015).

226. Ogris, M., Carlisle, R.C., Bettinger, T. & Seymour, L.W. Melittin Enables Efficient Vesicular Escape and Enhanced Nuclear Access of Nonviral Gene Delivery Vectors. *Journal of Biological Chemistry* **276**, 47550-47555 (2001).

227. Boeckle, S., Fahrmeir, J., Roedl, W., Ogris, M. & Wagner, E. Melittin analogs with high lytic activity at endosomal pH enhance transfection with purified targeted PEI polyplexes. *Journal of Controlled Release* **112**, 240-248 (2006).

228. Wooddell, C.I. et al. Hepatocyte-targeted RNAi Therapeutics for the Treatment of Chronic Hepatitis B Virus Infection. *Molecular Therapy* **21**, 973-985 (2013).

229. Luan, L. et al. Peptide amphiphiles with multifunctional fragments promoting cellular uptake and endosomal escape as efficient gene vectors. *Journal of Materials Chemistry B* **3**, 1068-1078 (2015).

230. Fasoli, A. et al. Mechanistic Insight into CM18-Tat11 Peptide Membrane-Perturbing Action by Whole-Cell Patch-Clamp Recording. *Molecules* **19**, 9228 (2014).

231. Boussif, O. et al. A versatile vector for gene and oligonucleotide transfer into cells in culture and in vivo: polyethylenimine. *Proceedings of the National Academy of Sciences* **92**, 7297-7301 (1995).

232. Yu, G.S. et al. Synthesis of PAMAM Dendrimer Derivatives with Enhanced Buffering Capacity and Remarkable Gene Transfection Efficiency. *Bioconjugate Chemistry* **22**, 1046-1055 (2011).

233. Remy, J.-S., Sirlin, C., Vierling, P. & Behr, J.-P. Gene Transfer with a Series of Lipophilic DNA-Binding Molecules. *Bioconjugate Chemistry* **5**, 647-654 (1994).

234. Perche, F. et al. Hydroxychloroquine-conjugated gold nanoparticles for improved siRNA activity. *Biomaterials* **90**, 62-71 (2016).

235. Seglen, P.O., Grinde, B. & Solheim, A.E. Inhibition of the Lysosomal Pathway of Protein Degradation in Isolated Rat Hepatocytes by Ammonia, Methylamine, Chloroquine and Leupeptin. *European Journal of Biochemistry* **95**, 215-225 (1979).

236. Tian, W.-d. & Ma, Y.-q. Insights into the endosomal escape mechanism via investigation of dendrimer-membrane interactions. *Soft Matter* **8**, 6378-6384 (2012).

237. Berg, K. et al. Photochemical Internalization. *A Novel Technology for Delivery of Macromolecules into Cytosol* **59**, 1180-1183 (1999).

238. Febvay, S., Marini, D.M., Belcher, A.M. & Clapham, D.E. Targeted Cytosolic Delivery of Cell-Impermeable Compounds by Nanoparticle-Mediated, Light-Triggered Endosome Disruption. *Nano Letters* **10**, 2211-2219 (2010).

239. Wang, S. et al. Light-Controlled Delivery of Monoclonal Antibodies for Targeted Photoinactivation of Ki-67. *Molecular Pharmaceutics* **12**, 3272-3281 (2015).

240. Oliveira, S., Fretz, M.M., Høgset, A., Storm, G. & Schiffelers, R.M. Photochemical internalization enhances silencing of epidermal growth factor receptor through improved endosomal escape of siRNA. *Biochimica et Biophysica Acta (BBA) - Biomembranes* **1768**, 1211-1217 (2007).

241. Raemdonck, K., Naeye, B., Høgset, A., Demeester, J. & De Smedt, S.C. Prolonged gene silencing by combining siRNA nanogels and photochemical internalization. *Journal of Controlled Release* **145**, 281-288 (2010).

242. Jayakumar, M.K.G. et al. Near-Infrared-Light-Based Nano-Platform Boosts Endosomal Escape and Controls Gene Knockdown in Vivo. *ACS Nano* **8**, 4848-4858 (2014).

243. Krpetić, Ž. et al. Inflicting Controlled Nonthermal Damage to Subcellular Structures by Laser-Activated Gold Nanoparticles. *Nano Letters* **10**, 4549-4554 (2010).

244. Asahara, T. et al. Isolation of Putative Progenitor Endothelial Cells for Angiogenesis. *Science* **275**, 964-966 (1997).

245. Hur, J. et al. Characterization of Two Types of Endothelial Progenitor Cells and Their Different Contributions to Neovasculogenesis. *Arteriosclerosis, Thrombosis, and Vascular Biology* **24**, 288-293 (2004).

246. Ishikawa, M. & Asahara, T. Endothelial Progenitor Cell Culture for Vascular Regeneration. *Stem Cells and Development* **13**, 344-349 (2004).

247. Moubarik, C. et al. Transplanted Late Outgrowth Endothelial Progenitor Cells as Cell Therapy Product for Stroke. *Stem Cell Reviews and Reports* **7**, 208-220 (2011).

248. Lee, S.H. et al. Genistein Promotes Endothelial Colony-Forming Cell (ECFC) Bioactivities and Cardiac Regeneration in Myocardial Infarction. *PLOS ONE* **9**, e96155 (2014).

249. Yoo, E.-S. et al. Outgrowing Endothelial Cells That Are Derived from Human Umbilical Cord Blood Improve Neovascularization in Hind-Limb Ischemia. *Blood* **110**, 3697-3697 (2007).

250. Medina, R.J., O'Neill, C.L., Humphreys, M.W., Gardiner, T.A. & Stitt, A.W. Outgrowth Endothelial Cells: Characterization and Their Potential for Reversing Ischemic Retinopathy. *Investigative Ophthalmology & Visual Science* **51**, 5906-5913 (2010).

251. Fraineau, S., Palii, C.G., Allan, D.S. & Brand, M. Epigenetic regulation of endothelial-cell-mediated vascular repair. *FEBS Journal* **282**, 1605-1629 (2015).

252. Suárez, Y. & Sessa, W.C. MicroRNAs As Novel Regulators of Angiogenesis. *Circulation Research* **104**, 442-454 (2009).

253. Zhang, Q., Kandic, I. & Kutryk, M.J. Dysregulation of angiogenesis-related microRNAs in endothelial progenitor cells from patients with coronary artery disease. *Biochemical and Biophysical Research Communications* **405**, 42-46 (2011).

254. Chang, T.-Y. et al. miRNome traits analysis on endothelial lineage cells discloses biomarker potential circulating microRNAs which affect progenitor activities. *BMC Genomics* **15**, 802 (2014).

255. Pourrajab, F., Vakili Zarch, A., Hekmatimoghaddam, S. & Zare-Khormizi, M.R. MicroRNAs; easy and potent targets in optimizing therapeutic methods in reparative angiogenesis. *Journal of Cellular and Molecular Medicine* **19**, 2702-2714 (2015).

256. Meng, S. et al. Downregulation of MicroRNA-130a Contributes to Endothelial Progenitor Cell Dysfunction in Diabetic Patients via Its Target Runx3. *PLOS ONE* **8**, e68611 (2013).

257. Zhang, X. et al. Increased expression of microRNA-221 inhibits PAK1 in endothelial progenitor cells and impairs its function via c-Raf/MEK/ERK pathway. *Biochemical and Biophysical Research Communications* **431**, 404-408 (2013).

258. Minami, Y. et al. Effect of atorvastatin on microRNA 221 / 222 expression in endothelial progenitor cells obtained from patients with coronary artery disease. *Eur J Clin Invest* **39** (2009).

259. Fish, J.E. et al. miR-126 Regulates Angiogenic Signaling and Vascular Integrity. *Developmental Cell* **15**, 272-284.

260. van Solingen, C. et al. MicroRNA-126 modulates endothelial SDF-1 expression and mobilization of Sca-1(+)/Lin(-) progenitor cells in ischaemia. *Cardiovascular Research* **92**, 449-455 (2011).

261. Zhao, T., Li, J. & Chen, A.F. MicroRNA-34a induces endothelial progenitor cell senescence and impedes its angiogenesis via suppressing silent information regulator 1. *American Journal of Physiology - Endocrinology And Metabolism* **299**, E110-E116 (2010).

262. Zhu, S. et al. MicroRNA-10A* and MicroRNA-21 Modulate Endothelial Progenitor Cell Senescence Via Suppressing High-Mobility Group A2. *Circulation Research* **112**, 152-164 (2013).

263. Jakob, P. et al. Loss of AngiomiR-126 and 130a in Angiogenic Early Outgrowth Cells from Patients with Chronic Heart Failure: Role for Impaired in vivo Neovascularization and Cardiac Repair Capacity. *Circulation* (2012).

264. Pankratz, F. et al. MicroRNA-155 Exerts Cell-Specific Antiangiogenic but Proarteriogenic Effects During Adaptive Neovascularization. *Circulation* **131**, 1575-1589 (2015).

265. Kong, W. et al. Upregulation of miRNA-155 promotes tumour angiogenesis by targeting VHL and is associated with poor prognosis and triple-negative breast cancer. *Oncogene* **33**, 679-689 (2014).

266. Yang, D., Wang, J., Xiao, M., Zhou, T. & Shi, X. Role of Mir-155 in Controlling HIF-1α Level and Promoting Endothelial Cell Maturation. *Scientific Reports* **6**, 35316 (2016).

267. Wilhelm, C. et al. Magnetic control of vascular network formation with magnetically labeled endothelial progenitor cells. *Biomaterials* **28**, 3797-3806 (2007).

268. Gomes, R.S.M. et al. Efficient Pro-survival/angiogenic miRNA Delivery by an MRI-Detectable Nanomaterial. *ACS Nano* **7**, 3362-3372 (2013).

269. Yang, H.N. et al. Differentiation of endothelial progenitor cells into endothelial cells by heparin-modified supramolecular pluronic nanogels encapsulating bFGF and complexed with VEGF165 genes. *Biomaterials* **35**, 4716-4728 (2014).

270. Masotti, A. et al. Regulation of angiogenesis through the efficient delivery of microRNAs into endothelial cells using polyamine-coated carbon nanotubes. *Nanomedicine: Nanotechnology, Biology and Medicine* **12**, 1511-1522 (2016).

271. Devalliere, J. et al. Sustained delivery of proangiogenic microRNA-132 by nanoparticle transfection improves endothelial cell transplantation. *The FASEB Journal* **28**, 908-922 (2014).

272. Liu, X.-Q., Song, W.-J., Sun, T.-M., Zhang, P.-Z. & Wang, J. Targeted Delivery of Antisense Inhibitor of miRNA for Antiangiogenesis Therapy Using cRGD-Functionalized Nanoparticles. *Molecular Pharmaceutics* **8**, 250-259 (2011).

273. Mitra, R.N. et al. Nanoparticle-mediated miR200-b delivery for the treatment of diabetic retinopathy. *Journal of Controlled Release* **236**, 31-37 (2016).

274. Gu, Z., Biswas, A., Zhao, M. & Tang, Y. Tailoring nanocarriers for intracellular protein delivery. *Chem Soc Rev* **40**, 3638-3655 (2011).

275. Kam, N.W.S. & Dai, H. Carbon Nanotubes as Intracellular Protein Transporters: Generality and Biological Functionality. *Journal of the American Chemical Society* **127**, 6021-6026 (2005).

276. Liu, Y. et al. Delivery of Intact Transcription Factor by Using Self-Assembled Supramolecular Nanoparticles. *Angewandte Chemie International Edition* **50**, 3058-3062 (2011).

277. Wu, J. et al. Development of multinuclear polymeric nanoparticles as robust protein nanocarriers. *Angew Chem Int Ed Engl* **53**, 8975-8979 (2014).

278. Ghosh, P. et al. Intracellular Delivery of a Membrane-Impermeable Enzyme in Active Form Using Functionalized Gold Nanoparticles. *Journal of the American Chemical Society* **132**, 2642-2645 (2010).

279. D'Astolfo, D.S. et al. Efficient intracellular delivery of native proteins. *Cell* **161**, 674-690 (2015).

280. Tong, R., Hemmati, H.D., Langer, R. & Kohane, D.S. Photoswitchable Nanoparticles for Triggered Tissue Penetration and Drug Delivery. *Journal of the American Chemical Society* **134**, 8848-8855 (2012).

281. Vasdekis, A.E., Scott, E.A., O'Neil, C.P., Psaltis, D. & Hubbell, J.A. Precision Intracellular Delivery Based on Optofluidic Polymersome Rupture. *ACS Nano* **6**, 7850-7857 (2012).

282. Pérez-Juste, J., Pastoriza-Santos, I., Liz-Marzán, L.M. & Mulvaney, P. Gold nanorods: Synthesis, characterization and applications. *Coordination Chemistry Reviews* **249**, 1870-1901 (2005).

283. Jiang, Z. et al. Controlled protein delivery from photosensitive nanoparticles. *Journal of Biomedical Materials Research Part A* **103**, 65-70 (2015).

284. Díaz, J.A. & Gibbs-Davis, J.M. Sharpening the Thermal Release of DNA from Nanoparticles: Towards a Sequential Release Strategy. *Small* **9**, 2862-2871 (2013).

285. Yun, C.S. et al. Nanometal Surface Energy Transfer in Optical Rulers, Breaking the FRET Barrier. *Journal of the American Chemical Society* **127**, 3115-3119 (2005).

286. Singh, M.P. & Strouse, G.F. Involvement of the LSPR Spectral Overlap for Energy Transfer between a Dye and Au Nanoparticle. *Journal of the American Chemical Society* **132**, 9383-9391 (2010).

287. Brzostowski, J.A., Meckel, T., Hong, J., Chen, A. & Jin, T. in Current Protocols in Protein Science (John Wiley & Sons, Inc., 2001).

288. Potokar, M. et al. Intermediate filaments attenuate stimulation-dependent mobility of endosomes/lysosomes in astrocytes. *Glia* **58**, 1208-1219 (2010).

289. Hu, Y. et al. Cytosolic delivery of membrane-impermeable molecules in dendritic cells using pH-responsive core-shell nanoparticles. *Nano Lett* **7**, 3056-3064 (2007).

290. Vankayala, R., Huang, Y.K., Kalluru, P., Chiang, C.S. & Hwang, K.C. First demonstration of gold nanorods-mediated photodynamic therapeutic destruction of tumors via near infra-red light activation. *Small* **10**, 1612-1622 (2014).

291. Levitsky, K.L., Toledo-Aral, J.J., López-Barneo, J. & Villadiego, J. Direct confocal acquisition of fluorescence from X-gal staining on thick tissue sections. *Scientific Reports* **3**, 2937 (2013).

292. Casey, J.R., Grinstein, S. & Orlowski, J. Sensors and regulators of intracellular pH. *Nat Rev Mol Cell Biol* **11**, 50-61 (2010).

293. Kenworthy, A.K. Imaging Protein-Protein Interactions Using Fluorescence Resonance Energy Transfer Microscopy. *Methods* **24**, 289-296 (2001).

294. Dunn, K.W., Kamocka, M.M. & McDonald, J.H. A practical guide to evaluating colocalization in biological microscopy. *American Journal of Physiology - Cell Physiology* **300**, C723-C742 (2011).

295. Sanganalmath, S.K. & Bolli, R. Cell therapy for heart failure: a comprehensive overview of experimental and clinical studies, current challenges, and future directions. *Circ Res* **113**, 810-834 (2013).

296. Raval, Z. & Losordo, D.W. Cell therapy of peripheral arterial disease: from experimental findings to clinical trials. *Circ Res* **112**, 1288-1302 (2013).

297. Asahara, T., Kawamoto, A. & Masuda, H. Concise review: Circulating endothelial progenitor cells for vascular medicine. *Stem Cells* **29**, 1650-1655 (2011).

298. Fadini, G.P., Losordo, D. & Dimmeler, S. Critical Reevaluation of Endothelial Progenitor Cell Phenotypes for Therapeutic and Diagnostic Use. *Circulation Research* **110**, 624-637 (2012).

299. Kinoshita, M. et al. Long-term clinical outcome after intramuscular transplantation of granulocyte colony stimulating factor-mobilized CD34 positive cells in patients with critical limb ischemia. *Atherosclerosis* **224**, 440-445 (2012).

300. Kawamoto, A. & Losordo, D.W. Endothelial progenitor cells for cardiovascular regeneration. *Trends Cardiovasc Med* **18**, 33-37 (2008).

301. Fuchs, S., Motta, A., Migliaresi, C. & Kirkpatrick, C.J. Outgrowth endothelial cells isolated and expanded from human peripheral blood progenitor cells as a potential source of autologous cells for endothelialization of silk fibroin biomaterials. *Biomaterials* **27**, 5399-5408 (2006).

302. Suarez, Y. & Sessa, W.C. MicroRNAs As Novel Regulators of Angiogenesis. *Circulation Research* **104**, 442-454 (2009).

303. Hua, Z. et al. MiRNA-Directed Regulation of VEGF and Other Angiogenic Factors under Hypoxia. *PLOS ONE* **1**, e116 (2006).

304. Gao, Z.Q., Zhu, X.L. & Dou, Y.X. The miR-302/367 cluster: a comprehensive update on its evolution and functions. *Open Biol* **5** (2015).

305. Yang, D., Wang, J., Xiao, M., Zhou, T. & Shi, X. Role of Mir-155 in Controlling HIF-1alpha Level and Promoting Endothelial Cell Maturation. *Sci Rep* **6**, 35316 (2016).

306. Wang, H. et al. A Near-Infrared Laser-Activated "Nanobomb" for Breaking the Barriers to MicroRNA Delivery. *Advanced Materials* **28**, 347-355 (2016).

307. Chiu, Y.-L. & Rana, T.M. siRNA function in RNAi: A chemical modification analysis. *RNA* **9**, 1034-1048 (2003).

308. Rai, A. et al. One-step synthesis of high-density peptide-conjugated gold nanoparticles with antimicrobial efficacy in a systemic infection model. *Biomaterials* **85**, 99-110 (2016).

309. Pulkkinen, K.H., Ylä-Herttuala, S. & Levonen, A.-L. Heme oxygenase 1 is induced by miR-155 via reduced BACH1 translation in endothelial cells. *Free Radical Biology and Medicine* **51**, 2124-2131 (2011).

310. Lee, S.H., Mok, H., Jo, S., Hong, C.A. & Park, T.G. Dual gene targeted multimeric siRNA for combinatorial gene silencing. *Biomaterials* **32**, 2359-2368 (2011).

311. Haque, F. et al. Ultrastable synergistic tetravalent RNA nanoparticles for targeting to cancers. *Nano Today* **7**, 245-257 (2012).

312. Lee, S.J. et al. Co-delivery of VEGF and Bcl-2 dual-targeted siRNA polymer using a single nanoparticle for synergistic anti-cancer effects in vivo. *Journal of Controlled Release* **220, Part B**, 631-641 (2015).

313. Roh, Y.H. et al. A Multi-RNAi Microsponge Platform for Simultaneous Controlled Delivery of Multiple Small Interfering RNAs. *Angewandte Chemie International Edition* **55**, 3347-3351 (2016).

314. Fomina, N., Sankaranarayanan, J. & Almutairi, A. Photochemical mechanisms of light-triggered release from nanocarriers. *Advanced Drug Delivery Reviews* **64**, 1005-1020 (2012).

315. Nguyen, Q.N. et al. Light controllable siRNAs regulate gene suppression and phenotypes in cells. *Biochimica et Biophysica Acta (BBA) - Biomembranes* **1758**, 394-403 (2006).

316. Yamazoe, S., Liu, Q., McQuade, L.E., Deiters, A. & Chen, J.K. Sequential Gene Silencing Using Wavelength-Selective Caged Morpholino Oligonucleotides. *Angewandte Chemie* **126**, 10278-10282 (2014).

317. Chang, S.-H. & Hla, T. Gene regulation by RNA binding proteins and microRNAs in angiogenesis. *Trends in Molecular Medicine* **17**, 650-658 (2011).

318. Pedroso, D.C.S. et al. Improved Survival, Vascular Differentiation and Wound Healing Potential of Stem Cells Co-Cultured with Endothelial Cells. *PLOS ONE* **6**, e16114 (2011).

319. Spierings, D.C. et al. Ordered progression of stage-specific miRNA profiles in the mouse B2 B-cell lineage. *Blood* **117**, 5340-5349 (2011).

320. Chen, Y., Gelfond, J., McManus, L.M. & Shireman, P.K. Temporal microRNA expression during in vitro myogenic progenitor cell proliferation and differentiation: regulation of proliferation by miR-682. *Physiological Genomics* **43**, 621-630 (2011).

321. Liu, X. et al. Sequential introduction of reprogramming factors reveals a time-sensitive requirement for individual factors and a sequential EMT-MET mechanism for optimal reprogramming. *Nat Cell Biol* **15** (2013).

322. Varkouhi, A.K., Scholte, M., Storm, G. & Haisma, H.J. Endosomal escape pathways for delivery of biologicals. *Journal of Controlled Release* **151**, 220-228 (2011).

323. Liu, X. et al. Sequential introduction of reprogramming factors reveals a time-sensitive requirement for individual factors and a sequential EMT–MET mechanism for optimal reprogramming. *Nat Cell Biol* **15**, 829-838 (2013).

324. Hevner, R.F., Hodge, R.D., Daza, R.A.M. & Englund, C. Transcription factors in glutamatergic neurogenesis: Conserved programs in neocortex, cerebellum, and adult hippocampus. *Neuroscience Research* **55**, 223-233 (2006).

325. Hsieh, J. Orchestrating transcriptional control of adult neurogenesis. *Genes & Development* **26**, 1010-1021 (2012).

326. Li, L. et al. Sequential expression of miR-182 and miR-503 cooperatively targets FBXW7, contributing to the malignant transformation of colon adenoma to adenocarcinoma. *The Journal of Pathology* **234**, 488-501 (2014).

327. Chen, J.-F. et al. The role of microRNA-1 and microRNA-133 in skeletal muscle proliferation and differentiation. *Nat Genet* **38**, 228-233 (2006).

328. Ren, J., Jin, P., Wang, E., Marincola, F.M. & Stroncek, D.F. MicroRNA and gene expression patterns in the differentiation of human embryonic stem cells. *Journal of Translational Medicine* **7**, 20 (2009).

329. Parchem, Ronald J. et al. Two miRNA Clusters Reveal Alternative Paths in Late-Stage Reprogramming. *Cell Stem Cell* **14**, 617-631.

330. Henzler, C.M. et al. Staged miRNA re-regulation patterns during reprogramming. *Genome Biology* **14**, R149 (2013).

331. Suh, W. et al. Transplantation of Endothelial Progenitor Cells Accelerates Dermal Wound Healing with Increased Recruitment of Monocytes/Macrophages and Neovascularization. *STEM CELLS* **23**, 1571-1578 (2005).

332. Hsu, Patrick D., Lander, Eric S. & Zhang, F. Development and Applications of CRISPR-Cas9 for Genome Engineering. *Cell* **157**, 1262-1278 (2014).